TRANSPORT IN THE PERIVASCULAR SPACES OF THE BRAIN: VISUALIZATION OF CONVECTION-ENHANCED DELIVERY

A Dissertation

Presented to the Faculty of the Graduate School

of Cornell University

In Partial Fulfillment of the Requirements for the Degree of

Doctor of Philosophy

by

Justin George Rosch

January 2017

TRANSPORT IN THE PERIVASCULAR SPACES OF THE BRAIN: VISUALIZATION OF CONVECTION ENHANCED DELIVERY

Justin George Rosch, Ph. D.

Cornell University 2017

A method for circumventing the blood-brain barrier (BBB), called convection-enhanced delivery (CED), involves directly infusing therapeutics into the brain tissue. The behavior of the therapeutics once in the tissue is not well understood. To gain insight into the behavior of materials introduced into the brain during a CED-like infusion, we used two-photon fluorescence microscopy to observe infusate movement *in vivo*. With our experiments, we were able to sample the infusate volume with high temporal (~30 s volume sample) and spatial (~2.5 μm^3 voxel size) resolution. With observable locations of the infused materials at many time points throughout the infusion, we determined important position, velocity, and volume characteristics of each infusion. For smaller, less-rigid materials, we saw larger distribution volume relative to larger, more-rigid materials. Furthermore, we were able to directly observe materials entering and traveling in the perivascular spaces (PVS), which are thin annular regions surrounding blood vessels in the brain. PVS are believed to be important in a number of neurological disorders and neural homeostasis, and we have shown that they play an influential role in the movement of infused materials. For a given timepoint in an infusion, the average PVS occupancy of infused materials can be a large portion of the total volume observed, depending on the location of an available

space relative to the infusion needle outlet. Given the large amount of infused material entering the PVS, we theorize how this knowledge can be used to influence clinical treatments of neurological disorders in order to have better control of where the infused materials will go during different parts of an infusion.

BIOGRAPHICAL SKETCH

Justin Rosch was born in Boston, MA in December 1989. He attended Bentley elementary school and Collins Middle School in Salem, MA, before moving on to Bishop Fenwick High School in Peabody, MA. At Bishop Fenwick, developed a strong interest in math and chemistry, and decided to pursue a degree in chemical engineering. Without full comprehension of what *true* upstate New York winters were like, he decided to pursue his Bachelor of Engineering degree at Clarkson University. He believes that the cold, barren landscape of Potsdam, NY, influenced his ability to avoid distraction, allowing him to succeed in the pursuit of his degree. During his junior year at Clarkson, Cornell biomedical engineering Professor David Putnam gave a lecture on the opportunities that Cornell offered to prospective graduate students. After spending a delightful summer at the University of Maryland as an undergraduate researcher investigating statistical mechanics of DNA-polymer complexes (without realizing he was studying advanced thermodynamics), he decided a research career would fit him well. After much deliberation over his offers, he opted to attend Cornell University to pursue his Ph.D. in chemical engineering.

ACKNOWLEDGMENTS

The culmination of the materials in this dissertation would not have happened without the help of a number of individuals. First and foremost, my committee has been central to completion of this work. My advisor, William Olbricht, aided my development early on in my graduate career, and directly guided my GK-12 project, which led to interesting observations. Chris Schaffer gave endless guidance and support while I struggled to develop as a surgeon and researcher into the midpoint of my project, and gave constant help with direction while I learned how to analyze the results of our experiments.

Poornima Gadamsetty worked with me through all of the experiments performed, and gave constant feedback to the methods by which we carried out the experiments. Through this, we improved as a group, and were able to collaborate and carry out myriad experiments, the numbers of which are rarely paralleled in the literature. She also helped discover better ways of carrying out the data analysis, which proved to be challenging with the number of infusions we had. Her constant troubleshooting with imaging allowed for the completion of our work, and her patience as I developed as a surgeon was invaluable.

Manjari Sistla and Nozomi Nishimura gave me direct instruction on how to perform various surgical techniques required for my experiments. Without their help and guidance, I would not have been able to gather the preclinical animal work skills I have today. Jason Jones and Elizabeth Wayne constantly helped me to understand the way things were done in the Schaffer lab, from wet lab chores to optics issues to working with the lab servers.

Linda Tompkins served as my boss/mentor during my tenure as a TA trainer/fellow. Her help led to great personal development throughout my graduate career, and helped make me a better-rounded individual and professional. Derina

Samuel served as my boss/mentor during my time working with Cornell's Center for Teaching Excellence, and allowed me to grow as a presenter and instructor.

John Foo was the greatest lab mate anyone could have asked for. When Bill left for the NSF, John became a constant source for scientific discussion. More than this though, John was a friend who encouraged me to try numerous new things, including the TA trainer position that led to funding for two years, and incredible development of leadership and interpersonal skills. We also broadcasted the best radio show, John and Justin in the Evening, to ever grace the airwaves of the greater Ithaca area in 2013.

I would like to thank all of the friends I've made during my time in Ithaca. My first year class, and in particular Joe, Brian, and Kyle, for great times and staying close for five years. Lindsey Crawford was (and is) the big sister I never had. Rambert Nahm, my only roommate, gave constant insight into my research and life. Johan Grimm and Jenny Novotney were fantastic karaoke singers and friends. Mark Richards and Jason Boock were intramural teammates and friends throughout most of my time in Ithaca.

Special thanks goes to Clifford Long, a longtime friend of mine from Clarkson University. We remained good friends throughout my time at Cornell, and his constant encouragement made all the difference as I struggled through the middle years of grad school. I have never been one to keep friends through major life transitions, but I am proud to have had Cliff as a friend throughout undergrad, grad school, and beyond.

Finally, I'd like to thank my family for continued encouragement and love.

Portions of this work were supported by NSF grant 1133426. I personally was funded by the BME GK-12 program at Cornell during my third year, and by Engineering Learning Initiatives during my fourth and fifth year.

TABLE OF CONTENTS

LIST OF FIGURES

LIST OF TABLES

CHAPTER 1

INTRODUCTION

Treating afflictions of the central nervous system (CNS) is particularly challenging and increasingly necessary. According to the Centers for Disease Control and Prevention, malignant neoplasms (cancer), cerebrovascular diseases (stroke), Alzheimer's disease, and Parkinson's disease are among the 15 leading causes of death in the United States [1]. Malignant neoplasms include all forms of cancer, but of particular concern to the CNS is malignant glioma, a difficult to treat form of cancer afflicting the brain. There were 22,850 new reported cases of "brain & other nervous system" cancers in 2015 [2]. Although this number is small relative to the incidences of cancer affecting other parts of the body, brain and nervous system cancers are less treatable than other cancers. Surgical removal of brain tumors is insufficient treatment, as malignant glioma cells are capable of moving beyond the edge of the tumor mass into the parenchyma. The cells are left behind in the brain, leading to recurrence of the tumor.

Diseases affecting the brain require innovative treatments, as the brain is protected by the blood-brain barrier (BBB). Materials in the bloodstream are prevented from directly entering the brain by the presence of endothelial tight junctions, which prevent all but the smallest molecules (<400 Da) from entering passively. In addition, brain endothelial cells have transporter proteins that can selectively transport compounds from the brain interstitium to the bloodstream. Larger molecules can move across the BBB using carrier-mediated transport [3], but

this mechanism is reserved for particular molecules needed to maintain homeostasis. While some research focuses on exploiting receptor-mediated transport or hiding small therapeutic molecules from efflux transport proteins [4,5], there are other methods for circumventing the BBB [6] that present novel means for treating CNS disease. Of particular interest is the technique of convection-enhanced delivery (CED), in which materials are directly infused into brain tissue.

Glioma treatments currently employ a combination of tumor removal by surgical resection and subsequent treatment with radiation, including, sometimes, implantation of a chemotherapeutic drug [7,8] to treat migrating cells beyond the resection cavity. The chemotherapeutic drug is incorporated in polymeric Gliadel ® wafers, which can be introduced directly into the resection cavity following surgery. Transport of the drug contained in the wafers, bischloroethylnitrosourea (BCNU), into the surrounding tissue relies on diffusion. The concentration gradient between the drug reservoir and the tissue allows the drug molecules to diffuse into the parenchyma. Once in the parenchyma, the BCNU passively diffuses throughout the adjacent tissue and may reach and destroy tumor cells in the local area. However, recurrence of the tumors is still an issue [9], despite the Gliadel® treatment showing clinical efficacy [10,11]. Diffusive transport of BCNU combined with various clearance mechanisms that can remove drugs from the brain parenchyma are likely culprits for tumor recurrence. Clearance mechanisms include transport across blood vessel walls into the bloodstream, enzymatic degradation, biotransformation, binding to cell membranes, and incorporation into non-target cells. In order to effectively prevent recurrence, a therapeutically useful concentration of the drug must penetrate into the parenchyma to

reach migrating malignant cells. It is these clearance mechanisms, in addition to mass-transfer issues in the extra cellular spaces (ECS), which play critical roles in limiting the drug from getting to its desired destination.

To overcome the diffusive limitations of treating malignant gliomas, convection-enhanced delivery (CED) has been developed as a means of improving the overall distribution of drug molecules in the brain. This technique is not significantly more invasive than the current treatments, as it is employed for infusing therapeutics directly into tumors and after the tumor has been removed via surgery. Bobo et al. used this technique *in vivo* to deliver macromolecules into the feline brain [12]. Their worked showed increased distribution of large molecules using CED compared with diffusive transport alone. CED has been studied for use with a number of different infusates for treatment of different CNS diseases [13–16]. CED's efficacy ranges from no enhancement [17] to significant efficacy when delivered alongside conventional treatments [18–20].

In principle, convection should aid in increasing distribution of the infused drug, which should lead to a higher probability of the drug reaching targets that cannot be reached by diffusive transport. Without a detailed examination of the spatial distribution of the infusate once injected, it is difficult to assess why efficacy is not as good as theory predicts it should be. Simulation and modelling has been studied to predict infusion patterns [21–23]. To study the behavior of materials introduced directly into the parenchyma, research has been done using gel phantoms [24–26]. Agarose gels of either 0.2% or 0.6% concentration were used to predict infusion patterns for given flow rates or catheter design. While modelling and *in vitro* methods

can help influence design of clinical procedures, they do not fully predict the behavior of materials once introduced *in vivo*. To fully understand the mechanisms that govern transport phenomena during a CED-like infusion, direct imaging is necessary. Post-mortem image analysis of CED in tissue slices excised from rodents gives insights into overall infusate distribution [13,18,20,27–29]. Nuclear magnetic resonance (NMR) imaging allows for real-time imaging of the infusate during CED infusions in various animal models [24,28,30,31]. Post-mortem analysis gives the investigators a view of the overall infusate distribution near the termination of the animal. NMR gives location data for the infusate at different times during the infusion, but often lacks small-scale resolution for determining micron-scale motion.

Interest in micron-scale motion of the infused material has gained importance due to discoveries indicating that transport of fluid in the brain may be enhanced in the perivascular spaces (PVS) surrounding blood vessels [32,33]. PVS are thin regions outside blood vessels in the brain. During CED, it is possible that the infused materials have access to these paths [34]. Evidence suggests that these paths may present less resistance to flow than that presented by interstitial pathways [32,33]. The infused material varies from experiment to experiment, but nanoparticles have gained interest in recent years due to their ability to encapsulate large amounts of therapeutics and to deliver therapeutics over time within the brain [6].

To investigate the movement of nanoparticles during a CED-like infusion, we present a technique for sampling the infusate with high spatial and temporal resolution. This technique involves the use of two-photon microscopy, a fluorescence imaging method that allows for deeper tissue penetration and a well-defined focal

volume [35,36]. By oscillating a motorized stage while observing two-photon fluorescence, we can elucidate transport properties of nanoparticles while they are infused. The unparalleled resolution allows for accurate determination of distribution volume, parenchymal velocity, and perivascular velocity. We can identify PVS entrances for nanoparticle efflux from the infusion site, and observe how local PVS influence the infusate cloud morphology. By varying particle size and type, we can observe how the ECS mean pore size influences particle movement. With a deeper understanding of particle dynamics, CED can be further improved for therapeutic purposes, as we can predict where the particles will go with greater accuracy. We believe this knowledge can be used to influence further research and clinical practice for better treatment of CNS diseases.

Chapter 2 details the development of the imaging technique used in this work. By performing a craniotomy on an anesthetized rat and imaging in our oscillatory fashion, we can observe particle movement in real time. This chapter also covers the algorithm development for processing the raw image stacks and the process for extracting various quantitative features from the images. We discuss how we came to the parameters used for the studies shown in Chapter 3. This chapter contains various output images that give weight to the assertion that high resolution images of the infusate being delivered in real time are necessary for understanding what actually occurs during a CED-like infusion. Finally, we discuss the drawbacks of this system, which include the finite imaging depth involved with fluorescence imaging.

Chapter 3 describes experimental results. With the imaging setup discussed in Chapter 2, we aimed to characterize the infusions of various infusates similar to those

used in the literature. We infused four sizes of fluorescently-tagged polystyrene beads and three sizes of fluorescent liposomes. We also ran infusions using an infusate composed of a fluorescent, lower molecular weight dextran and polystyrene beads. We were able to determine that smaller particles traveled further than larger particles for a given amount of time of infusion. The volume of distribution for the polystyrene beads was significantly lower than that of the liposomes of comparable size. The hindrance on the larger particles for both the polystyrene beads and the liposomes leads to lower volumes of distribution for each. The velocity of the infused material propagating from the infusion site for the various infusates dropped rapidly as the infusion progresses. The smaller infusates maintained a higher velocity than the larger infusates at greater penetration distances. All infusates entered perivascular spaces. For the larger infusates, the proportion of particles in the perivascular space relative the particles in the parenchyma was markedly higher on average for the larger particles. The larger infusates could move further from the point of infusion due to the presence of these perivascular spaces. We discuss the quantitative results and present theories for the influences of perivascular transport on the distribution of therapeutics during a CED infusion. We discuss interesting behavior, such as the presence of micro-channels in the parenchyma allowing movement of larger particles, which seem to lead to perivascular spaces. These findings are discussed in the context of the literature in this area.

Chapter 4 departs from the two-photon imaging, and discusses agarose gel experimentation done to model the interface between different regions of the brain (or different sections of tissue). By preparing an agarose gel layer of lower concentration

on a second layer of higher concentration, and infusing near the location where the two layers meet, we were able simulate infusions near an interface. The material properties of the different concentration gels on either side of the interface lead to reduced concentration of the infusate in the higher concentration gel. The penetration distance of the infusate into the higher concentration gel was also reduced, further reinforcing the role that porosity and mean pore size play in allowing transport of therapeutics *in vivo*. While agarose gel experimentation cannot fully simulate an *in vivo* infusion into living tissue, it can act as a guide before moving to animal and clinical experimentation.

Chapter 5 briefly discusses the context of this work and recommendations for future studies.

CHAPTER 2

DEVELOPMENT OF TWO-PHOTON IMAGING METHOD FOR IN VIVO EXPERIMENTS

2.1 Introduction

There are two ways to investigate therapeutic material transport *in vivo*. The first is to infuse materials tagged with some marker that can be viewed post-mortem to elucidate where the materials went during the infusion. This method generally involves sacrificing the animal immediately after the infusion, and sectioning the brain to view cross-sections of the infused material. Bobo et al. infused In-labelled transferrin into anesthetized cats to investigate the effect of convection on increasing the distribution volume of infused materials [12]. MacKay et al. investigated the effects of particle charge, particle diameter, and steric coating of liposomes on their overall distribution and penetration depth following a CED infusion [27]. Hamilton et al. co-infused heparin with various proteins to show that heparin was capable of increasing distribution volume relative to protein infusion alone [13].

The second way to elucidate the transport behavior of the materials during a CED-like infusion is to image the infusate as it is being introduced into the tissue. The most common method of this technique involves using magnetic resonance imaging (MRI). A tracer molecule, such as gadolinium, is introduced into the tissue while the MRI setup images the region of the tissue. The recorded images contain location data

of the infused material. From this location data, the volume occupied by the infusate, or volume of distribution (V_D), of the infused material is reconstructed from the data. Kim et al. infused gadolinium-labelled-albumin with Evan's blue dye into the rat dorsal and ventral hippocampus as part of a dynamic contrast-enhanced MRI experiment. They showed that the marker preferentially travelled along anatomy with less fluid resistance [37]. Richardson et al. infused gadoteridol with adeno-associated virus serotype 2-glial-derived neurotrophic factor into the putamen and thalamus of monkeys. They were able to accurately reconstruct the distribution volume, as well as correlate the gadoteridol signal with GDNF expression, indicating therapeutic efficacy when attempting to treat Parkinson's [38]. Haar et al. observed gadolinium-diethylenetriamine pentaacetic acid as tracer infused during CED using MRI to study the differences between behaviour of the infusate under normal and ischemic conditions [31]. All of these, and the majority of other MRI-monitored CED infusions, rely on temporal resolutions of minutes to tens of minutes for a single volume sampling, with voxel size on the order of 0.1-1 mm^3. Therefore, the behavior that is being studied via MRI is a macroscopic view of the infused materials.

While viewing infused materials macroscopically can lead to clinical prediction of therapeutic efficacy and enhanced targeting for various CNS treatments, anatomical mechanisms that affect the overall behaviour of the infused material occur on the micro and nano-length scales. The average effective pore size in the extracellular spaces (ECS) is predicted to be between 38 and 64 nm [39] for healthy tissue, and diffusion experiments using PEG-coated nanoparticles suggest that glioma ECS spacing is even smaller [40]. More recent experiments have shown through real-

time multiple particle tracking that nanoparticles greater than100 nm in diameter are capable of penetrating human and rat tissue [41]. Further investigations using multiple particle tracking have shown that nanoparticles between 100 and 200 nm are capable of moving through roughly one fourth the pores in an area of the tissue. However, nanoparticles larger than 200 nm are extremely hindered in their motion, which suggests pores or pathways are not large enough to accommodate larger particles [42]. Furthermore, there is an additional mode of transport once a therapeutic is introduced into the parenchyma. The brain contains fluid clearance systems that carry materials away from the desired destination [43,44]. It is these clearance systems, in addition to the intrinsic hindered transport through the ECS, which play critical roles in limiting the drug from getting to its desired destination.

Research into the purpose and function of perivascular routes in the brain has increased dramatically in recent years. Perivascular spaces (PVS) had been detailed by research since at least the 1970s [45,46]. These compartments are extensions of the subarachnoid space that encompass brain vasculature, creating thin (micron scale at capillary level) annular regions. Pulsations of the blood vessel walls may help to propel fluid in the PVS [32,47–49]. The PVS have been shown as part of a functioning fluid drainage/lymphatic system in the brain termed the “glymphatic” system by Iliff et al. [43]. This system is believed to play a role in fluid movement-related systems in the brain, such as metabolite clearance [50], tau aggregation following traumatic brain injury [51], and removal/accumulation of amyloid-β [52]. Given the prevalence of blood vessels throughout the brain, the PVS should also play a role in clearance of infused materials during CED.

Two-photon excitation fluorescence (2PEF) microscopy is a novel technique for investigating the microscale movements of infused particles in the brain. In conventional fluorescence imaging, scattering of photons in the biological tissue prevents collection of the fluorescence beyond surface imaging of the sample. Higher-photon imaging modalities, such as 2PEF microscopy, allow for greater imaging depths to be achieved, as scattering of the photons in the biological tissue is greatly reduced. This allows for capturing of imaging planes within the biological tissue down to depths of 1 mm. 2PEF microscopy has been used to observe astrocyte/blood vessel anatomy [53], investigate age-related differences in cerebral capillary blood flow [54], and, most relevant to this work, capture images of perivascular transport during CED in the rat cortex [33]. Previous work in our lab had shown particles moving through the parenchyma and the PVS at vastly different speeds by watching a plane above the point of infusion using this 2PEF technique.

In this study, we developed a platform for imaging the distribution volume of various infusates using two-photon fluorescence microscopy. A live anesthetized rat is placed on a continuously oscillating motorized stage. Fluorescence is captured in two-dimensional planes throughout various depths in the tissue while an infusate is delivered into the rat cortex. This yields compilations of images at the recorded depths at various times throughout the infusion, referred to as “image stacks”. From these image stacks, the location of the infusate in the cortex is tracked over the course of the infusion, allowing for real-time observation of the movement of the infusate. With this information, it is possible to show the infusate morphology (also referred to as cloud morphology) at various points in the infusion with unrivaled spatial and temporal

resolution. The development of this platform allows for *in vivo* characterization of various infusates at the microscale, allowing for an unprecedented look at where therapeutic-like particles go during a CED-like infusion.

2.2 Materials and Methods

2.2.1 Rat Craniotomy Procedure

Adult male Sprague-Dawley rats (weighing 250-450 g) were anesthetized *via* isoflurane inhalation (1 % in oxygen at 0.2 L/min). Animals were secured in a stereotactic frame and an incision was made in the skin along the dorsal midline. Skin and muscle tissue were excised to reveal a ~3 cm section of the skull. A dental drill was used to open a ~1 cm circular craniotomy, exposing the brain from near the midline to the right side of the skull. A 30 gauge needle was used to make a small incision in the dura, and a fine hook was then used to pull back the dura to the outer portions of the craniotomy. Once bleeding near the craniotomy had ceased, fluorescein isothiocyanate (FITC) conjugated to 2-MDa dextran (Sigma-Aldrich, St. Louis, MO) was administered directly to the bloodstream *via* tail vein injection. FITC, once in the bloodstream, labels the blood plasma, allowing for visualization of the vasculature in the brain using 2PEF. A glass coverslip was placed over the craniotomy and fixed to the skull using dental cement. All animal procedures were performed in accordance with the Cornell University Institutional Animal Care and Use Committee guidelines and regulations.

2.2.2 Imaging Setup

To observe the proliferation of infused materials into the rat cortex, we employed a technique using a custom-built microscope setup. To collect emitted fluorescence from the infused materials at multiple depths within the rat cortex, the animal was moved toward and away from the microscope objective continuously over the course of the infusion. Therefore, the recorded images are two dimensional scans of various depths within the rat cortex. The scans occur at discrete times, meaning the compilation of recorded images from a single up and down motion of the motorized stage, or loop, is both spatially and time dependent. The compilation of recorded images from a single loop is referred to as an "image stack".

An example of the imaging setup can be found in **Figure 2.1**. The rat was placed on a 3-axis motorized stage beneath the optics (shown without objective in **Figure 2.1**). A micromanipulator was fixed on the stage near the rat. A plastic rod held the infusion needle in place on the micromanipulator. Rigid plastic tubing was fixed to the non-injecting end of the needle, with the other end attached to the syringe beneath the stage. The syringe was held in place in the syringe pump, a PHD 2000 infusion pump (Harvard Apparatus). The stage and optics were controlled by the computer to the left of the stage (not shown). Once the experiment was set to begin, the lights were turned off, and a black curtain was pulled around the entire stage to conceal the setup from any remaining light.

The white-light camera in the imaging setup was used to locate where the

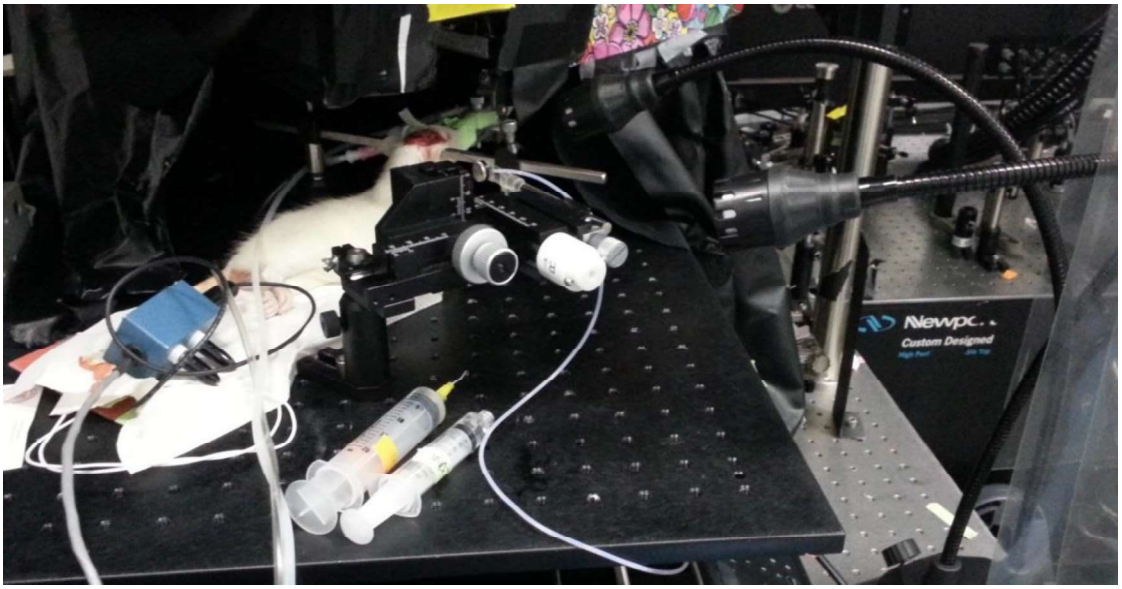

Figure 2.1. Imaging setup used in these studies. The anesthetized rat is placed on the motorized stage beneath the optics. The infusion pump sits beneath the stage, and tubing runs from the syringe containing the nanoparticles to the micromanipulator, which holds the infusion needle.

infusion needle entered the brain. The motion of the needle could be tracked under this 4x objective to the point where the needle was inserted into the brain. It was necessary to estimate the needle's location inside the brain, which was difficult when using the 20x objective, which was needed to achieve sufficient spatial resolution to identify capillaries and their adjacent perivascular spaces. A better way was developed to locate the needle tip inside in the tissue. A 4x objective was still employed, but it was used to observe the fluorescence in the field of view, both in the needle and in the vasculature. This permitted the identification of the blood vessels and the needle that were in the same horizontal plane. By making careful adjustments during insertion, it was possible to keep both the needle and the vessels in plane throughout the insertion. To do this, the tapered needle shaft was placed directly over the coverslip. The micromanipulator was adjusted by one operator while the other operator adjusted the camera through software on the computer. The camera operator moved the stage to follow the needle tip as the micromanipulator operator moved in plane above the coverslip to beyond the edge of the coverslip. The needle tip was then lowered into the plane of the coverslip. The 4x objective allowed a wide enough field of view such that both the needle tip and the coverslip/vasculature could be seen. From here, the camera operator lowered the stage in 100 μm increments, pausing for the micromanipulator operator to lower the needle tip into focus, and thus into the imaging plane. Once the needle was somewhere between 200 – 400 μm below the surface to the brain (coverslip sat directly on the brain tissue), the needle was inserted into the tissue, making sure to avoid any major visible blood vessels. With the needle in the brain, the stage was lowered, and the 4x objective was switched out for a 20x objective. The

coverslip was raised to within 5 – 10 mm of the objective, where water was added between the objective and the coverslip. The imaging plane was close to the plane of the needle tip, and slight positional adjustments were necessary to get the needle tip in focus. From here, the needle tip was inserted further into the brain, and imaging experiments could begin.

There are multiple time scales to be aware of during a single loop. The time to scan the imaging plane and record the data is 0.317 s for a 512 x 512 pix^2 image. The distance between each image depth that is being recorded is 2 μm. The time to travel to each imaging depth is negligible. In a typical experiment, the total vertical depth being imaged is 250 μm, meaning there are 125 images taken in a single direction of the loop. This equates to roughly 40 s, or 80 s total recording time for the loop (the up and down motion). A single experiment can involve infusions at multiple locations within the cortex, with each individual infusion recorded comprised of 4 - 12 loops. It is important to remember the manner in which the data was recorded when interpreting results. We acquire images while the microscope's imaging plane traverses through the cortex from top to bottom and then bottom to top. Thus, images at any specific plane are not acquired at uniform intervals. For example, a plane near the bottom of the stack is imaged late in the traverse from top to bottom. However, that plane is imaged again soon after the microscope's direction changes and it traverses the stack from bottom to top. The only plane that is imaged at uniform intervals is the plane in the center of the stack. Therefore, the temporal resolution of the setup varies depending on the imaging depth. Images near the center of the stack will have similar time between them, but images are further apart in time near the

surface of the brain during a single loop. This time resolution inverts when looking at images between loops, as the recorded image at the end of first loop and beginning of the second loop occur very close in time.

The 0.317 s recording time gives a frame capture rate of 3.15 frames/s, which equates to about 6 μm moved each second. For an isotropic infusion in the brain, a sphere would grow beyond the edge of the viewing plane (about 287 μm) in about 6 s. The materials being infused take much longer (order of minutes) to grow beyond the field of view. It is therefore possible to record multiple loops for a single infusion and observe the movement of the infused materials using this setup. All image data taken was recorded using the referenced method for recording loops, or the up and down image capture technique. No data was taken using a "fixed plane" approach, in which the imaging plane is recorded at a single depth within the cortex, which was primarily used in [33]

In these imaging experiments, three primary types of infusates were used, polystyrene beads, liposomes, and dextrans. The exact sizes and formulations are discussed in Chapter 3. The size of the infusate was varied between 20 – 200 nm for the polystyrene beads, and between 50 – 200 nm for the liposomes. A single size of 3 kDa dextran was used for select experiments.

2.2.3 Determination of Relevant Parameters

Volumetric infusion rates for most studies of convection-enhanced delivery in rodents vary between 0.1-1 μL/min [17,33,55]. However, these studies involve

infusion into subcortical regions of the brain such as the caudate, which is often used in rodent studies because it is a relatively large homogenous region of gray matter. To use 2PEF microscopy for imaging, it was necessary to work in the rodent's cortex, as the maximum allowable depth for 2PEF imaging in tissue is about 1 mm. The thickness of the rodent cortex is only about 2 mm. To keep the infusate confined to the cortex, it was necessary to use a relatively low volumetric infusion rate. Therefore, experiments were carried out at an infusion rate of 0.2 μL/min.

Once the infusion rate was set, the volume of tissue that would have to sampled to include the entire infusion volume could be calculated assuming an isotopic distribution of infusate and considering the porosity of brain tissue, which is about 0.2[56]. This result provided estimates for the magnification that would be necessary to capture the infusate volume in the field of view. A magnification between 1.7 and 2.0 with the 20x objective was used for all the experiments. To accurately capture the small, micron scale capillary perivascular movement, a 512 x 512 pix^2 planar resolution was used. Lower resolutions at 256 x 256 pix^2, 128 x 128 pix^2, and 64 x 64 pix^2 and a higher resolution 1024 x 1024 pix^2 were also tested. Sample figures for the lower resolutions can be found in **Figure 2.2**. The selected resolution dictates the rate at which the images can be captured, with ~1.6 frames per second being captured at 1024 x 1024 pix^2, up to ~20 frames per second captured at 64 x 64 pix^2. The lower resolutions of 256 x 256 pix^2, 128 x 128 pix^2, and 64 x 64 pix^2 sacrificed too much image clarity of the smaller vessels. The higher resolution of 1024 x 1024 pix^2 did not reveal anything that could not be seen at 512 x 512 pix^2. Therefore, a resolution of 512 x 512 pix^2 was used to provide a balance between image clarity and

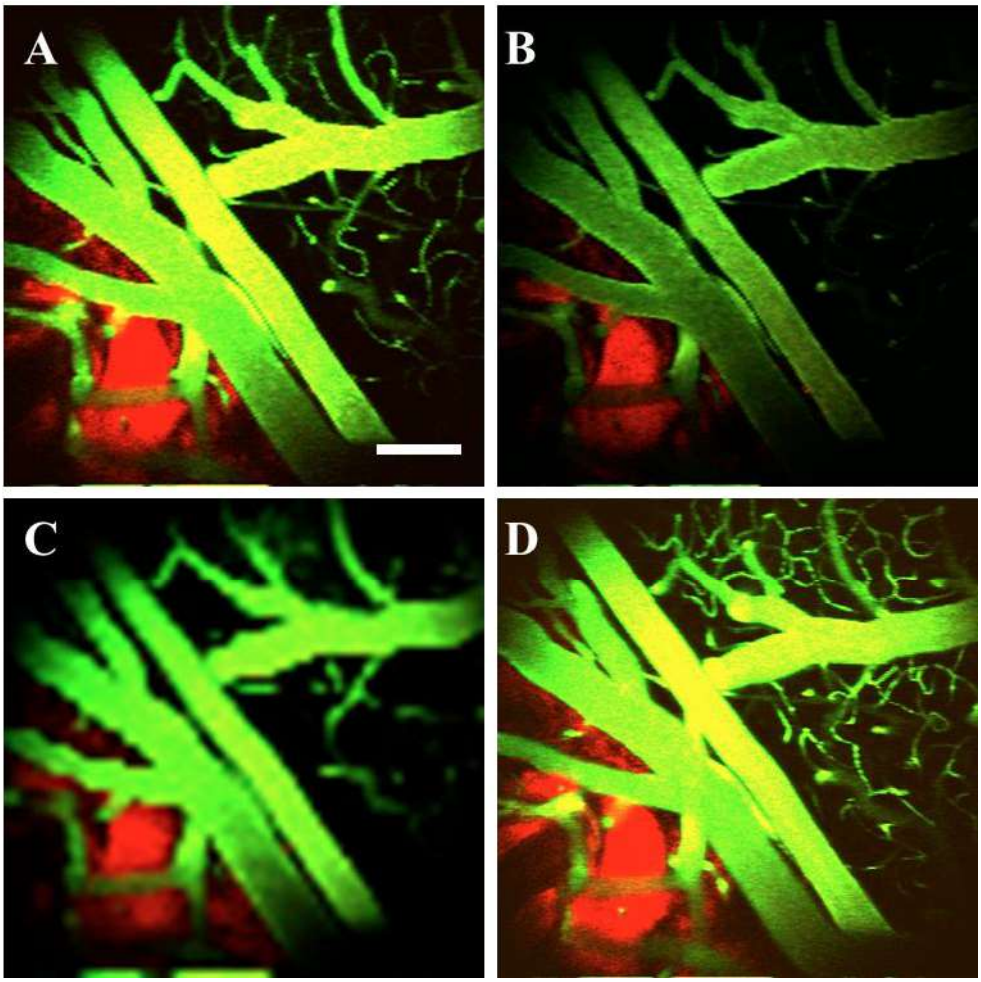

Figure 2.2. Sample images illustrating image resolutions. Blood vessels appear green, while polystyrene beads appear red. The vasculature and the infusate cloud become harder to discern as the resolution decreases from 512 x 512 pix^2 **(D)** to 256 x 256 pix^2 **(A)**, 128 x 128 pix^2 **(B)**, and 64 x 64 pix^2 **(C)**. Scale bar is 100 μm.

scan rate. This gave an image recording rate of ~3.15 frames per second. Finally, the step size in the vertical direction, i.e. into the cortex, was determined by estimating the size of the smallest vessels, which was several μm. Therefore, a vertical step size of 2 μm was chosen, with the intent of capturing all lateral sections of small vessels.

2.2.4 Data Processing

The raw data from the experiments consisted of stacks of tagged image file format (TIFF) images. Each image within a stack is 512 x 512 pix^2. The conversion between pixel and actual distance depends on the objective and magnification setting. During each experiment, the focal plane of the microscope was moved vertically in steps over a predetermined travel distance through the cortical tissue by moving the microscope stage. When the focal plane reached the bottom of the travel distance, the direction of the stage was reversed, and the focal plane moved upward until it reached its initial location. The direction was reversed, and again the focal plane traveled downward through the tissue. This periodic action continued throughout the experiment. The number of images in a stack depended on the number of vertical steps and the total vertical travel distance in the experiment. Each TIFF stack was loaded into ImageJ for filtering. A three-dimensional, 1 pix median filter was applied. The median filter helps to reduce noise in the image while retaining the edges of shapes within the image. The filter looks at the neighboring pixels around each pixel in an image, and replaces it with the median value from these neighboring pixel intensities. This smoothed out edges of vasculature and infusion clouds, effectively

removing image hairs and any irregularities brought about by saturation during recording. An example of the effect of this filtering on an image is shown in **Figure 2.3**.

2.2.5 Extracting Quantitative Features from Images - Automated

Analysis of the images started by converting them to binary images with a specified threshold. Initial development of data processing protocols set the threshold manually at a single intensity determined by probing the background pixel intensity values. Later, the threshold was set using a script that set the value of the threshold as a specified fraction of the mean of the top ten percent of pixel intensity values. To determine the top ten percent of the values, all pixel intensity values for a single image were concatenated and sorted from smallest to greatest. The mean of the top decile of intensity values was calculated. The threshold value was then set to this mean value multiplied by an adjustable coefficient. It was determined that a coefficient of 0.05, corresponding to 5% of the mean of the top ten percent of the pixel intensity values, gave similar values to those that were determined manually. With the threshold level set, pixels with intensity values higher than the threshold value were changed to 1, with all others set to 0.

The threshold script was incorporated into to a data analysis script with modules that could calculate certain values from the stacks of images. All stacks for a single infusion were read into MATLAB one at a time, converted to an array, and calculations of infusion cloud volume, surface area, and velocity of the infusion front

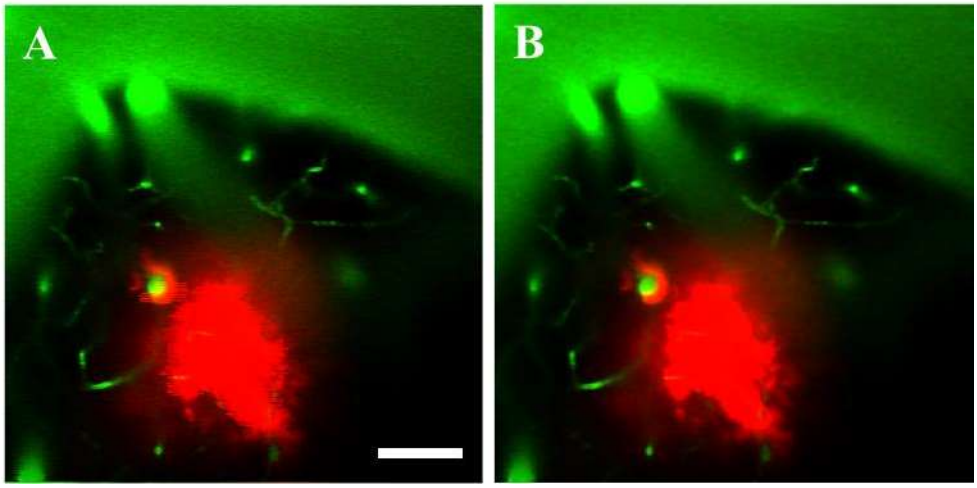

Figure 2.3. Sample image of infusion cloud. **(A)** before and **(B)** after the application of the 1 pixel median filter. Green = FITC-dextran; red = red-orange fluorescently tagged polystyrene beads. The image hairs protruding from the cloud in the red channel are entirely removed. Scale bar is 100 μm.

were performed in sequence.

To calculate distribution volume of nanoparticles the number of pixels containing nanoparticles, which corresponded to values in the array containing a 1, were added together to define the area containing nanoparticles in each image. Multiplying this area value for each slice by the thickness of each slice, defined by the vertical step distance of the microscope stage, gave the volume of nanoparticles contained within each slice of the stack. By adding the volumes of all of these stacks, the total volume of distribution of nanoparticles was determined. The area values were converted from pix^2 to μm^2 prior to multiplication by the step size, which was always 2 μm in our experiments. This is a common volume calculation technique used in imaging analysis [37,57].

To calculate surface area of the infusate, each voxel, consisting of the 1 x 1 planar pixel and the 2 μm depth associated with that pixel, and its neighbors are examined. For each adjacent voxel with a value of 0 (indicating that there are no nanoparticles in that adjacent voxel), the surface area is increased by 1, up to a maximum value of 6 (a voxel described here is a rectangular prism, with 6 faces), indicating a voxel containing nanoparticles is free from any adjacent nanoparticle-containing voxel. The area is summed, and converted to μm to give a total surface area for each image. The total surface area for the volume sample is found by adding up all the surface area values for the sampling of the cloud (which is a one direction sample of the cloud).

To calculate the parenchymal velocity, referred to as the cloud front of the infusion, code was written to sample the extent of penetration of the nanoparticles in

several directions from the point of infusion. The velocity of the moving particles could only be distinguished at the edge of the cloud. A total of 26 directions were sampled, corresponding to 8 compass directions around the needle outlet in plane, the 8 compass directions around a pixel directly above and directly below the needle outlet, and the vertical directions from the needle outlet. By tracking the pixels along the edge of the cloud front in these directions, the velocities of the nanoparticles traveling in each of these directions could be monitored over the whole infusion, giving insights into nanoparticle transport for each of the infusions.

Code developed for the data analysis portion of this work can be found in the appendix.

2.2.6 Extracting Quantitative Features from Images – Manual

To calculate the volume of the cloud, the radius of the cloud in the plane of the needle outlet was measured in the direction of the needle and in directions normal to it. These radii were averaged, giving a mean radius. Infusions resemble a sphere with protrusions corresponding to perivascular routes. The radius was used to calculate the volume of the spherical portion of the cloud, thus giving an estimate for the parenchymal distribution volume. The values were calculated for each time the imaging plane passed through the cloud, giving increasing values with each pass.

To calculate the volume of the perivascular spaces manually, an ImageJ plugin called “Simple Neurite Tracer” was used. Perivascular spaces were identified by their location alongside a vessel, and the plugin was used to measure the length of the

observed particles in the perivascular space. The width of associated vessels and the perivascular width was also measured, which allowed for calculation of both the perivascular volumes and velocities along these routes.

Chapter 3 bases all the data on manual measurements. Developing these algorithms and protocols for discerning these quantitative features was a large part of this work, and thus both methods are presented to show the breadth of work done.

2.3 Results

2.3.1 Sample Infusion Data – 2D Output TIFF Stacks

Each stack of TIFF images contains the fluorescence emission captured during a single cycle through the cortex, which corresponds to one upward movement of the stage followed by the downward movement. This gives an image stack that appears to be capturing images while moving down into the cortex, and subsequently back up and out of the cortex. A representative example of images demonstrating parenchymal and perivascular transport of nanoparticles during a downward traverse of the imaging plane in the cortex is shown in **Figure 2.4**. **Figure 2.4A** is at the top of the image stack, corresponding to a depth of 0 μm. **Figure 2.4B-D** display images at 25 μm distance increments into the brain, with **B** at 25 μm, **C** at 50 μm, and **D** at 75 μm into the cortex (where the infusion needle can also be seen). The presence of perivascular routes surrounding small blood vessels can be seen in **Figure 2.4A-B**. Again, the presence of perivascular spaces is discerned by their annular shape encompassing

vessels, shown in green. The nanoparticles colored red, in this case, 200 nm polystyrene beads, can be seen in the PVS. The imaging records the fluorescence emission that falls within wavelength limits, corresponding to a “green” and a “red” channel. In ImageJ, the two channels can be separated or combined into a composite (as shown in **Figure 2.4**) of the two images at each depth. This technique is common for visualizing the fluorescence data [27,33], and most images shown in this work are composite images of the two channels’ information.

2.3.2 3D Rendering of 2D TIFF Stacks

The imaging technique used here allows for 3D reconstruction of the infusion cloud over a ~30 s portion of an infusion, as this is the required time for the imaging to capture the infusate distribution volume once, in either a downward or upward pass through the infusate cloud. An example of a 3D reconstruction is shown in **Figure 2.5**. **Figure 2.5A** shows a view of the 3D reconstruction looking down on the cloud from above. **Figure 2.5B** shows the same view of the 3D reconstruction angled to show the depth of the reconstruction, which cannot be discerned from a purely top-down view. From this 3D rendering of the data, the perivascular paths and overall cloud morphology are easily visible, and act as a guide for further, more detailed inspection in 2D images. The 3D renderings offer a unique way of displaying relevant spatial information about the distributions of nanoparticles without needing to show multiple frames during an infusion.

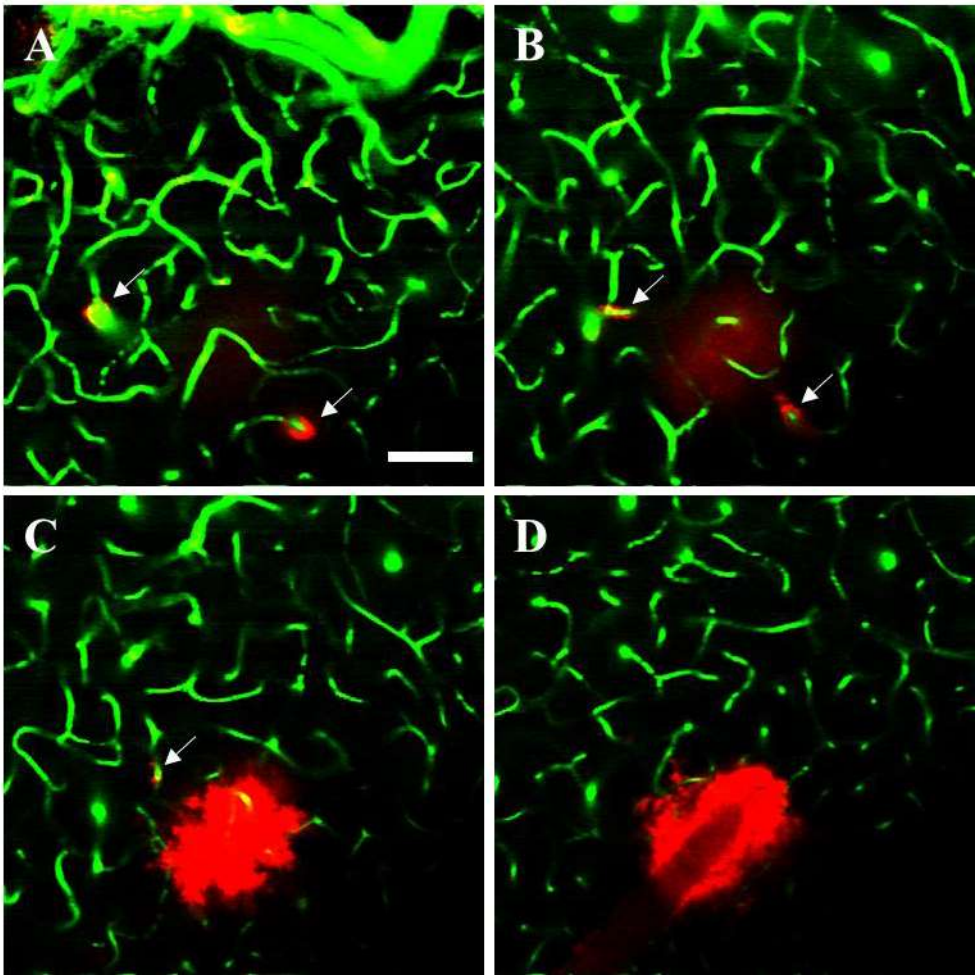

Figure 2.4. Sequence of images from a single loop during a 200 nm polystyrene bead nanoparticle infusion (towards the middle of the infusion, after infusing for about 8 minutes). Both parenchymal and perivascular transport can be seen in the sequence. Green = FITC-dextran; red = red-orange fluorescently tagged polystyrene beads. **(A)** Image near surface of the brain. Depth = 0 μm, time into infusion = 411 s. **(B)** Depth = 25 μm, time into infusion = 419 s. **(C)** Depth = 50 μm, time into infusion = 427 s. **(D)** depth = 75 μm, time into infusion = 435 s. Scale bar is 100 μm. Arrows indicate perivascular routes, which are identified by their adjacent location to vasculature (green due to FITC).

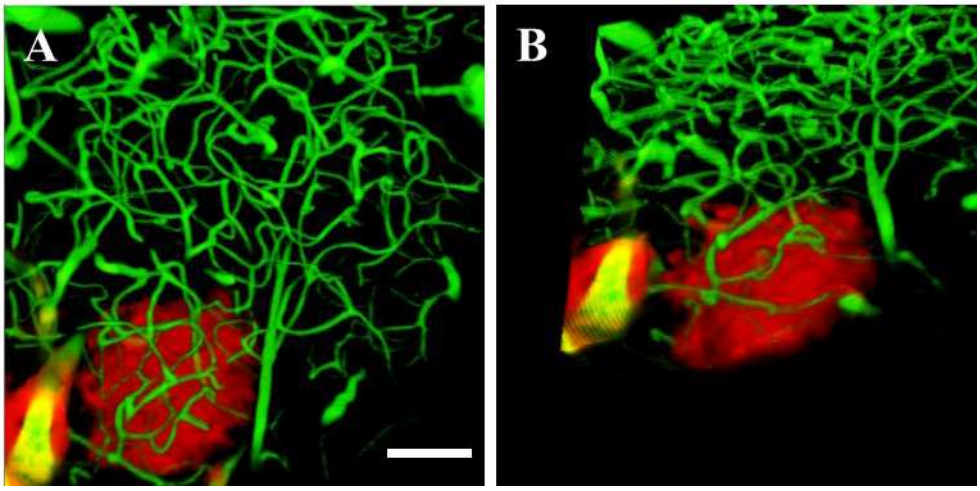

Figure 2.5. 3D reconstruction of one stack of images from a 200 nm polystyrene bead infusion. The reconstruction shows the location of particles during the interval from 248 s to 287 s of the infusion. **(A)** Top-down view of the 3D reconstruction. **(B)** Rotated view of the 3D reconstruction, which sometimes allows for better recognition of PVS transport. Scale bar is 100 μm.

2.3.3 Time-Lapse Images and PVS Identification

Identification of relevant perivascular spaces involves a combination of viewing entire infusions as 2D images through time and 3D reconstruction. To estimate the spatial dimensions of the perivascular spaces, the "Simple Neurite Tracer" plugin in ImageJ is used. Pixel values are converted to μm through known conversion factors provided by the imaging software. An example from this perivascular identification process is shown in **Figure 2.6**. **Figure 2.6A-B** show examples from steps in the 2D and 3D process of finding local PVS. In **Figure 2.6A**, the local PVS are spotted using the 2D stack of images, and confirmed in location in **Figure 2.6B**. In **Figure 2.6C**, the "Simple Neurite Tracer" plugin in ImageJ is used to load the red channel only, isolating the nanoparticles in the image for the script to analyze. A location is entered by the user to define the PVS entrance along the edge of the cloud, and locations of points within the PVS are added by the user as the script interpolates the path between the given points. **Figure 2.6D** shows the output from the script, highlighting in magenta the identified PVS routes. All the PVS routes are saved with an identifier for later reference. This determination of PVS allows for comparison to comparable parenchymal movement, both in time and in position from the needle tip.

2.3.4 Different Magnifications

Most of the data collected over the course of this work involves the use of a

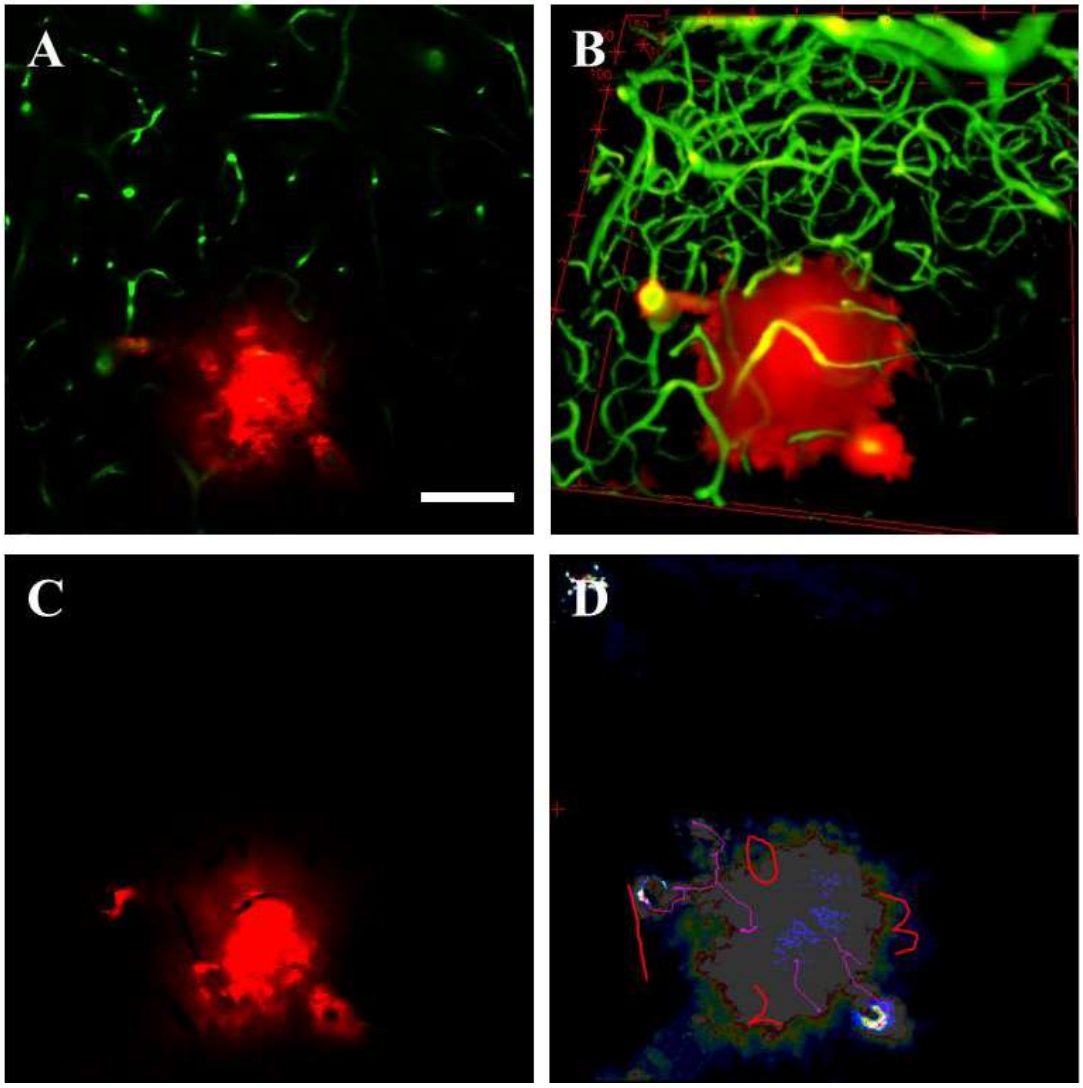

Figure 2.6. General process for identifying and measuring length of PVS. Green = FITC-dextran; red = red-orange fluorescently tagged polystyrene beads. **(A)** Sample imaging plane from 2D image stack used to locate PVS. **(B)** Sample 3D reconstruction used to identify location of PVS. **(C)** "Simple Neurite Tracer" plugin for ImageJ requires loading of a single channel, so the particles are separated from the vasculature. Only the infusion cloud is shown, and is used with the script to trace the PVS. **(D)** The traced PVS paths identified by the script. The user selects a location, and multiple points along the PVS, and the script interpolates the path of the PVS

along those points. Magenta lines indicate traced paths. Image of traced paths is catalogued for later reference. Scale bar is 100 μm.

20X objective, giving much greater spatial resolution at the expense of field of view. For examining the wider view of where nanoparticles travel during the infusion, a 4X objective is used. Sample images taken using this lower magnification objective are shown in **Figure 2.7**. While most perivascular nanoparticles are not discernable at this lower magnification, the parenchymal movement of particles relative to larger vasculature and structures can be observed.

2.3.5 Identification of Non-PVS Fluid Routes

Evidence of fluid pathways that are larger than the mean ECS pore size estimated in [39] is observed five infusions. These pathways are observed for the largest size of particles, 200 nm. An example of this observation is shown in **Figure 2.8**. The arrows indicate the direction of flow for this observation. This phenomenon would not be observable without collecting data in the oscillatory manner discussed in this section, as other imaging techniques would not have the resolution to observe the micron-scale movement of the nanoparticle infusate through these fluid pathways. A fixed imaging depth experiment would likely miss the progression of the nanoparticles through these fluid routes unless a route happened to lie in the fixed imaging plane, which is unlikely. The pathways observed protruded from the edge of the infusion cloud through the parenchyma to a perivascular space. This does not mean that these paths are not present for other particle sizes, but rather that the 200 nm move slowly enough that the movement of the nanoparticles into these pathways can be observed by the imaging.

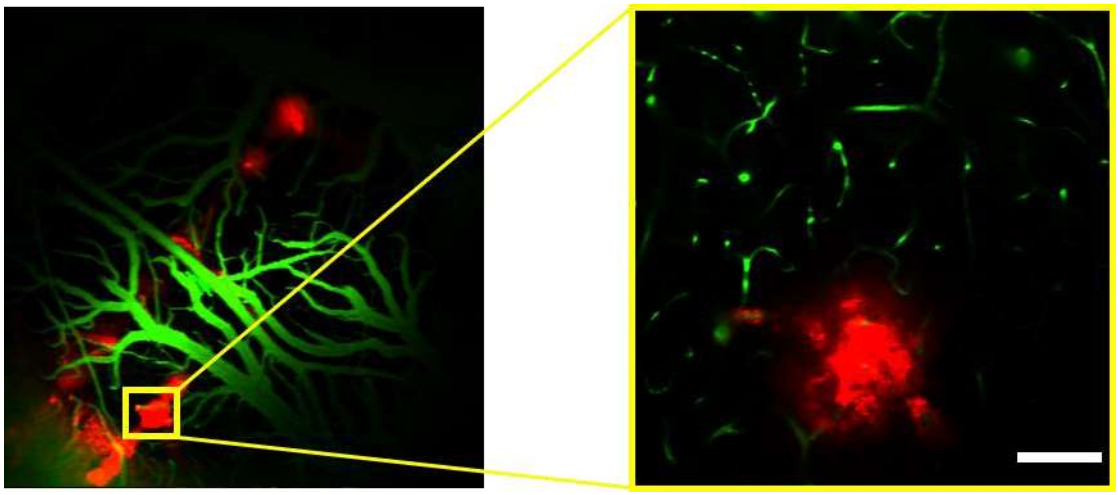

Figure 2.7. Sample image of different magnifications. Green = FITC-dextran; red = red-orange fluorescently tagged polystyrene beads. On the left, the 4x objective gives a much larger field of view than the 20x objective's image on the right. The 4x objective can view the entire open craniotomy, but lacks fine resolution. The fine resolution provided by the 20x objective allows for investigation of micron-scale movements of the infusate. Scale bar is 100 µm.

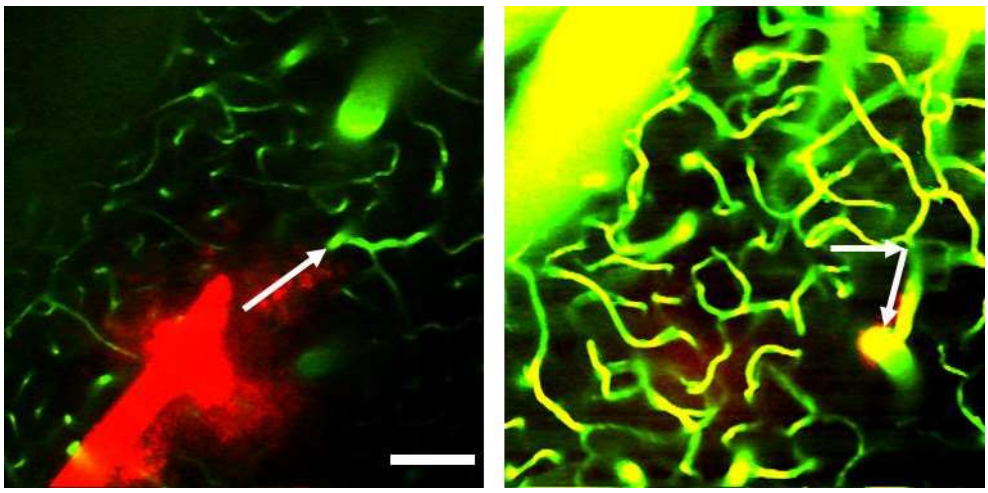

Figure 2.8. Sample of pathway leading from edge of infusion cloud to viable perivascular space. Direction of flow and path taken is indicated by the arrows. The image on the left is near the point of infusion, ~250 µm below the surface of the brain. The image on the right is the surface of the brain. The infusate (200 nm liposomes in this example) moves from the infusion cloud to the vessel's perivascular entrance, and follows a series of interconnected vessels up to the surface, as demonstrated by the white arrows. Scale bar is 100 µm (same scale for both images).

2.4 Discussion

We developed an experimental setup for viewing CED-like infusions with unparalleled resolution. MRI has been used to view infusions at a larger scale [37,38,58], and fluorescence imaging has been used to view microvasculature and other micron-scale behavior [33,43,50,51]. The combination of a ~2.5 μm^3 voxel size with a volume sample rate of ~30 s allows for detailed views of the movement of infused particles into the brain environment. Previous work in our lab had shown particles moving through the parenchyma and the PVS at vastly different speeds by watching a plane above the point of infusion. Here, a system has been developed to track the evolution of the three-dimensional nanoparticle cloud in real time continuously throughout the entire infusion. In previous experiments, the shape, as well as instantaneous velocity and volume of the developing cloud was not obtained. This method can track the entrance of infused materials into the PVS, and follow them for short amounts of time before they exit the field of view.

Previous research lacks detailed resolution [59,60]. A more detailed understanding of the motion of therapeutic compounds injected into the brain is needed to predict whether a CED-based treatment could prove effective. The lack of understanding of infusate location during a CED infusion could be a contributing factor in diminishing the efficacy of new treatments in clinically relevant situations [61].

The presence of larger pore sizes for the ECS have been reported in [42,62]. The fluid pathway shown in **Figure 2.8** could be something as simple as a larger pore

near the site of infusion. The nature of the nanoparticle movement, in that these pathways appear to lead into PVS, indicates that they may play a role in a larger fluid drainage system. Furthermore, they may be present for the other particle sizes and types, but could not be observed due to cloud overtaking that section of the parenchyma while other parts of the infusion were imaged.

Most of the experiments done using this experimental setup involve only two channels; a red channel for the nanoparticles and a green channel for the vasculature. The system has since been upgraded to four channels, which allows for viewing of multiple infusates or illumination of other local structures. Astrocytic endfeet play an important role in regulation of the fluid moving in the PVS [43]. If the astrocytes could be visualized using a separate color, multiple infusates could be observed interacting with both the PVS and the outer "walls" of the PVS created by the endfeet. This could lead to further understanding of the role the astrocytes play in the event of therapeutics being introduced into the local environment during a CED-like infusion.

There are drawbacks to this system. The largest is the lack of imaging depth, in that we can only observe up to ~500 μm into the cortex. This limits current experiments, at least in their current state, to rodent experimentation. This drawback will be somewhat mitigated by the advent of higher-photon imaging modalities, which will allow for greater depth imaging [35]. Furthermore, the field of view in our experiments is always between 500 x 500 to 700 x 700 μm^2, which is quite limited, especially when trying to extrapolate results to a clinically relevant scale.

It is important to understand that the development of this system and experiments performed with this system are for elucidating the mechanisms that

underlie the movement of therapeutics during a CED-like infusion. We can only predict based on evidence where materials will go. By varying particle size and type, we can make general statements about the relative rates of transport within the rodent brain environment. With appropriate scaling and future investigation into transport in higher order animals and humans, it is possible that these findings will directly extrapolate, although this is purely speculative and similar investigation in higher order animals and human trials would be necessary to confirm or deny this. Further testing for comparison will be needed to determine scale up, and future experiments will be needed to determine why materials move to the places that they do at certain times. It is possible that the bulk fluid movement systems proposed by Iliff et al. [43] carry over to CED-conditions, in that the observed motion during a CED-infusion could be sum of the infusion motion and the bulk fluid movement from arterioles to venuoles in the parenchyma. Speculation like this could be further investigated by varying the influence of the bulk fluid movement system, perhaps by varying the heartrate of the animal. In future work, if it were possible to identify available PVS prior to CED-infusion, the infusion cloud morphology could be predicted in a more precise manner, and infusion characteristics such as infusion location, flow rate, and infusate type could be tuned to more effectively deliver the therapeutic.

2.5 Conclusion

Imaging of infusates has evolved in complexity in recent years. From post-mortem brain slice analysis to MRI imaging of various tracers, visualization of

transport in the brain has added to the understanding of the underlying mechanisms that govern therapeutic movement in the brain. With the development of our system, we are able to see infusates move with greater spatial and temporal resolution than what has been accomplished previously. With micron-scale spatial resolution, we are able to see the infusate enter perivascular pathways, and can discern its location as it moves about the local area. The development of this system allowed for the experiments detailed in Chapter 3 to occur, in which numerous quantitative properties of the infusion are calculated from our imaging method. These findings allow for greater understanding of therapeutic transport in the rat cortex, which can be extrapolated to higher order animals, and potentially humans.

CHAPTER 3

PROBING PERIVASCULAR TRANSPORT DYNAMICS USING IN VIVO, HIGH RESOLUTION FLUORESCENCE MICROSCOPY

3.1 Introduction

Free drugs introduced into the bloodstream are not effective for treating many central nervous system (CNS) disorders. They are prone to poor solubility, limited biodistribution, unfavorable pharmacokinetics, and rapid breakdown [63] when treating systemic diseases. The brain is guarded by the blood-brain barrier, a series of tight junctions formed by endothelial cells that line brain capillaries, which limits the compounds that can enter the brain. Small lipophilic molecules (<400 Da) and facilitated materials can cross the barrier, but most drugs introduced into the bloodstream do not readily cross.

Convection-enhanced delivery (CED) is a local drug delivery method that circumvents the blood-brain barrier by delivering therapeutic compounds directly into the brain interstitium through a catheter or needle that is implanted into the brain. CED is used in clinical trials with humans and in experiments involving animals to deliver an array of therapeutics to treat CNS disorders. One of the most innovative CED strategies involves delivering therapeutic-containing nanoparticles deep inside the brain parenchyma where the nanoparticles can release the therapeutic over long times following CED delivery. Encapsulating therapeutic compounds inside particles

protects the therapeutic against clearance during transport of the nanoparticles through the brain. Polymeric nanoparticles that have been tested in CED studies include particles composed of polylactide-co-glycolic acid (PLGA) [40,41,64,65], polystyrene [41], polycaprolactone (PCL) [64] and polylactide-PCL [22]. Liposomes [66–69], lipid based carriers [14], and iron oxide nanoparticles [70], have also been used in CED experiments.

The size of the nanoparticles has proved to significantly affect their transport through tissue with CED. Larger particles can carry a greater therapeutic payload, but transport of larger particles may be diminished due to hindrance that increases with size. Thus, a range of particle sizes has been investigated. Nance et al. analyzed the movements PEG and carboxylic acid modified polystyrene nanoparticles of 40, 100 and 200 nm to discern the effect of size and surface coatings on the transport of infused materials in cortical slices [41]. Arshad et al. developed therapeutically effective carboplatin PLGA nanoparticles with an average diameter 175 ± 40.75 nm for the treatment of gliomas via CED [71]. Bernal et al. showed prolonged survival of animals with intracranial xenografts after infusion of a mixture of 30 to 75 nm temozolomide containing iron oxide particles [72]. Krauze et al. used liposomes of average diameter 85.1 ± 37.5 nm and 79.0 ± 34.3 nm to investigate perivascular transport throughout CNS arteries upon infusion into the putamen of monkeys [34].

While the development of various nanoparticles has increased since CED was first developed, the distribution of nanoparticles after injection into the brain remains difficult to predict, especially since it may depend on the local anatomy. Gray and white matter have different diffusional resistances [73,74] and hydraulic conductivities

[75], and the presence of highly-conductive fluid pathways further complicates accurate prediction of infusate trajectory *in vivo*[33]. Numerical simulations to predict fluid flow *in vivo* have been developed and often are used in clinical trials of CED [21,22,76–78], but they include only the conspicuous features of the local anatomy, if they include any at all. Without extensive knowledge of local anatomy and variations in tissue properties, predicting the fate of therapeutics in the brain is challenging.

The inability to disperse infused material throughout the brain may be responsible for the limited improvement of patient outcome at the clinical level with CED. The PRECISE clinical trial used CED to deliver cintredekin besudotox (CB), a recombinant chimeric cytotoxin that targets and kills tumor cells that express a specific receptor found on gliomas. Results from the clinical trial showed no significant advantage in survival outcome over Gliadel wafer treatments [79]. Several potential reasons are offered to explain the failure of CED to improve patient outcomes, including variations in catheter placement, infusion rate, and total infusion volume. However, the largest factor limiting the effectiveness of CED treatment is the uncertainty of achieving sufficient concentrations of the therapeutic at distant target sites.

The goal of this work is to use two-photon fluorescence microscopy to examine the motion of nanoparticles infused in the cortex of rodents to better understand how local anatomy and vasculature influence the distribution of infused material. The imaging system described in Chapter 2 will be used to characterize the transport of various nanoparticles injected during a CED-like infusion. The studies will examine the role of size on transport of rigid polymeric particles and deformable

liposomes. By examining the locations of nanoparticles infused into the cortex at various times during an infusion, we aim to determine various quantitative features of the infusion, such as penetration distance of the particles, volume of distribution (V_D) vs. volume of infusion (V_I), and velocities of particles in the parenchyma and in the perivascular spaces. With this information, a greater understanding of where nanoparticles go during a CED infusion into the cortex can be attained.

3.2 Materials and Methods

3.2.1 Nanoparticle Preparation

Carboxylate-modified polystyrene fluorescent nanoparticle solutions (20, 40, 100 and 200 nm FluoSpheres, Life Technologies) were sonicated for 15 min. The nanoparticles were then diluted to 0.1 wt% solids in a solution of 1 wt% bovine serum albumin (BSA, Sigma-Aldrich, St. Louis, MO) in phosphate buffered saline. Nanoparticle solutions were mixed on laboratory rocker at low speed for 4 h. BSA conjugation to carboxylate-modified surface reduces surface charge of polystyrene nanoparticles, decreasing non-specific binding of the nanoparticles upon infusion into rodent brain.

Fuchsia-colored suspensions of 50, 100, and 200 nm liposomes were procured from Avanti Polar Lipids, Inc. These liposomes were formulated in a molar ratio of 55:44:1 1,2-dioleoyl-sn-glycero-3-phosphocholine (DOPC): cholesterol: Texas Red 1,2-dihexadecanoyl-sn-glycero-3-phosphoethanolamine (DHPE). The formulation

involved extrusion through appropriate filters to form liposomes of the desired size. The liposomes were suspended in buffer solution containing 10 mM 4-(2-hydroxyethyl)-1-piperazineethanesulfonic acid (HEPES buffer), pH 7.4, 150 mM NaCl, and 1 mM $MgCl_2$.

Size and surface charge were determined for the liposomes and for the polystyrene beads both before and after BSA incubation of the polystyrene beads (Zetasizer Nano, Malvern Instruments Ltd., UK). The measured sizes and zeta potentials of the particles are contained in **Table 3.1**.

Dynamic light scattering (DLS) characterization techniques are sensitive to the presence of large particles in the solution. Large particles can change the average diameter measured by the Zetasizer, which may explain the larger than anticipated average particle diameter. The hydrodynamic diameter of BSA is ~7 nm [80], and the presence of a BSA molecule surrounding the surface of the polystyrene nanoparticle helps explain the increase in the diameter of the particles when conjugated with BSA. BSA conjugation clearly reduces the zeta potential of the particles, thus helping to reduce non-specific binding once infused into the brain parenchyma during these experiments. As for the liposomes, the polydispersity index (PDI) indicates that there is a large range of particle sizes in the suspension, with the average influenced by the presence of larger particles in the suspension. Investigation into Zetasizer data indicated that for the 50 nm particles, over half were in the range of 50-100 nm.

Cascade Blue-dextran was used to track fluid motion independent of the nanoparticle motion. To do this, a “co-infusion” of nanoparticles and Cascade Blue dextran was prepared by mixing 1 wt% Cascade Blue dextran in phosphate buffered

Table 3.1: Average particle diameter, polydispersity index (measure from 0 to 1 of how wide the distribution of particles is, 0 being uniform size, and 1 being wide range of particle sizes), and zeta-potentials for all particles. Stock solutions prior to surface modification are also shown as entries for beads. Standard error of the mean (SEM) shown for particle diameter and zeta-potential. All values were measured in triplicate, giving these averages and SEM.

Particle Type	Average Particle Diameter (nm)	Standard Error of the Mean for Average Particle Diameter (nm)	Average Polydispersity Index	Average zeta-Potential (mV)	Standard Error of the Mean for Average zeta-Potential (mV)
50 nm liposome	137.3	2.42	0.181	-4.1	0.54
100 nm liposome	186.5	4.92	0.248	-3.5	0.26
200 nm liposome	246.5	11.14	0.294	-2.7	0.35
20 nm bead	29.1	0.42	0.080	-30.5	1.48
20 nm bead+bsa	50.6	0.41	0.248	-10.5	0.45
40 nm bead	49.8	0.50	0.043	-32.3	2.77
40 nm bead+bsa	75.4	0.50	0.121	-11.0	0.35
100 nm bead	108.9	0.69	0.012	-38.3	0.34
100 nm bead+bsa	131.3	0.84	0.017	-11.2	1.03
200 nm bead	179.9	1.64	0.018	-34.1	2.03
200 nm bead+bsa	207.6	0.54	0.009	-10.1	0.31

saline solution with 0.1 wt% 200 nm nanoparticle solution in a 1:4 ratio.

3.2.2 Infusion Setup Preparation

The craniotomy protocol described in Ch.2 was used here. After the craniotomy, the subject was transferred to the imaging setup. The animal was placed on a motorized stage beneath the two-photon excitation fluorescence (2PEF) microscope objective. A 4X objective (Zeiss) was used to examine the craniotomy during insertion of the CED needle. Using a micromanipulator, a fixed rod that held a needle (prepared using P-97 Flaming/Brown Micropipette Puller, Sutter Instrument) of outer diameter ~10 μm was brought into the field of view above the coverslip. The needle was then retracted, lowered, and then inserted into the brain in a direction parallel to the surface of the brain at a depth below the brain surface between 100 and 400 μm. The pipette could be seen under 2PEF due to the presence of nanoparticle solution, which was primed to the distal end of the needle. The vasculature and nanoparticles could be identified in separate channels on the imaging computer, as the blood vessels were labeled with fluorescein isothiocyanate (FITC)-dextran from a 1 mL tail vein injection, and the nanoparticles were labeled with a red (580 excitation/605 emission)-fluorescent molecule. Once the needle was in the tissue, the 4X objective was replaced by a 20X, water-immersed objective (Zeiss or Olympus).

3.2.3 Imaging Experiments

2PEF images were taken on a custom-built two-channel microscope using 100 fs duration pulses from a 76 MHz repetition rate Ti:sapphire laser system (Mira-HP, Coherent, Santa Clara, CA) pumped by a continuous wave laser (Verdi-V18, Coherent, Santa Clara, CA). Excitation wavelength was set to 800 nm, which excited both the FITC and the red nanoparticles. Fluorescence collection was achieved using a 610-nm and 530-nm bandpass filter. ScanImage (r3.8.1, Janelia Farm, USA) was used for image acquisition. High magnification images were captured with a 1.0 NA, 20x water immersion objective (Zeiss, Thornwood, NY).

Infusions were made at a flow rate of 0.2 μL/min using a PHD-2000 constant flow infusion pump (Harvard Apparatus). During the infusion, the motorized stage was used to move the animal and micromanipulator vertically under the objective. The stage was programmed to move up and down periodically. The imaging plane was fixed in space, but the relative motion of the tissue allowed the imaging plane to scan through the cortical tissue periodically. Thus, the vasculature and the infusion cloud were sampled in each plane at discrete times. The period of the stage motion ranged between 60 and 90 s. depending on the total vertical depth being imaged. The distance traveled by the stage during each half-period was 150 to 300 μm. The step size was 2 μm. At each step, 512 x 512 pixel images were captured at a frame rate of 3.15 frame per second. This resolution and frame rate were previously determined to be sufficient for viewing transport with spatial and temporal resolution that could reveal details of the infusate motion.

Multiple infusions were performed with a single animal. The edge of each infusion cloud could be seen, meaning each subsequent infusion needed to be done

where the field of view would not pick up any residual fluorescence from a previous infusion. The needle was withdrawn and reinserted to avoid any overlapping regions from a previous infusion. At the end of the experiment, pentobarbital was administered *via* intraperitoneal injection to induce euthanasia.

3.2.4 Image Analysis

2PEF imaging files were exported as multi-image tagged image file format (TIFF) stacks for analysis in ImageJ (National Institutes of Health, Bethesda, MD) and MATLAB (Mathworks, Natick, MA). Image stacks were individually loaded into ImageJ. A 1-pixel 3D median filter was used to remove noise from the images. Then, the two channels were combined into a composite image for each depth in the brain. Brightness and contrast were adjusted for viewing and data analysis. Perivascular routes and parenchymal cloud growth could be assessed using these image stacks, with perivascular routes identified as areas where nanoparticles were adjacent to blood vessels. Filtered image stacks were individually loaded into MATLAB. A threshold was calculated based on image histograms to remove background noise. Then, various quantitative properties of the infusions were measured, including average radius of the infusion cloud near point of infusion and length of visible perivascular routes.

3.3 Results

3.3.1 Nanoparticle Experiments

To gain a fundamental understanding of the movement of nanoparticles injected during a CED-like infusion, we continuously imaged nanoparticles as they were infused. This allowed us to evaluate numerous aspects of the infusion with unparalleled temporal (~30 s per recording of infusate volume) and spatial (~2.5 μm^3 voxel size) resolution. We found that nanoparticles of all sizes can travel along perivascular routes, and the presence of these perivascular routes influences the morphology of the infusion cloud. Furthermore, velocities could be estimated for perivascular pathways, which allows for direct comparison to parenchymal transport.

The sampling of the volume occupied by nanoparticles during the experiment allows for reconstruction of the cloud in ImageJ. A typical MRI reconstruction would have about 20% of the available volume samples, with significantly reduced spatial resolution. The 2PEF technique used here can accurately track the progression of the growth of the cloud, which is necessary for understanding nanoparticle dynamics at this scale.

3.3.2 Cloud Morphology

Our experiments can be viewed in two groups: "rigid" polystyrene beads of 20, 40, 100, and 200 nm diameter, and "deformable" liposomes of 50, 100, and 200 nm diameter. For the 20 nm nanoparticles and for liposomes of all sizes in this experiment, the infusion cloud closely resembled a sphere. However, for nanoparticles of larger sizes (40, 100, and 200 nm), the growth of the infusion cloud was strongly

influenced by perivascular routes. The clouds formed by the larger beads have a spherical portion indicative of isotropic growth, but they also have protrusions from the spherical boundary that lead to perivascular spaces.

Figure 3.1 depicts 3D reconstructions of infusion clouds for liposomes (50, 100, and 200 nm) and for nanoparticles (20, 40, 100, and 200 nm). Each row contains images of the infusion cloud at short, medium, and long times throughout the infusion.

The perivascular routes for liposome transport are readily visible in most of the frames for the liposomes. For example, all frames of **Figure 3.1A**, which pertain to 50 nm liposomes, show clearly defined perivascular routes extending beyond the edges of the infusion cloud. The growth rate of the cloud, i.e. the speed of the edge of the cloud, is comparable to the speed of liposomes in perivascular spaces for the short and middle times. However, for longer times, the rate of penetration of particles along perivascular routes is considerably faster than the growth of the cloud boundary. Thus, the extensions of fluorescence beyond the edge of the cloud grow in time relative to the edge of the cloud.

In **Figures 3.1B-C**, the 100 and 200 nm liposome clouds have similar overall morphologies, but the growth rate of the cloud for 200 nm liposomes is slightly less than that for the smaller 100 nm liposomes. In any event, it is clear that relatively large liposomes, i.e. much larger than the estimated average pore size (38-64 nm [39]) of the extracellular space (ECS), are able to move through the interstitial space during a pressure-driven CED-like infusion. However, liposomes of all sizes in the experiment move through perivascular spaces at greater speeds than they exhibit in the interstitium.

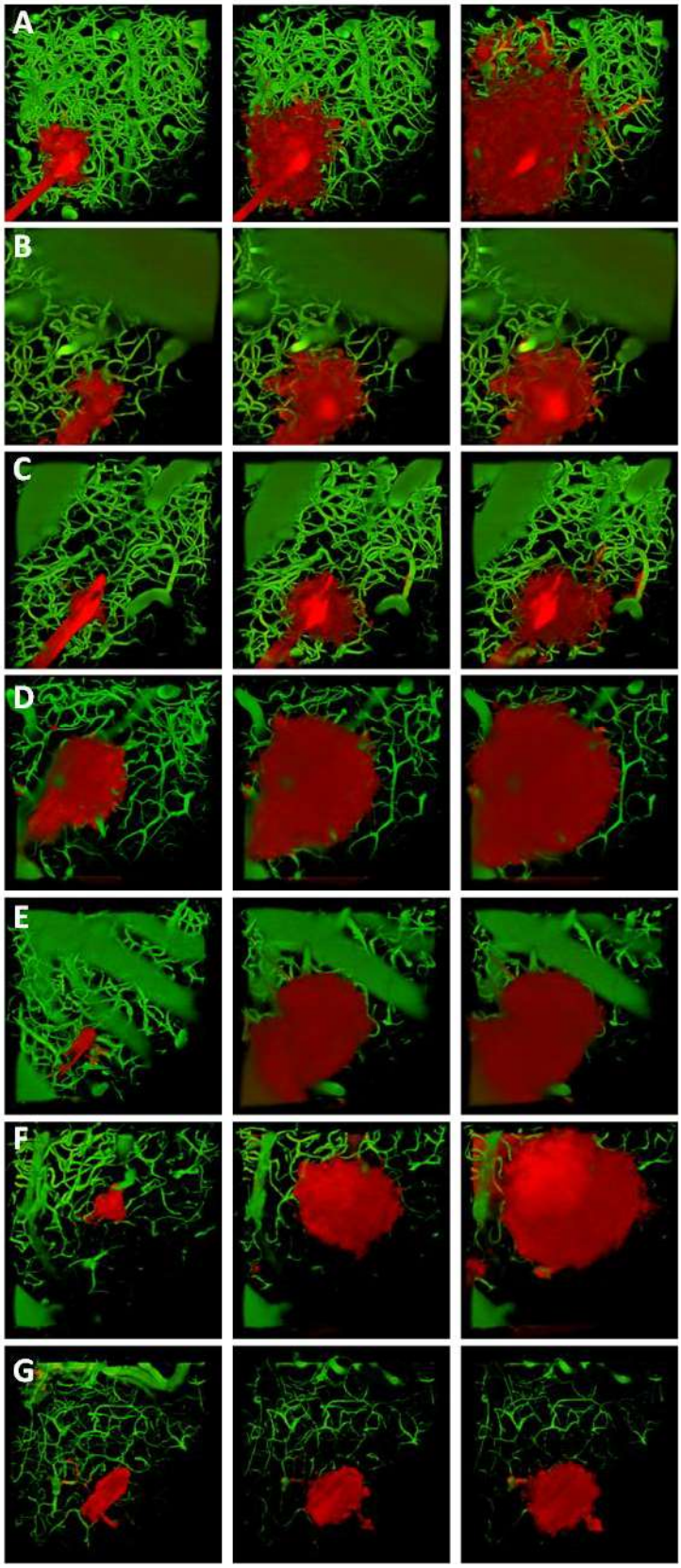
A
B
C
D
E
F
G

Figure 3.1. Time-Lapse images of infusions for each particle size and type. Each image is 574 μm x 574 μm. The infusion needle is visible in the imaging area, extending into the tissue at a ~45º angle from the bottom left corner. From top to bottom, **(A)** 50 nm liposomes, t = 48 s, 245 s, 441 s, **(B)** 100 nm liposomes, t = 32 s, 232 s, 430 s, **(C)** 200 nm liposomes, t = 40 s, 287 s, 451 s, **(D)** 20 nm polystyrene bead, t = 32 s, 165 s, 298 s, **(E)** 40 nm polystyrene bead, t = 40 s, 205 s, 369 s, **(F)** 100 nm polystyrene bead, t = 99 s, 298 s, 496 s, **(G)** 200 nm polystyrene bead, t = 205 s, 451 s, 697 s. Times were chosen to show characteristic growth of cloud. Imaging depth determined how long a volume sample would take. Images shown are 3-D reconstructions of 2-D image stacks. Green = FITC-dextran 2 MDa, red = fluorescently tagged nanoparticles.

Images for rigid nanoparticles in **Figures 3.1D-G** show that the growth rate of in the infusion cloud decreases with increasing particle size. The slowest growth rate is observed for the 200 nm polystyrene beads (**Figure 3.1G**). In this case, perivascular routes are clearly visible, especially near the infusion needle.

The data show that nanoparticles with sizes comparable to or greater than the estimated pore size of the interstitium can move through the interstitium, albeit at rates that depend on particle size. It is reasonable to expect that the motion of the nanoparticles through the interstitium is hindered in these cases. If resistance to fluid motion in the perivascular spaces outside blood vessels is less that than in the interstitial space, fluid flow could be preferentially diverted toward the perivascular spaces. This should be reflected in the trajectories of the suspended nanoparticles, too.

However, in some instances protrusions from the spherical core of the cloud were not always linked to readily identifiable perivascular spaces. In a few cases, anisotropy in the infusion cloud was not correlated with the presence of local blood vessels. This suggests the presence of higher-conductivity pathways that are not correlated with perivascular spaces. **Figure 3.2** depicts an example of this behavior. In **Figure 3.2**, a sequence of images of a loop for a 200 nm polystyrene bead infusion is shown. In column A, a perivascular route is shown in 2 μm increments, from near the top of the PVS at the top of the image sequence, and down through the PVS and associated vessel through the image sequence. In column B, there is an example of nanoparticle movement in a narrow channel without the presence of an associated blood vessel. The image sequence shows the surface of the brain in the first image, 2 μm separated images passing through the channel, and the connection of the

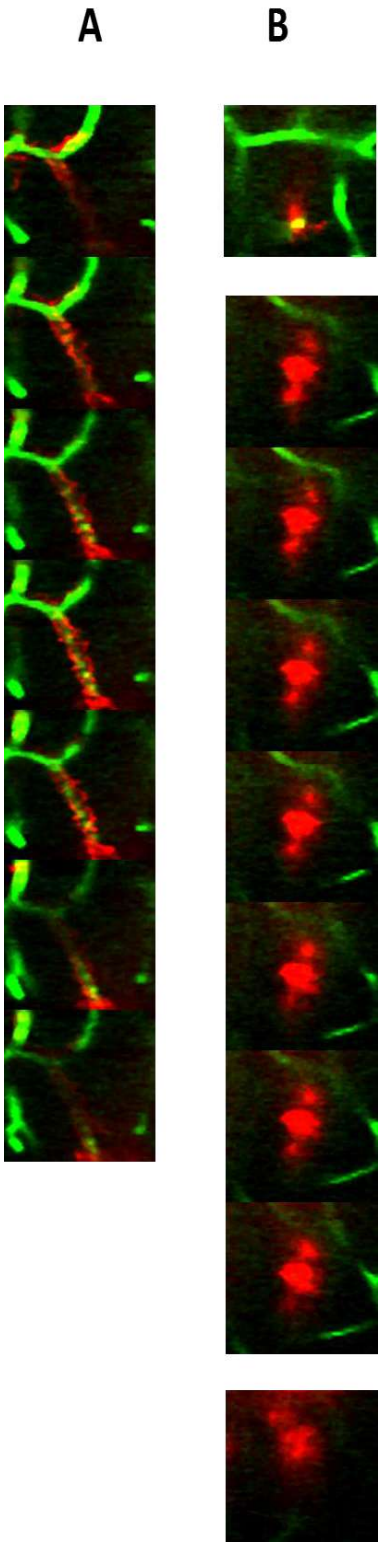
A
B

Figure 3.2. Examples of anisotropy in cloud morphology. Images shown are 100 μm x 100 μm. Green = FITC-dextran 2 MDa, red = 200 nm polystyrene beads. **(A)** Perivascular transport along a capillary. The capillary can be followed at multiple imaging depths. **(B)** Preferential parenchymal transport following a path with no identifiable blood vessel. At multiple imaging depths (2 μm apart), there are no indications of a blood vessel along the path of the particles. The particles move laterally and upward to a capillary from the point of infusion, indicative of a high conductivity pathway of egress for the particles.

nanoparticles to the cloud near the needle in the final image. The presence of this channel could be due to the location of larger ECS pores in the area, which were proposed and studied by Nance et al. [41].

3.3.3 Volume of Distribution

The volume of distribution (V_D) is the volume of tissue that contains nanoparticles. The volume of distribution is small than the infused volume (V_I) because the motion of nanoparticles is hindered, and they do move at the same speed as that of the fluid. The volume of distribution can be calculated based on the images obtained from the 2PEF. In this case, the total volume of distribution consists of two parts: the contribution from the spherical core for each infusion, which can be obtained by measuring the radius of the cloud near the needle outlet, and the perivascular routes, which can be measured using the simple neurite tracer plugin from ImageJ. All measurements are initially taken in pixels and then converted to μm^3 or μL. For the spherical portion of the infusion cloud, this calculation is trivial because the radius lies in the focal plane and the conversion from pixel to length is known. The conversion factor in the focal plan differs from the conversion factor in the vertical direction, as the voxel is a rectangular prism with a longer vertical length than in-plane length. With the correct conversion factors, we can find the true perivascular length in μm, which along with the measured PVS width and vessel radius can be used to calculate the perivascular volume for each route, using the equation:

$$\text{Volume of PVS} = L\pi(2rw+\pi w^2)$$

where L is the measured length of the PVS route, r is the measured radius of the blood vessel, and w is the measured width of the perivascular annulus. For example, for an infusion of 200 nm polystyrene beads, the measured length of a PVS was found to be 276.15 μm, the measured radius of the blood vessel was 2.14 μm, and the perivascular width w was 2.33 μm, giving a PVS volume of 13407 μm^3, or 1.34 x 10^{-5} μL.

Figure 3.3A shows the volume of distribution V_D as a function of volume of infusion V_I for each particle size. The left side of **Figure 3.3A** pertains to liposomes; the right side of the panel pertains to rigid polystyrene nanoparticles. **Figure 3.3B** shows V_D as a function of V_I for 200 nm polystyrene beads. The slope of each linear fit of the data is the V_D/V_I ratio; the average of the slopes for a particular size and type is displayed in **Figure 3.3A**. This gives evidence of the assertion that the ECS pore size plays a role in hindering the movement of particles as the average pore is approached and exceeded, as the 50 nm liposomes showed significantly higher V_D/V_I than the other two liposome sizes tested. The 20 and 40 nm polystyrene beads showed a similar average V_D/V_I, but decreased for 100 nm, and further decreased for 200 nm. The values of V_D/V_I for liposomes are between three and eight times greater than the values of V_D/V_I for polystyrene beads of similar size.

3.3.4 Parenchymal Transport

Upon entering the brain tissue, nanoparticles are hindered as they move through the ECS. All of the nanoparticles show sharp declines in initial velocity with increasing time and, thus, with increasing distance from the needle outlet. **Figure 3.4**

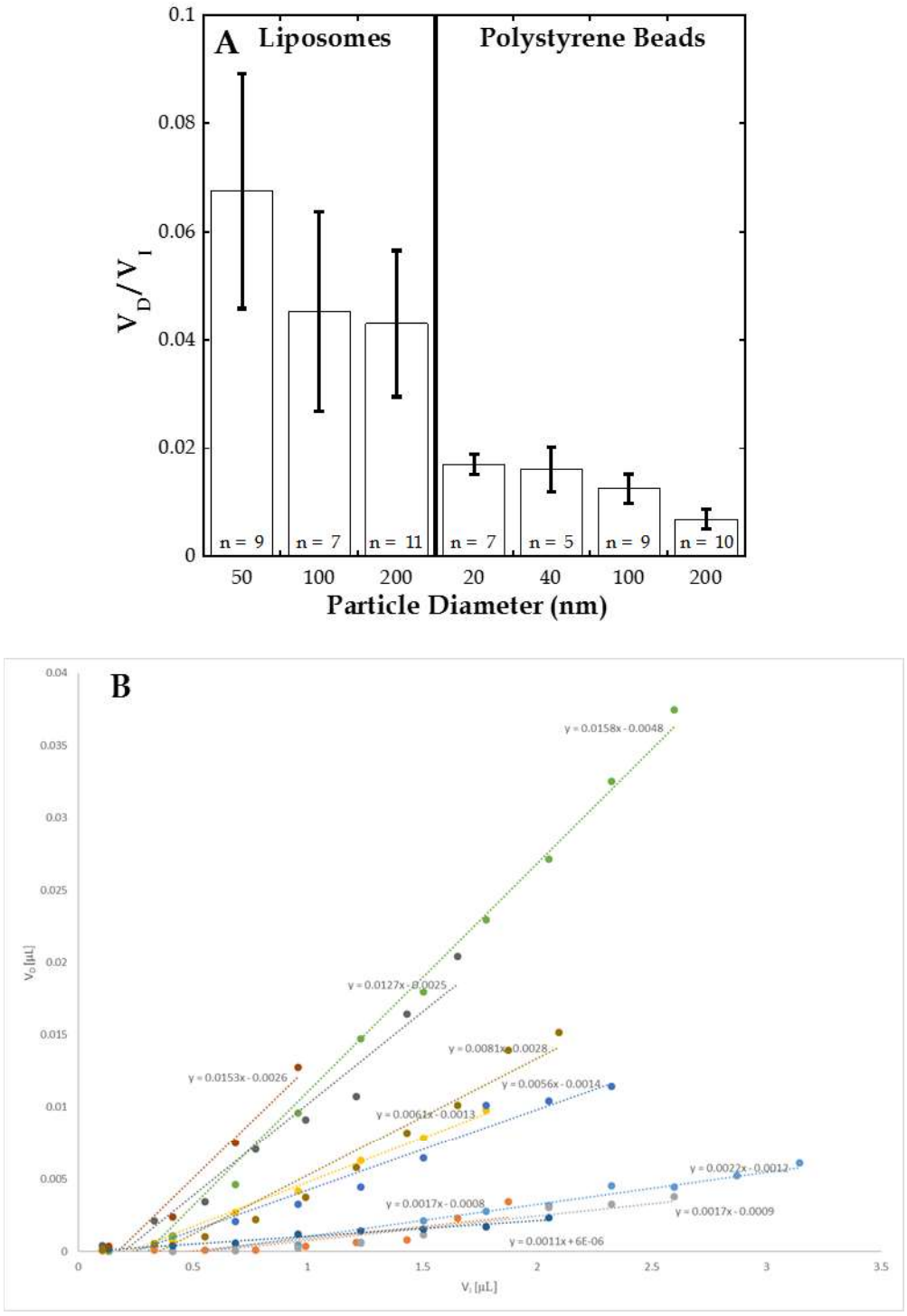

Figure 3.3. The ratio V_D/V_I for each particle type and size, and an example of V_D vs. V_I for the 200 nm polystyrene beads. **(A)** The left side of the figure shows data for

liposomes; the right side shows data for rigid nanoparticles. n is the sample size for each particle type and size. Error bars indicate ± standard error of the mean (SEM). The ratio V_D/V_I is larger for liposomes than for polystyrene particles of equal size in every case, and the ratio decreases with increasing particle size for both kinds of particles. **(B)** For 200 nm polystyrene beads, V_D vs. V_I varies linearly. Each color indicates a separate infusion. The average and SEM of the slope of the linear fit makeup the rightmost bar in **(A)**. Similar linear fits were done for each of the other particle size and type, populating the bar graph shown in **(A)**.

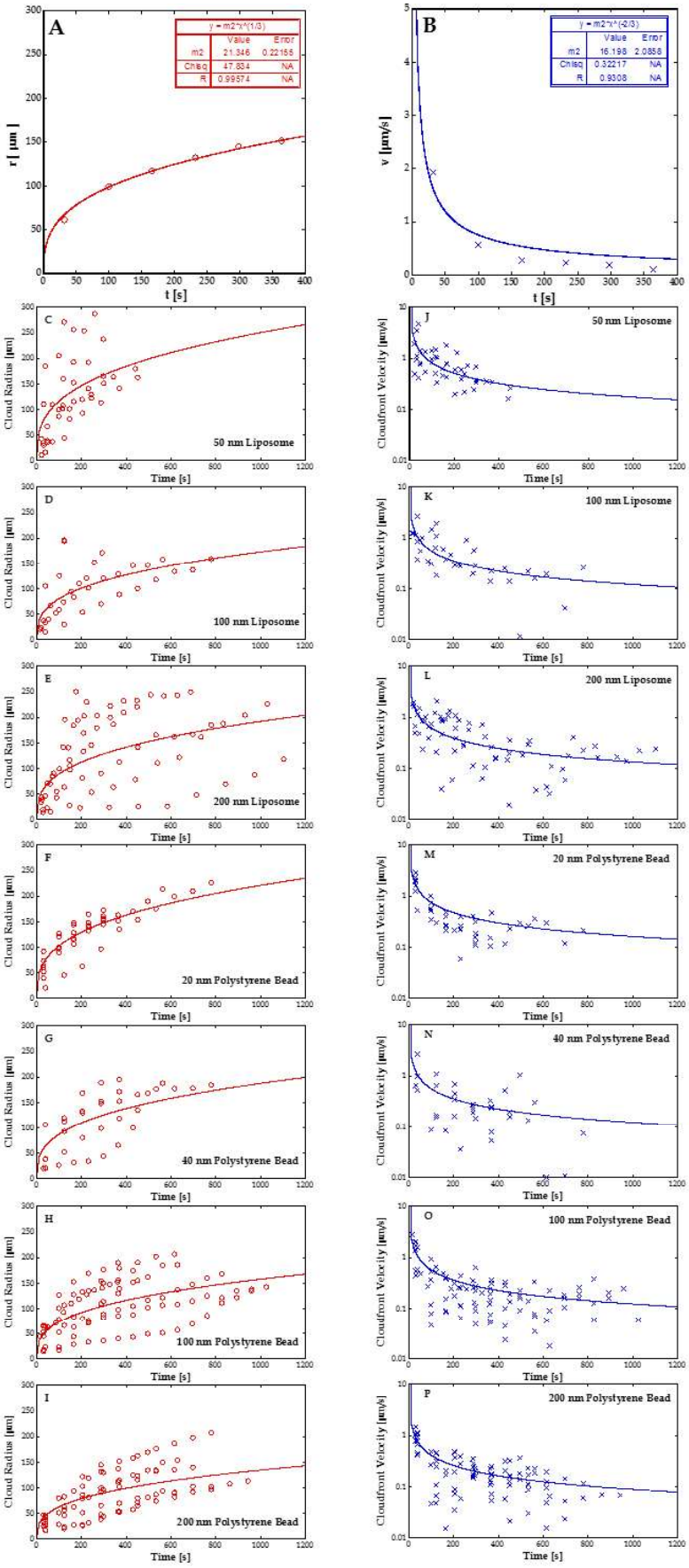
A
y = m2*x^(1/3)
Value Error
m2 21.346 0.22155
Chisq 47.834 NA
R 0.99574 NA
r [µm]
t [s]
B
y = m2*x^(-2/3)
Value Error
m2 16.198 2.0858
Chisq 0.32217 NA
R 0.9308 NA
v [µm/s]
t [s]
C
50 nm Liposome
D
100 nm Liposome
E
200 nm Liposome
F
20 nm Polystyrene Bead
G
40 nm Polystyrene Bead
H
100 nm Polystyrene Bead
I
200 nm Polystyrene Bead
J
50 nm Liposome
K
100 nm Liposome
L
200 nm Liposome
M
20 nm Polystyrene Bead
N
40 nm Polystyrene Bead
O
100 nm Polystyrene Bead
P
200 nm Polystyrene Bead
Cloud Radius [µm]
Cloudfront Velocity [µm/s]
Time [s]

Figure 3.4. Cloud radius and cloudfront velocity as functions of infusion time for various particles. **(A)** Single infusion radius vs. infusion time data with corresponding power law fit for an infusion of 200 nm polystyrene beads. **(B)** Single infusion cloud front velocity vs. infusion time data with corresponding power law fit for an infusion of 200 nm polystyrene bead. **(C-I)** Aggregate (all infusions plotted together) radius vs. time data and corresponding aggregate fit (power law fit) for each particle size and type, labeled in the plot area. **(J-P)** Aggregate cloudfront velocity vs. time data and corresponding aggregate fit (power law fit)

shows examples of the measured cloud radii as a function of infusion time, the velocity of the cloud front as a function of infusion time, and the aggregate (all of the infusions on a single plot) radius/velocity data for all infusions of each particle type. The top image in **Figure 3.4A** shows the cloud radius for a single infusion of 200 nm polystyrene beads. The data points are the measured radii at various times in the infusion, which are obtained by measuring the radial extent of the cloud in four directions about the needle tip. The fit through the data points is of the form:

$$r_{nanoparticles} = \alpha\left(\frac{3Qt}{4\pi\phi}\right)^{\frac{1}{3}} = Prefactor * t^{\frac{1}{3}}$$

where Q is the volumetric flow rate (0.2 μL/min), φ is the porosity of brain tissue (0.2), t is time and α is a coefficient representing the ratio between the measured radius of the nanoparticle cloud and the radius of an equivalent sphere having the same volume as V_D. Thus, the value of α is a measure of deviation from sphericity of the infusion cloud. However, since the nanoparticles move through the tissue with a speed that is smaller than that of the fluid, the value of α also reflects the degree of hindrance of the nanoparticles' motion. The expression above reflects a simple mass balance that equates the volume of distribution, adjusted by the tissue porosity, to the volume infused.

For smaller, unhindered particles, the infusion cloud could reflect an isotropic expansion of the nanoparticles, which would correspond to a value of unity for the coefficient α. For larger nanoparticles, α decreases in value as the size of the nanoparticles approaches the size of the pore that the nanoparticles must negotiate to move through the porous medium. Steric hindrance and non-specific binding of the

nanoparticles to cells or to constituents of the extracellular matrix can also contribute to a lower value of α. In practice, the prefactor shown in the equation can be found simply by fitting the data to the suggested scaling of $t^{1/3}$. The values for the prefactor from each fit and the measured values of α can be found in **Table 3.2**. Both aggregate data (all the infusions plotted with a single curve fit through them) and individual data averages (each infusion plotted separately, with individual curve fits) show a decrease in alpha with increasing particle size. Aggregate values found are similar to those found from averaging the individual curve fits.

The fastest traveling particles in this experiment were the 50 nm liposomes. The extent of their travel was 16% of that of an isotropically expanding, unhindered sphere over the course of the infusion. The slowest traveling particles, the 200 nm polystyrene beads, reached a distance of about 9% of an isotropically expanding, unhindered sphere over the course of the infusion. The liposomes had higher values for α than polystyrene beads of similar size, which could indicate that the flexibility of the liposomes enhanced their motion into the tissue.

Figure 3.4B shows the cloudfront velocities for a single infusion of 200 nm polystyrene beads. The velocity is calculated by dividing the change in radius by the change in time. The fit for the velocity data is:

$$v_{nanoparticles} = \frac{\alpha}{3}\left(\frac{3Qt}{4\pi\phi}\right)^{-\frac{2}{3}} = Prefactor * t^{-\frac{2}{3}}$$

Table 3.2. Power-law fit prefactors and radial growth of cloud relative to isotropic expansion of a sphere (α). Aggregate values (top) are obtained by plotting all of the infusions and fitting the power law curve for radial growth to the data, and individual values (bottom) are obtained by plotting each infusion individually and fitting the power law curve for radial growth to each curve, and averaging the values. Values for α are shown on the right, decreasing with increase in particle diameter.

Particle Type	Prefactor from Fit	α
Aggregate		
50 nm liposome	25.04	0.158
100 nm liposome	17.285	0.109
200 nm liposome	19.22	0.121
20 nm bead	22.19	0.139
40 nm bead	18.78	0.118
100 nm bead	15.79	0.100
200 nm bead	13.47	0.085
Individual		
50 nm liposome	25.86	0.163
100 nm liposome	17.76	0.112
200 nm liposome	23.59	0.149
20 nm bead	22.33	0.141
40 nm bead	19.37	0.122
100 nm bead	18.38	0.116
200 nm bead	14.16	0.089

Figure 3.4C-I shows the aggregate data with curve fit for the measured cloud radius as a function of time for the infusates, and **Figure 3.4J-P** shows the aggregate data with curve fit for the cloud front velocity. For a given time, the 20 and 40 nm beads can reach larger distances in the parenchyma than the 100 and 200 nm sizes. The smaller beads move with less hindrance than the larger beads: they move fast enough that they reach the edge of the viewing range in relatively short times, compared with the larger particles. The liposomes show similar behavior to the beads with respect to the radial behavior across particle diameter.

In every case, the velocities of the particles decreased as $t^{(-2/3)}$. In general, after the first 30 to 60 s of the infusion, the particles were moving at less than 1 μm/s speeds along the edge of the cloud. This continued to decrease with increasing infusion time. The smaller particles maintained a higher cloud front velocity for longer times than the larger particles.

The prefactors from each fit can be used to plot predictive curves for where the radius of the cloud will be for each particle type. In a similar manner, the predicted cloud front velocities can be plotted vs. time. These plots allow for direct comparison of predicted cloud behavior, and can be found in **Figure 3.5**. The aggregate prefactors are used for the plots shown. From **Figure 3.5**, the greater radius and cloudfront velocity for the 50 nm liposomes and 20 nm polystyrene beads can be seen versus the other particles.

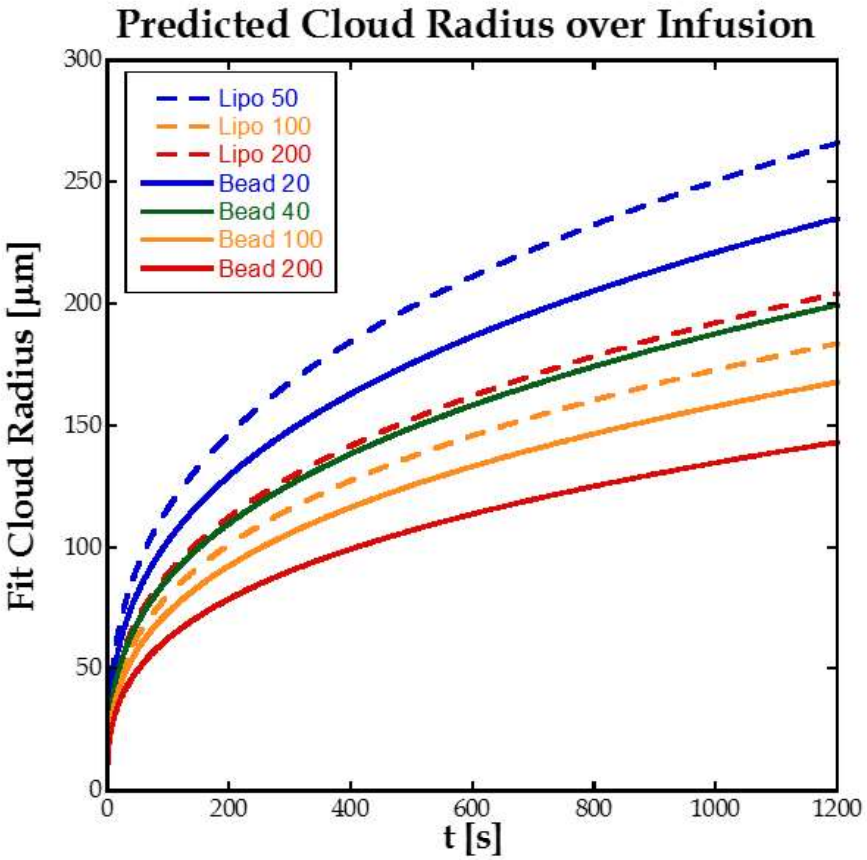
Predicted Cloud Radius over Infusion
Fit Cloud Radius [µm]
t [s]
Lipo 50
Lipo 100
Lipo 200
Bead 20
Bead 40
Bead 100
Bead 200
0
50
100
150
200
250
300
0
200
400
600
800
1000
1200

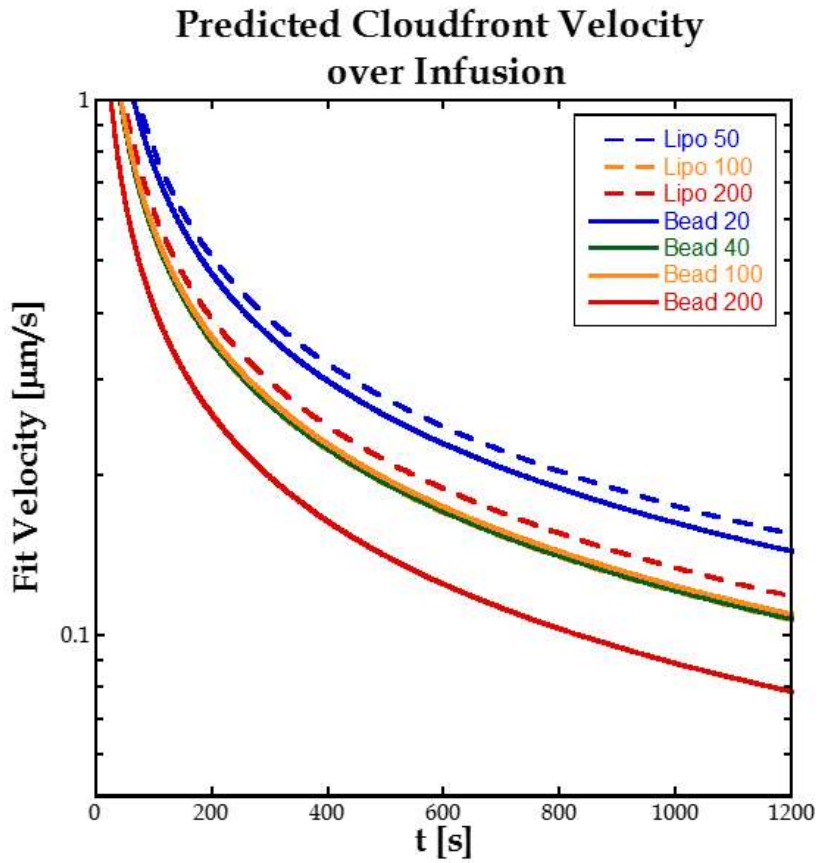
Predicted Cloudfront Velocity over Infusion
Fit Velocity [µm/s]
t [s]
Lipo 50
Lipo 100
Lipo 200
Bead 20
Bead 40
Bead 100
Bead 200
1
0.1
0
200
400
600
800
1000
1200

Figure 3.5. Power-law predictions of radius of cloud vs. time and velocity of cloudfront vs. time. Aggregate prefactors are used to generate the curves. Smaller particles maintain a higher velocity as the cloud moves outward from the point of infusion, while the velocity of larger particles decreases more rapidly with distance. Liposomes maintain a higher velocity than polystyrene beads of comparable size.

3.3.5 Perivascular Transport

Once particles reach a PVS, they follow the contours of the PVS, and penetrate the tissue beyond the cloud front. This change in transport modality leads to the anisotropy in the cloud shape, as shown in **Figure 3.1**.

Figures 3.6 A-B display histograms of vessel diameter and PVS width for every perivascular route containing nanoparticles over the course of the entire infusion. More than 90% of vessels in the imaged volume do not show evidence of nanoparticles in a PVS associated with the vessels. Some PVS were accessed readily during the first few loops of the infusion, while others required longer times for the nanoparticles to enter a perivascular route. Within the network of capillaries, arterioles/venules, and arteries/veins, between one and six vessels had nanoparticles located in a space identified as a PVS.

Figure 3.6A shows most vessels with nanoparticles in their PVS had vessel diameters less than 20 μm. This result could depend on the infusion point, which was 100 to 300 μm below the cortical surface. The nearest available PVS would likely be along a capillary. Nanoparticles did not appear to move directly toward a larger vessel if there were available PVS along a local capillary. For infusates to enter larger PVS, there needed to be larger vessels in the immediate vicinity of the infusion cloud.

Figure 3.6B shows most PVS widths are between 1 and 10 μm. Thus, the largest particles used in this experiment were considerably smaller than the smallest measured PVS width.

Figure 3.6E shows the speed of nanoparticles in the perivascular space

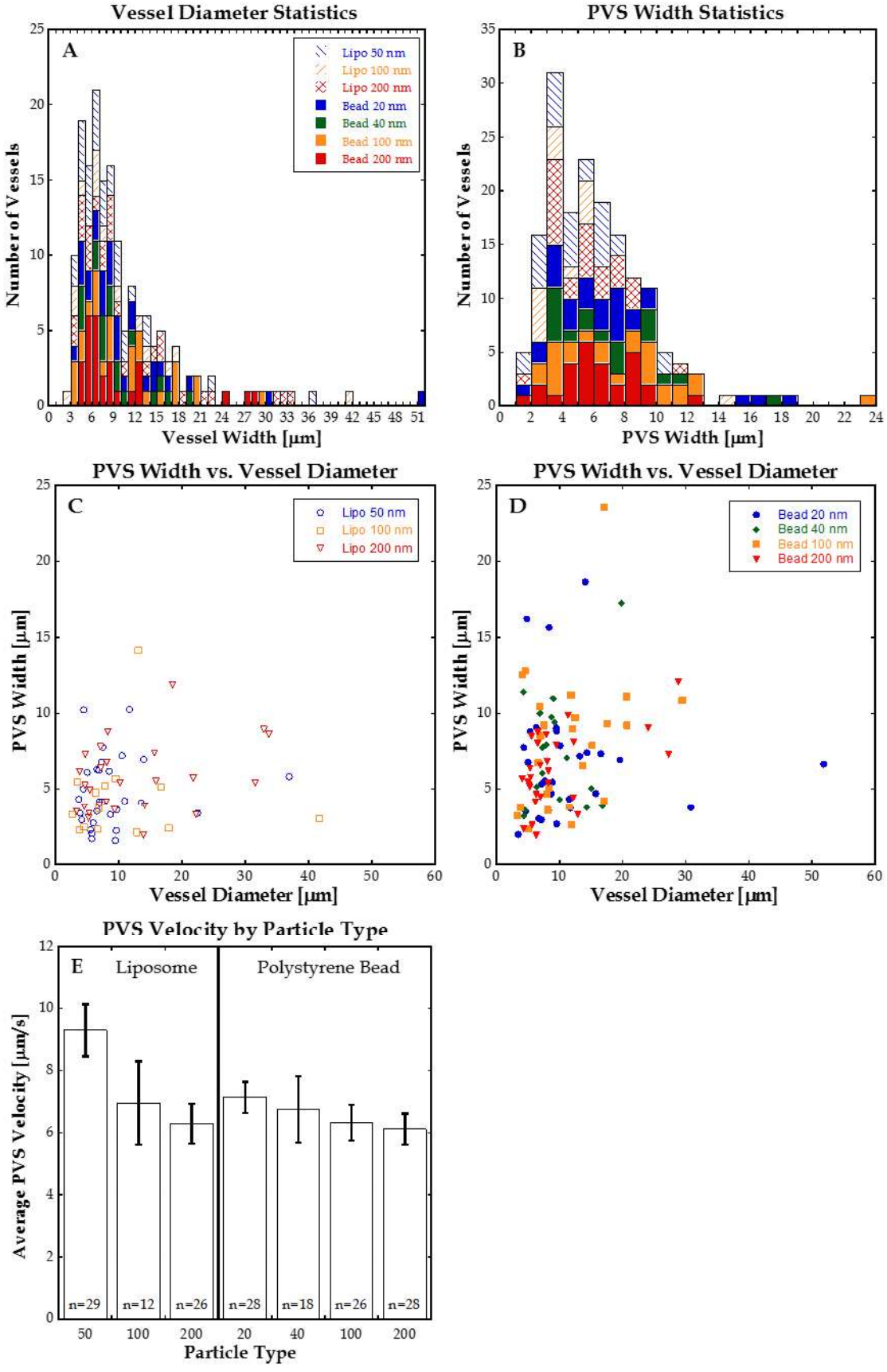
Vessel Diameter Statistics
A
Lipo 50 nm
Lipo 100 nm
Lipo 200 nm
Bead 20 nm
Bead 40 nm
Bead 100 nm
Bead 200 nm
Number of Vessels
Vessel Width [µm]
PVS Width Statistics
B
Number of Vessels
PVS Width [µm]
PVS Width vs. Vessel Diameter
C
Lipo 50 nm
Lipo 100 nm
Lipo 200 nm
PVS Width [µm]
Vessel Diameter [µm]
PVS Width vs. Vessel Diameter
D
Bead 20 nm
Bead 40 nm
Bead 100 nm
Bead 200 nm
PVS Width [µm]
Vessel Diameter [µm]
PVS Velocity by Particle Type
E
Liposome
Polystyrene Bead
Average PVS Velocity [µm/s]
n=29
n=12
n=26
n=28
n=18
n=26
n=28
50
100
200
20
40
100
200
Particle Type

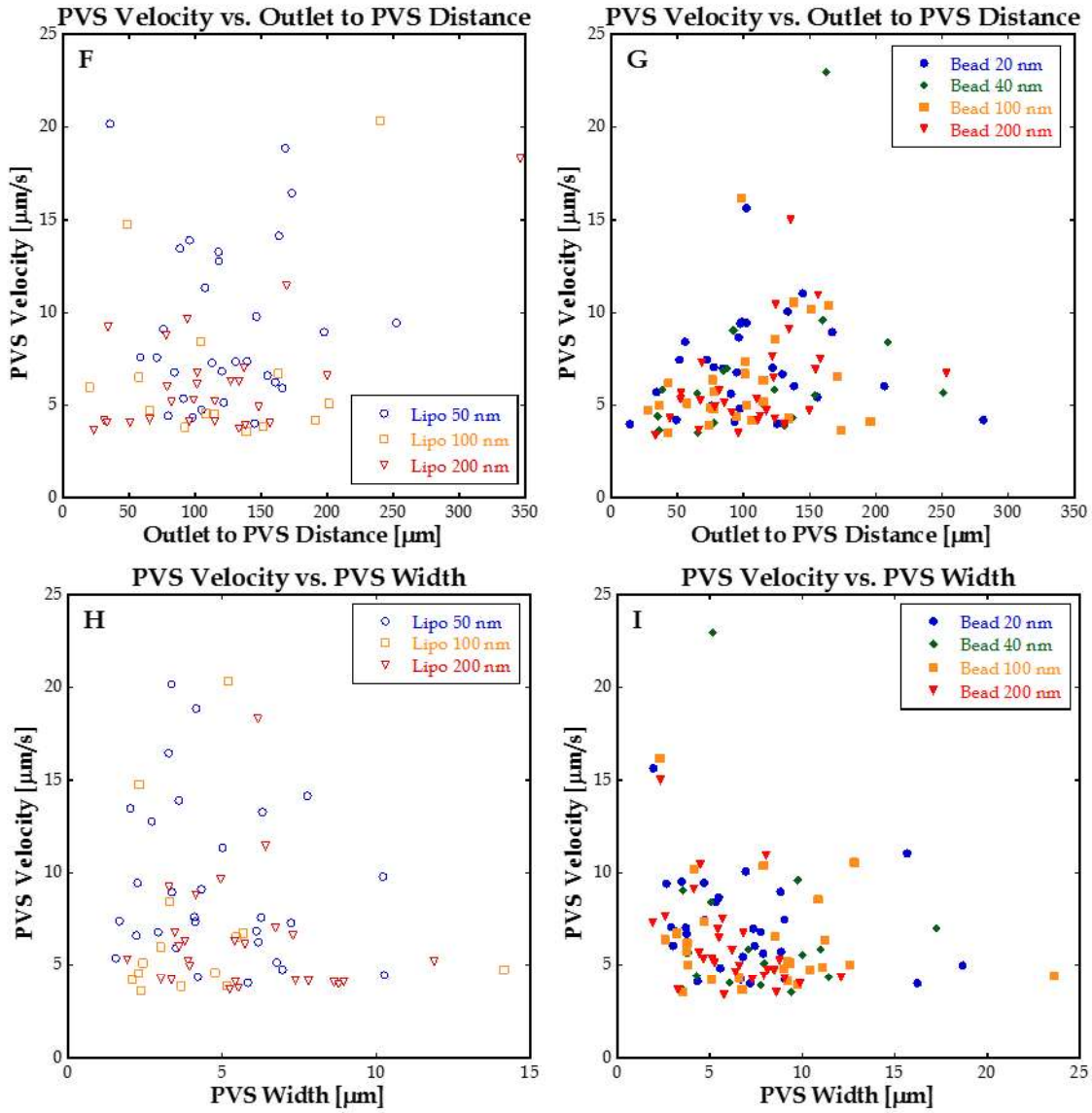

Figure 3.6. Vessel statistics and perivascular velocities. (**A**) A histogram of vessel widths that contained nanoparticles for all cases. (**B**) A histogram of perivascular space widths for all cases. (**C**) The average measured velocity of nanoparticles in the perivascular space for each particle size and type. Data to the left of the vertical line pertain to liposomes; data to the right pertain to polystyrene nanoparticles. Error bars indicate ±SEM. Sample sizes from left to right are 29, 12, 26, 28, 18, 26, 28. The correlation between perivascular space width and vessel diameter for the liposomes

(D) and the polystyrene beads **(E)**. The measured velocities of liposomes **(F)** and polystyrene beads **(G)** moving through a perivascular space as a function of distance from the infusion needle outlet. The measured velocity of liposomes **(H)** and polystyrene beads **(I)** in the perivascular space as a function of the width of the perivascular space where the velocity was measured.

averaged over all observations for a given particle type and size. The liposomes, to the left of the vertical line, show a slight dependence on size, insofar as the 50 nm liposomes moved, on the average, about 20% faster than the larger liposomes. The difference in average speed between 100 nm and 200 nm liposomes was small. The average measured speeds of the rigid polystyrene nanoparticles were practically independent of size from 20 to 200 nm. Furthermore, the average speed of all rigid nanoparticles, regardless of size, was comparable to the speeds of the 100 and 200 nm liposomes.

Figure 3.6C-D show the correlation between the measured PVS width and the measured vessel diameter. In many cases for smaller vessels, say less than 10 μm, the perivascular space width is larger than the vessel diameter. In a few cases, the perivascular space width is several times larger than the vessel diameter. Even in these cases, the motion of nanoparticles in the perivascular space followed the contours of the blood vessel. PVS width varied between 2 μm and 24 μm. In addition, the annulus surrounding the vessel, in a large proportion of the vessels, was not uniform in width along the length of the vessel. In these cases, PVS width was measured at the widest part of the PVS along the vessel. This nonuniformity is likely due to unique anatomy in the neurovascular unit. Differences in this anatomy compared to unoccupied PVS in other local vessels could be indicators of why particular PVS are available to the particles, but were beyond the scope of our experiments.

Figure 3.6F-G show the velocities of nanoparticles in perivascular spaces as a function of the distance from the needle outlet to the point where the velocity is

measured. Most values of nanoparticle speeds are between 3 and 12 μm/s, although there are some nanoparticles that move considerably faster. However, the figure shows that the speed of the nanoparticles does not appear to depend on distance from the infusion needle outlet.

Figure 3.6H-I show the velocities of nanoparticles in the perivascular space as a function of the width of the perivascular space where the velocity was measured. Most of the measured PVS widths fall between 1 and 10 μm, and the velocities are between 3 and 12 μm/s. The speeds of the 50 nm liposomes are higher than those of the other nanoparticles, confirming the higher average speed for the small liposomes shown in **Figure 3.6E**.

3.3.6 Relative Volumes

Figure 3.7A-B show the measured PVS volumes in relation to distance from the needle outlet. PVS volume is the volume occupied by the infusate along the outside of blood vessels. The equation used to calculate PVS volume was shown previously in this chapter. No trend was observed in this data.

Figure 3.7C-D show the measured PVS volumes as a function of PVS width. To better examine the relationship between the volumes of particles occupying local PVS to volume of particles in the parenchyma, we calculated the sum of PVS volumes, and divide it by the total volume of the distribution (spherical cloud volume and PVS volume). This gives us a better idea of the partitioning of the particles across the time of the infusion, for each of the particle types and sizes. In **Figure 3.7E**, we

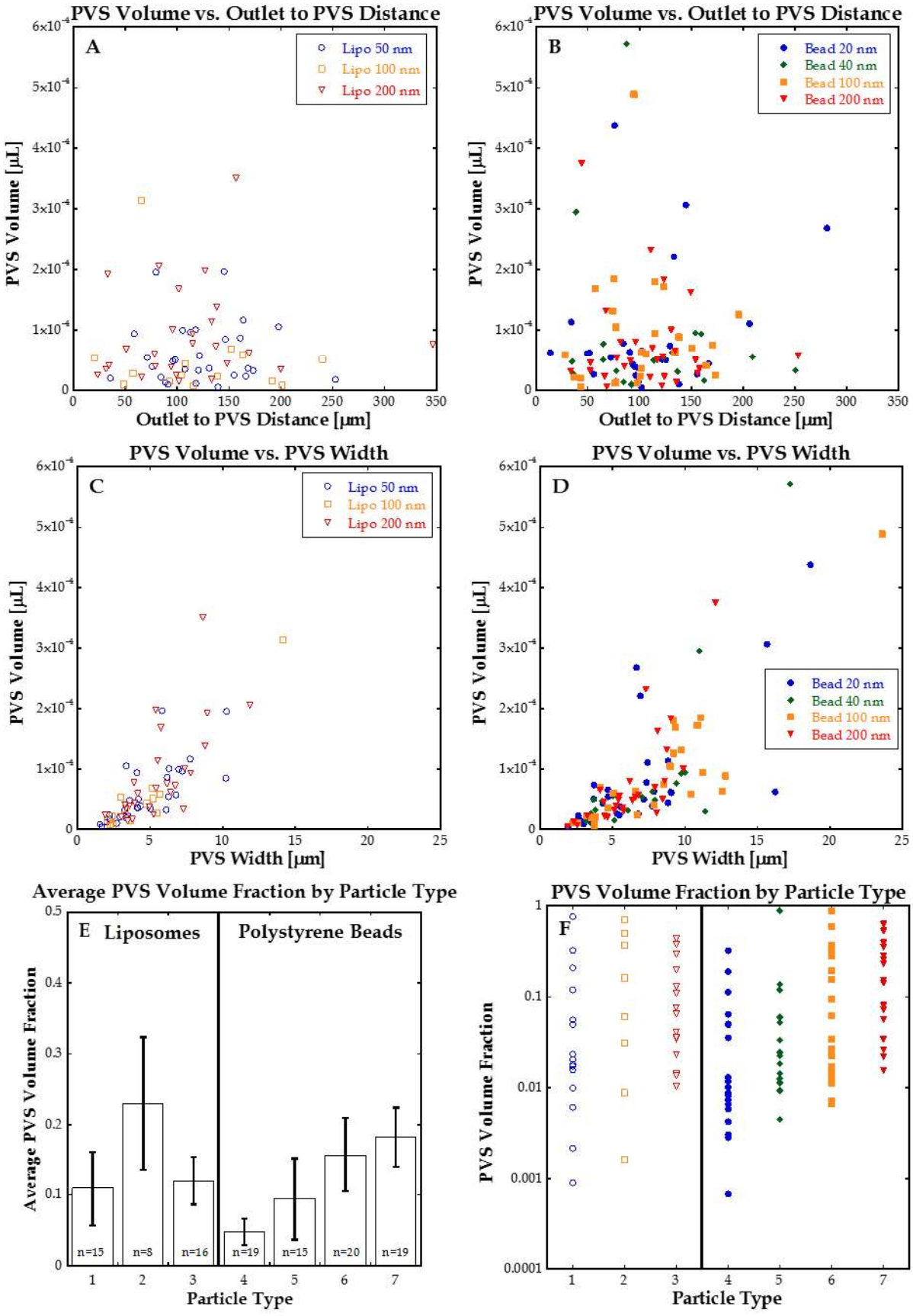
PVS Volume vs. Outlet to PVS Distance
A
Lipo 50 nm
Lipo 100 nm
Lipo 200 nm
PVS Volume [µL]
Outlet to PVS Distance [µm]
PVS Volume vs. Outlet to PVS Distance
B
Bead 20 nm
Bead 40 nm
Bead 100 nm
Bead 200 nm
PVS Volume [µL]
Outlet to PVS Distance [µm]
PVS Volume vs. PVS Width
C
Lipo 50 nm
Lipo 100 nm
Lipo 200 nm
PVS Volume [µL]
PVS Width [µm]
PVS Volume vs. PVS Width
D
Bead 20 nm
Bead 40 nm
Bead 100 nm
Bead 200 nm
PVS Volume [µL]
PVS Width [µm]
Average PVS Volume Fraction by Particle Type
E
Liposomes
Polystyrene Beads
Average PVS Volume Fraction
n=15
n=8
n=16
n=19
n=15
n=20
n=19
Particle Type
PVS Volume Fraction by Particle Type
F
PVS Volume Fraction
Particle Type

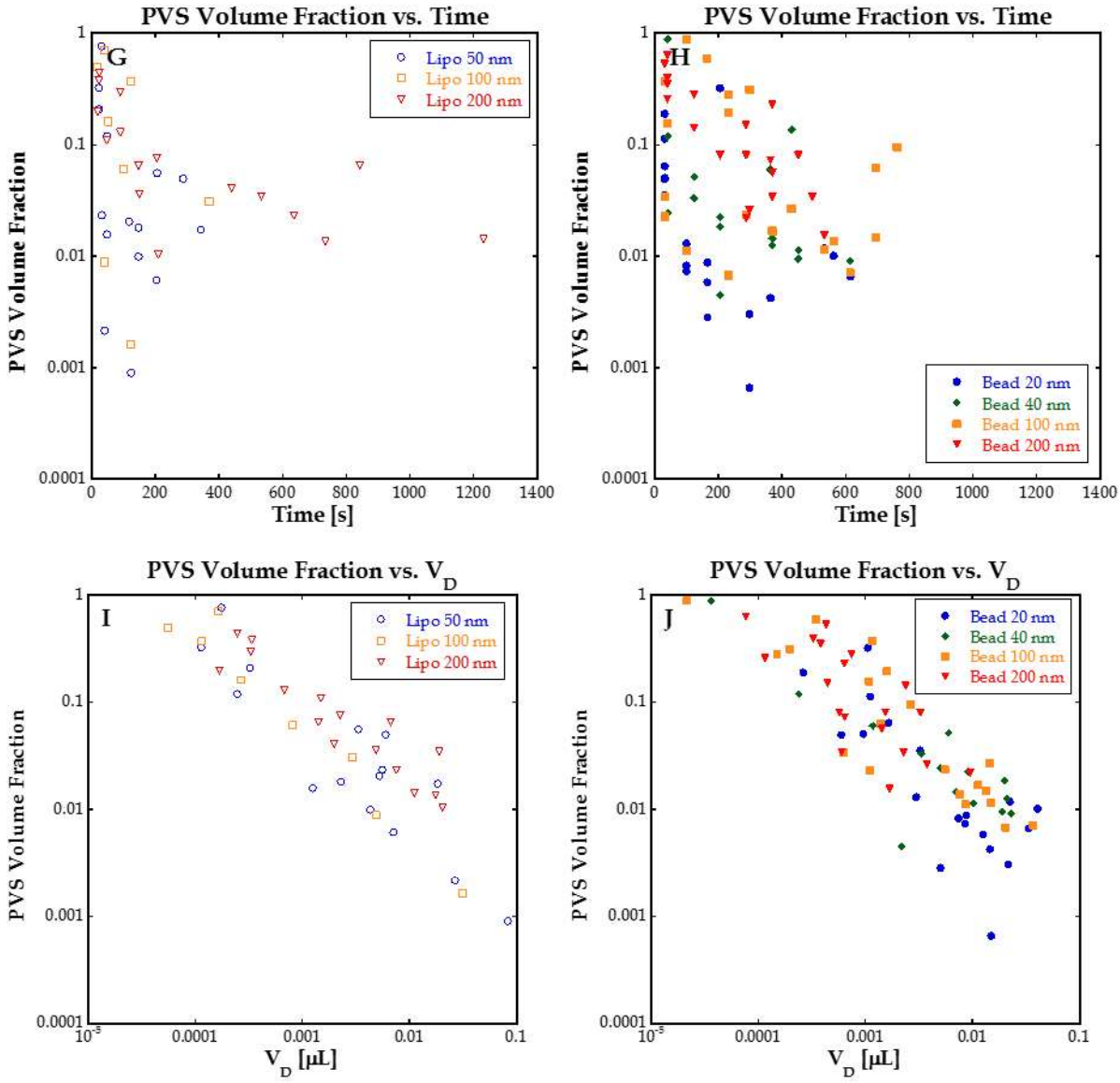

Figure 3.7. Volume comparisons for the particles traveling in the PVS and the parenchyma. **(A-B)** PVS volume versus distance from needle outlet. **(C-D)** PVS volume versus PVS width. **(E)** PVS volume to total volume ratio averaged across all times for each particle type. To the left of the line are the liposomes of size 50, 100, and 200 nm. To the right of the line are the polystyrene beads of size 20, 40, 100, and 200 nm. Error bars indicate average ± SEM. Sample size, from left starting at 50 nm liposome, to right ending at 200 nm bead, is: n = 15, 8, 16, 19, 15, 20, 19. These n

indicate total PVS volume versus total volume during a given volume sample, where multiple PVS are observed during the same sample, leading to a smaller sample size than when individual PVS are quantified. **(F)** Individual values for the averages seen in **(E)** for each particle type. **(G-H)** PVS volume to total volume ratio versus time. Smaller particle sizes saw steeper decline due to larger distribution volumes. **(I-J)** PVS volume to total volume ratio versus distribution volume observed during volume sample.

show the average ratio of PVS volume to total volume of the distribution and PVS across all times for each particle type. On the left of the dividing line, the liposomes range from about 10% to 20% PVS volume to total volume. On the right of the line, the beads range from about 5% to 20% of the total volume. The liposomes do not seem to display a trend, and the 100 nm liposomes (bar 2) seem significantly higher than the other two liposome sizes. This is likely due to a lower number of observed PVS during these infusions. A higher proportion had higher PVS volume relative to the total volume, which can be seen in **Figure 3.7F**.

Figure 3.7F shows all the individual data points where PVS volume could be compared directly to the total volume for a volume sample. The smaller particles (size 1 and 4 corresponding to 50 nm liposomes and 20 nm beads respectively) have smaller values for the PVS volume to total volume ratio, which is consistent with what is seen during the infusion. The volume of distribution is dominated by the particles in the parenchyma, or core of the cloud, at all time points, as there is less resistance to their movement in the ECS. As the particle size grows, a higher proportion of the particles from the infused volume move into perivascular routes instead of into parenchymal routes, increasing the value of the PVS volume to total volume. **Figure 3.7G-H** show the PVS volume to total volume ratio data vs. time. For the first few minutes in the infusions, it is possible for all the particles sizes to have between 20% and 80% of the total volume occupied be in the local PVS. There is a decrease in the PVS volume relative to total volume across all the particle sizes with time. There is great contrast in the way that the data points decrease for the different particle sizes. The smaller particles, shown in blue open and closed circles (50 nm liposomes and 20 nm beads

respectively), drop off much quicker than the other particles. Due to the slower parenchymal velocity of the larger particles, the PVS to total volume ratio can stay between 1% and 10% past the 10-minute mark in some of the infusions for the 100 nm liposomes and the 100 and 200 nm beads. **Figure 3.7I-J** show where the PVS to total volume data lies relative to the volume of distribution of the parenchymal cloud. Most of the data falls along a decreasing band, as the PVS volume becomes significantly less than the cloud volume at longer times. **Figures 3.7E-J** demonstrate the relative effect that the local PVS have on the infusion, in that for sizes larger than around and greater than the average ECS pore size, a significant amount of the particles are moving through the PVS rather than the parenchyma for a large portion of the infusion.

3.3.7 Co-Infusion

To observe directly the difference between transport rates of nanoparticles and fluid during a CED infusion, a small molecule tracer (Cascade Blue dextran 3kDa) was infused at the same time with a suspension of 200 nm polystyrene nanoparticles. **Figure 3.8** shows a series of images from the infusion near the needle tip. The time intervals of the images are 32, 196, and 360 s after the start of the infusion. At a time of 32 s, there is evidence that the dextran has entered the tissue, while the fluorescence of the nanoparticles appears to be confined to the needle lumen. However, at a time of 196 s extensive penetration of the dextran and the nanoparticles into the tissue is clear. At a time of 360 s, both the dextran and nanoparticles show increased penetration into

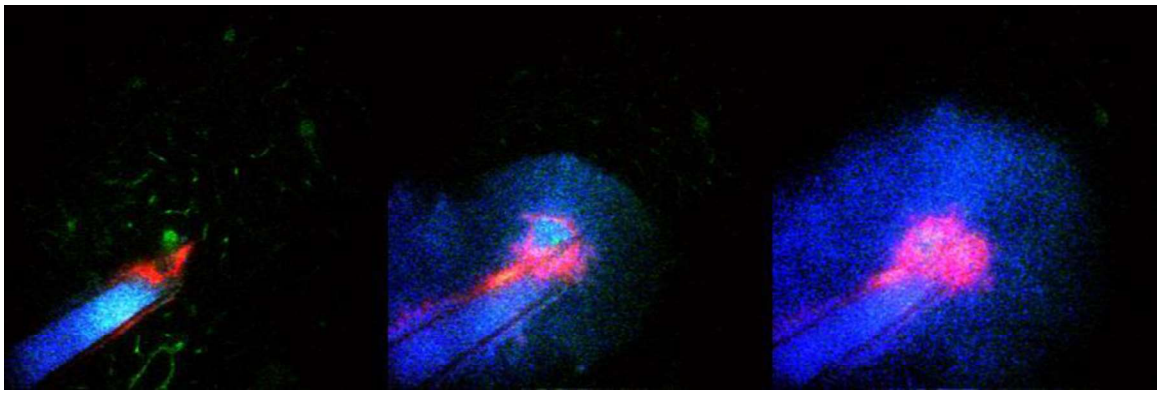

Figure 3.8. Time-lapse images of co-infusion of Cascade Blue dextran and 200 nm polystyrene beads. Images are 574 μm x 574 μm. Blue = Cascade Blue dextran 3kDa, Red = Polystyrene beads, 200nm, Green = FITC dextran 2 MDa. Imaging plane at location of needle outlet, ~200 μm below the surface of the brain. Times shown are 32 s, 196 s, 360 s.

the tissue. At 196 and 360 s that the dextran has shown greater tissue penetration than the nanoparticles. For direct comparison to the prefactor and α values for the nanoparticles, the dextran had a prefactor of 30.63 and an α value of 0.193. While this value is higher than any of the values seen for the nanoparticles, this value signifies that the dextran traveled roughly 19% of the distance of an expanding sphere

3.4 Discussion

Nanoparticles have many therapeutic uses in treatments for neurological diseases [72–74]. Nanoparticles can behave significantly different than fluid tracers or "free" drugs introduced directly into brain tissue. With these experiments, we can follow nanoparticles emanating throughout ~500 μm of the cortex. Materials introduced directly into brain tissue are hindered by the limited pore size of the ECS [46]. In a porous medium, assuming isotropic infusion, the velocity of an infused fluid varies as:

$$v(r) = \frac{Q}{4\pi\phi r^2}$$

where v(r) is the velocity as a function of radial position from the fluid source, Q is the volumetric flow rate for the fluid source, φ is the porosity of the tissue (~0.2, [75]), and r is the radial position from the fluid source. For a direct comparison to the data we collected, at a distance of 100 μm from the needle tip, the fluid velocity from theory should be 132 μm/s. We found the velocity to be between 0.4 and 1 μm/s, depending on the particle type (referring to **Figure 3.5** for estimate). For most of our experiments, we observed nanoparticle movement, knowing that the fluid containing

the nanoparticles should be moving at a different rate than the particles. To get a better understanding of relative velocity difference between the fluid and the nanoparticles, we infused a solution of the 200 nm nanoparticles with 3 kDa Cascade Blue dextran (1:3 nanoparticle solution to Cascade Blue dextran solution). Using three channels on the 2PEF setup, we could see the growth of both the small molecule (blue) and nanoparticle (red) clouds, as shown in **Figure 3.8**. The blue cloud grows much quicker, and shows up near the edge of the field of view before the nanoparticles move more than a few μm from the needle outlet. The initial fluid velocity of the Cascade Blue dextran is estimated to be ~4.8 μm/s, which is similar to the initial movement of other infusates. Furthermore, the fluid shows a drop in velocity similar to the nanoparticles, but it occurs at greater distances from the needle outlet. We chose the 200 nm beads knowing that they would likely show the greatest difference in relative velocity. With smaller nanoparticles, the movement would approach fluid-like behavior. These differences in velocity play an important role in understanding drug-delivery in vivo. With increased diameter of the infused material, moving the material from the infusion point in a CED situation becomes increasingly difficult, as the movement of the particles drops multiple orders of magnitude with increased radial position from the outlet of the infusion catheter. This limits the effective penetration distance of the larger particles for clinical purposes. The infusion rate could be increased to improve the penetration distance, but there is an upper limit to what can be achieved, depending on the catheter type. Ultimately, improvement of penetration distance and efficacy of the infused material will depend on other properties of the drug, if a larger particle size must be used for a particular treatment.

Perivascular routes are believed to be highly permeable routes for fluid flow in the brain [45]. The velocity of fluid moving in these spaces surrounding blood vessels has been estimated as 8.33 μm/s by Diem et al. [76], based on measurements of maximum distance traveled for dextrans in the brain by Carare et al. [77]. This differs by an order of magnitude from Foley et al. who approximated the velocity to be 25 μm/s [45]. We found the average velocity of the various particle sizes to be between 6-9 μm/s, as shown in **Figure 3.6E**. There is a slight decrease in PVS velocity for the increase in particle size, but it is not significant. The range of the data extended between about 3 μm/s to 24 μm/s, which indicates that both values in the literature may have been reasonable. With our extensive amount of infusions done, we could see the range of the PVS velocities, and estimate them in a more precise method. In comparison to relevant parenchymal velocity, the difference is greater. In **Figures 3.4** and **3.5**, we show the decrease in parenchymal velocity with increasing time. For most of the infusions, after an initial velocity of 0.5-3 μm/s, the cloudfront velocities drop to 0.08-0.2 μm/s. This shows that beyond a certain distance from the needle (~100 μm), the nanoparticles moving in the PVS can move two orders of magnitude *faster* than nanoparticles in the ECS for the infusion rate of 0.2 μL/min used in these experiments. For human clinical use, a higher flow rate (greater than 1 μL/min) would be used, which would allow for greater movement of the particles, and likely reduce any non-specific binding effects of the particles to the ECS. The human brain also contains a larger volume of tissue than the rat brain that the particles would need to cover, and thus higher infusion volumes would be used. From our rat experiments, it seems that these particles are forced to move hindered through the ECS (prior to entering a PVS),

which limits their use/efficacy. Long infusion times (order of hours) or other enhancement methods, such as focus ultrasound [48,78], would be necessary to increase the affected tissue.

The resolution of our setup allows for unparalleled estimation of the volume occupied by particles compared to previous work done. With the higher resolution, we can see the presence of blood vessels and other unoccupied spaces within the tissue, allowing for better estimation of the real occupied volume relative to the infused volume. **Figure 3.3A** shows the average V_D/V_I ratio for each particle size. The magnitude of these values is multiple orders of magnitude less than tracer experiments that have been done for both brain phantoms and in vivo work in the past, and about an order of magnitude less than comparable work done with nanoparticles. Zhou et al. showed for PLGA nanoparticles of mean size 71 nm ± 13 nm and 147 nm ± 27 nm a V_D/V_I ratio of 3.7 ± 0.3 for trehalose coated particles, and 0.6 ± 0.1 for standard PLGA particles [56]. We showed average values between ~0.01 and 0.02. This means that the nanoparticles are extremely hindered once entering the brain tissue, and are only occupying roughly 10% the volume of a similar nanoparticle infused in a similar manner. The methods used for determining the volume of distribution in Zhou et al. involved both PET and post-mortem fluorescence imaging, which could help contribute to the order of magnitude difference in the ratio. It is intuitive that these particles would travel slower and occupy less space than a fluid-like tracer. There is a sharp drop between the 20 and 40 nm beads, and the 100 and 200 nm particles. We theorize that this is likely due to the mean ECS pore size being somewhere between

these particle sizes, causing greater hindrance to the larger particle sizes. It is promising for clinical relevance that the 100 and 200 nm particles could move, albeit slowly, through the ECS. Furthermore, the liposomes of all sizes could occupy a larger volume of distribution than the beads for any size. This is likely due to the softer, more malleable nature of the liposome. The liposomes should be able to contort and pass through the tortuous ECS in a less-hindered manner than the rigid beads. If parenchymal delivery of a drug is desired, liposomes seem to offer advantages of both small molecules and modified nanoparticles in terms of transport. They are less hindered in the parenchyma, and can have their formulation modified to deliver specific concentration to specific areas in a local infusion. Liposomes are still susceptible to entering PVS, but as far as we can tell, anything introduced into the brain via a CED-like infusion can enter the PVS.

In our investigation of perivascular velocity, we observed that cloud formation of the larger particles is influenced by the presence of local PVS. **Figure 3.1** shows the influence that local PVS have on overall cloud growth for infusions for each particle size. We theorize that there is preferential movement of the particles in the direction of the PVS entrances due to higher convective currents in the brain, likely due to effects of a glymphatic system detailed by Iliff et al. [12]. While the conditions of the system are different (i.e. the dura has been breached), the presence of fast moving fluid pathways would have an effect similar to a fluid sink around the entrance to the PVS. More importantly, though, we have shown an important behavior that could lead to better targeting of drugs released in a CED-like infusion. By increasing the diameter of the infused particle to a size much larger than the mean ECS pore diameter, we

increased the volume of particles in the PVS relative to the particles in the ECS at the same depth within the brain. This could have an impact on the way proliferating gliomas are treated. Migrating gliomas are known to use the PVS as means of expanding in rodent model, as the annular regions are adjacent to blood vessel walls, which can be sapped by the tumor cells to procure oxygen and nutrients without the need for vascularization [79,80]. We theorize that this may be the reason vascular endothelial growth inhibitors do not limit the expansion of migrating gliomas through the PVS. Our research would indicate that combinatorial treatments, potentially combining growth inhibitors for stopping the parenchymal tumors and larger particles to specifically eradicate perivascular tumor growth, may lead to more effective clinical treatment of gliomas. While research is done to improve penetration distance of nanoparticles in the parenchyma [29,46,56], we argue that there are several effective treatments for limiting/eliminating parenchymal tumors, and getting concentrated doses of cancer-killing drugs to the migrating perivascular tumors will have a large effect on the clinical outcome for the patient.

3.5 Conclusion

In this work, we have presented an in depth look at nanoparticle dynamics introduced directly into the brain parenchyma of rats during a CED-like infusion. Through our experiments, we have elucidated quantitative features of rigid polystyrene beads and flexible liposomes, and theorized how these findings will benefit continuing clinical trials in the area. Fundamental understanding of the behavior of different infusates introduced during CED-like procedures leads to a better

understanding of where the infusions will go during actual clinical practice, and control/predictability of this behavior is paramount to the goal of effective, targeted delivery in the treatment of neurological disorders. We give strong evidence that our method for predicting this behavior is significant in the field, as it allows for higher spatial and temporal resolution *in vivo* than any previous work has achieved for studying infused nanoparticle dynamics. With continual improvements in the technology, such as higher photon imaging modalities and more responsive setups, even higher resolution will be possible at greater depths within the brain, perhaps allowing for studies to be done in other sections of the brain outside of the cortex. Furthermore, with greater imaging depth, higher animal models could be used, such as porcine or primate, which would allow for testing of CED-like infusions closer to those done in humans. The method used would still be the same, but the experimental parameters, such as flow rate and size of needle used, could be augmented to resemble those used in humans.

CHAPTER 4

MODELING DRUG DELIVERY AT AN INTERFACE USING AGAROSE GEL PHANTOMS

4.1 Introduction

Infusing therapeutic-like materials into gel phantoms that mimic live tissue properties plays an important early step in development of a treatment for treating CNS disorders. Finding materials that behave similar to live tissue and are robust, realistic, and cost-effective became necessary in the early 2000's, as there was no standard for evaluating CED infusions *in vitro*. Chen et al. presented the similar characteristics between 0.6% agarose gels and pig brain tissue, as well as compared various infusion mediums for mimicking brain tissue [81]. In the following years, agarose gels became the standard for *in vitro* modeling for infusions in brain tissue, and was used for a variety of purposes. Hardy et al. investigated the V_D/V_I relationship for varied molecular weight tracers of gadolinium-tagged polylysine, finding a deep decrease as for higher molecular weight tracers [24]. Vazquez et al. evaluated polymer-coated cannulas that reduced backflow using agarose gels [82]. Casanova et al. looked at the relationship between needle insertion speed on the prevalence of backflow for varied needle sizes, and found that slower insertions into the agarose medium yielded larger backflow distances along the needle cannula [83]. Regardless of how well the agarose gel phantoms function as live tissue surrogates, they remain as

an option for initial investigation of infusion parameters with certain therapeutics.

Both the brain microenvironment and tumor microenvironment present a complex challenge for the delivery of therapeutics. The tumor microenvironment has been shown to have lower mean ECS spacing than in normal tissue [40], leading to greater steric hindrance on the particles that approach the pore size. Increased concentration of agarose leads to decrease in pore size for the gel [84]. To gather insight into the movement of tracer particles near a tissue interface, we created an infusion setup that allowed us to infuse materials near the interface of agarose with varied concentration. The movement of our tracer particle, Evan's Blue Dye with conjugated albumin, penetrated significantly less into the higher concentration of agarose than in the lower concentration. The concentration of the tracer molecules dropped sharply at the interface of the two gel layers. Varied flow rates showed different concentration profiles for the infused tracer. While rigorous measurements were not made across a number of times of infusion, flow rates, and various infusates, the studies presented in this chapter allow for insights into the infusion near an agarose gel interface, which may influence *in vivo* studies near the edge of a particular region of the brain.

4.2 Materials and Methods

4.2.1 Agarose Gel Preparation

For all weight percentages of agarose in water (0.2-0.6), agarose was measured out

and added to volumetric flask or beaker. Solution was made by addition of distilled water. Agarose would not completely dissolve in the vessel, and thus heat was applied while the mixture was stirred. Temperature of the mixture was monitored via thermometer, as to not reach the boiling point. Once the solution became clear, indicating complete dissolution of the agarose, the vessel was removed from heat, and the stirring rod was removed. The mixture was then transferred to a custom plexiglass container while still at the high temperature. The vessel containing the initial, higher concentration layer of agarose was placed in a refrigerator to allow setting and hardening of the gel. The second layer could then be prepared using a similar method. Once the second layer solution was heated and ready to be poured, the first layer in the plexiglass container was removed from the refrigerator. The second, lower concentration layer was poured directly onto the first, higher concentration layer, and returned to the refrigerator to solidify.

4.2.2 Infusion Setup

The plexiglass container with multiple layers of agarose was moved to the area of an infusion pump. A capillary tube of 1 mm outer diameter (0.87 mm inner diameter) was lowered through a port in the roof of the plexiglass container into the agarose gel. Plastic tubing connected the capillary tube to a 3 mL screwtop syringe with an adaptor to feed the tubing into. An infusion pump (Harvard Apparatus PHD2000) was used to deliver 0.2% Evan's Blue dye (EBD) in water solution at various flow rates into the agarose gel. A picture of the experimental setup can be

Figure 4.1.

4.2.3 Concentration Determination of Standards

To be able to estimate the concentration of EBD solution in the agarose once infused, a standard curve for the EBD was created. To do this, one-inch diameter clear plastic dishes were filled with 0.2% - 0.01% EBD solutions, and laid on a light source in an isolated area of the room. Pictures were taken from the same height (6" above sample), angle (looking directly down at sample), and camera settings for each of the sample. The pictures were loaded into ImageJ, where a line was drawn across the center of the dish. The intensity profile for this line was averaged, giving a single value for the light intensity for each concentration of EBD solution.

In our experiments, after infusion had occurred, we would cut out a rectangular cross section of the gel layers distributed evenly across the point of infusion. The thickness of the gel was similar to the depth of the dish used to create the standard curve, about 1 cm. The section of the gels would then be laid on the light source. Pictures were again taken in the manner in which the standard curve was generated. With the aid of the standard curve, we were able to translate the light intensity values from the gel section to estimates for the concentration of EBD in the gel at any point along the cross section.

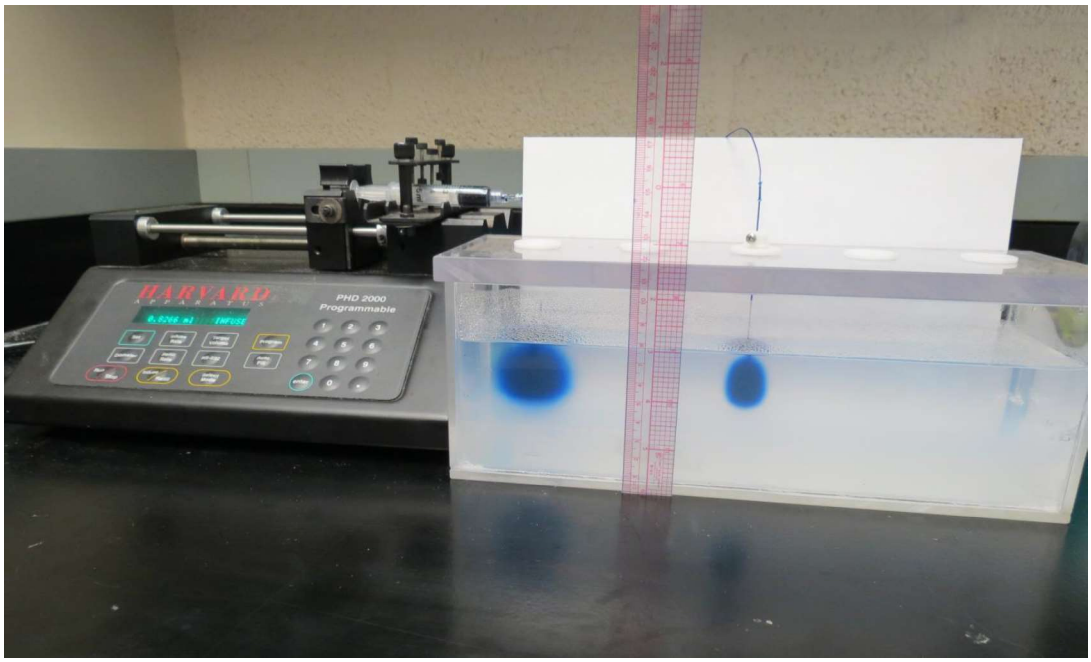

Figure 4.1. Photograph of experimental setup for agarose experiments. The Harvard Apparatus infusion pump introduces drives the compression of a syringe. Result is constant flow of Evan's Blue dye into the agarose gel in the container on the right.

4.3 Results

4.3.1 Tracer Experiments

In order to better understand concentration differences near an interface, we injected Evan's Blue dye, a small molecule, into layered agarose gels of varying wt% agarose. The agarose gel phases varied between 0.2 wt% to 0.6 wt%. The consistency of the gels varies greatly across this range, with 0.2% being loose and closer to water than 0.6%, which is rigid and closer to a solid polymer. All experiments done were for preliminary purposes only, as part of Cornell's Learning Initiative in Medicine and Bioengineering (CLIMB) GK-12 program. Overall, after significant work into developing a stable procedure, multiple infusions indicated that the switch from lower concentration agarose gel to higher concentration agarose gel inhibited movement of tracer molecules. This indicates that drug molecules introduced into an environment with local changes in porosity could be significantly hindered and act in unpredictable ways.

4.3.2 Time Evolution of Evan's Blue Dye Infusions

Agarose gel can be thought of as a roughly "ideal" medium, in that the variation in properties of the material from location to location do not vary on the macroscopic scale in which the experiments are conducted. The gels are composed almost entirely of water by weight, with the pore size far exceeding the size of the

infused molecule, Evan's Blue dye. Once the infusion cannula is introduced into the gel and given time to relax, the EBD is introduced into the medium via a constant flow rate infusion pump. The cloud morphology shifts from teardrop to spherical as time progresses. An illustrative example can be seen in **Figure 4.2**. At early times (within a few hours), the growth appears as a teardrop. By **Figure 4.2D**, which corresponds to roughly 2.5 hours into the infusion, the EBD has reached the interface, and continues to proliferate beyond the interface into the higher concentration gel. At this time, it is difficult to discern any change in the growth of the cloud between the two layers. By the end of the infusion, in **Figure 4.2F**, the difference in cloud shape between the two agarose layers is not discernable. After given significant time post infusion (20+ hours) for diffusion to occur in **Figure 4.2H**, the difference is more noticeable. At a higher flow rate, the difference in cloud shape between the two agarose layers is evident, as shown in **Figure 4.3**. This image shows the two layers at ~5 hours into a 3 μL/min infusion. The yellow curves indicate the outer perimeter of the cloud growth; the red line highlights the interface. The EBD in the bottom layer (0.6% agarose) forms a hemisphere of smaller radius compared to the hemisphere in the top layer (0.2% agarose). The effective porosity of the higher concentration gel is lower, leading to lower permeability for the EBD molecules.

4.3.3 Standard Curve

In order to estimate EBD concentration in different layers of agarose, we generated a standard curve. **Figure 4.4A** shows the curve that is generated from the

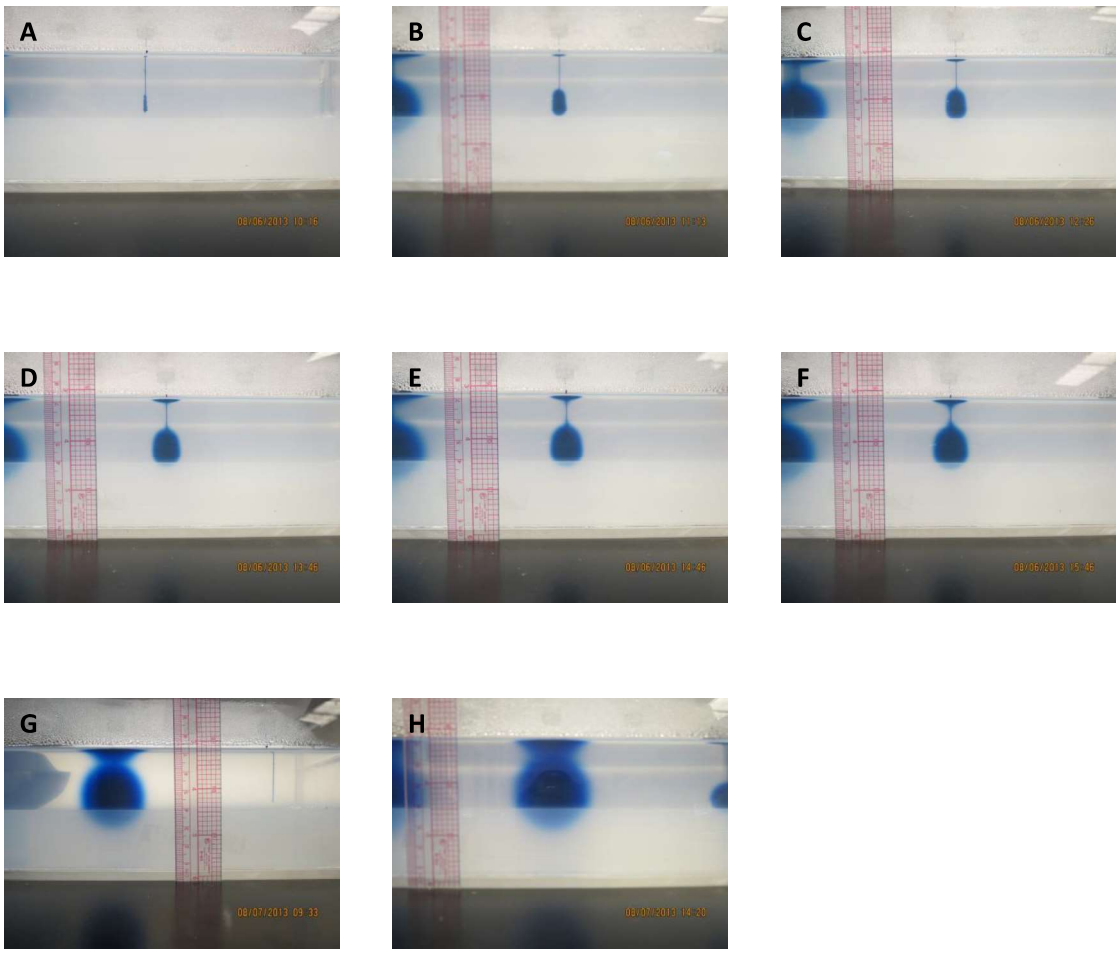

Figure 4.2. Time-lapse images showing single infusion cloud growth over time for 0.2%/0.6% gel. Times of the images are as follows: **(A)** 3 min **(B)** 1 hour **(C)** 1 hour 13 min **(D)** 2 hour 33 min **(E)** 3 hour 33 min **(F)** 4 hour 33 min. **(G)** and **(H)** show longer time points once infusion cannula was removed, at 23 hour 20 min for **(G)** and 28 hour 7 min for **(H)**.

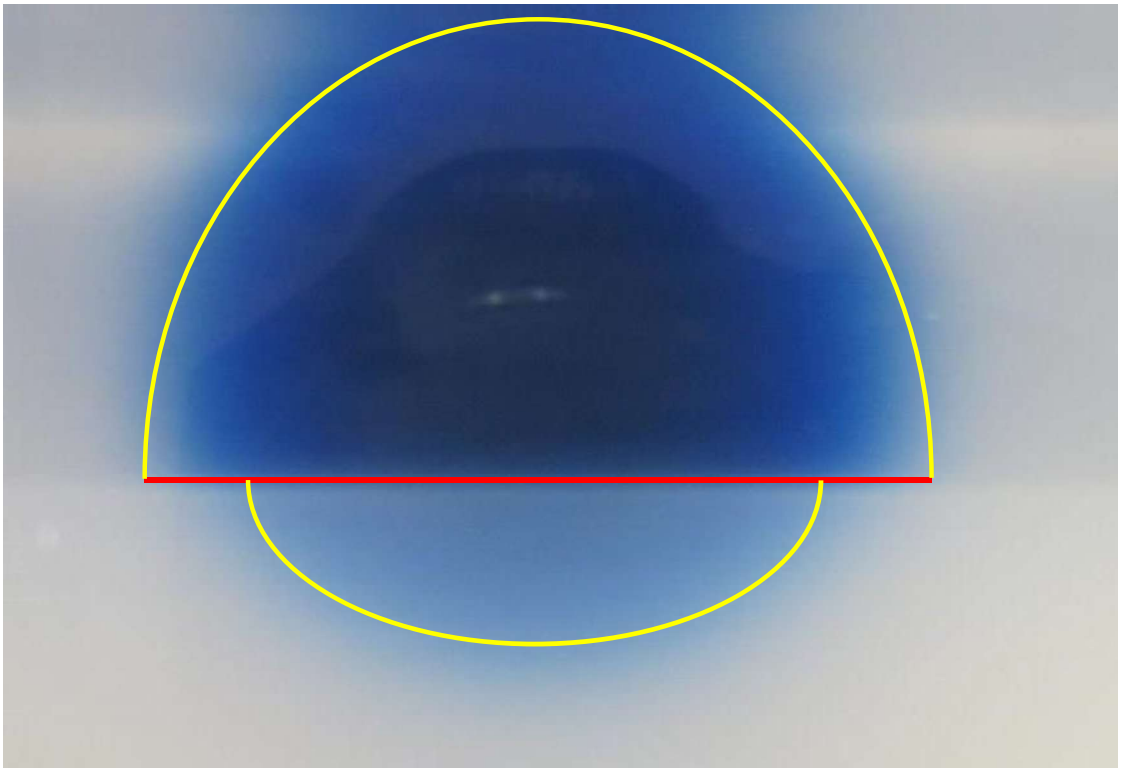

Figure 4.3. Close view of an infusion, near the interface. Yellow curves indicate outer region of the cloud in both gel phases; red line indicates interface.

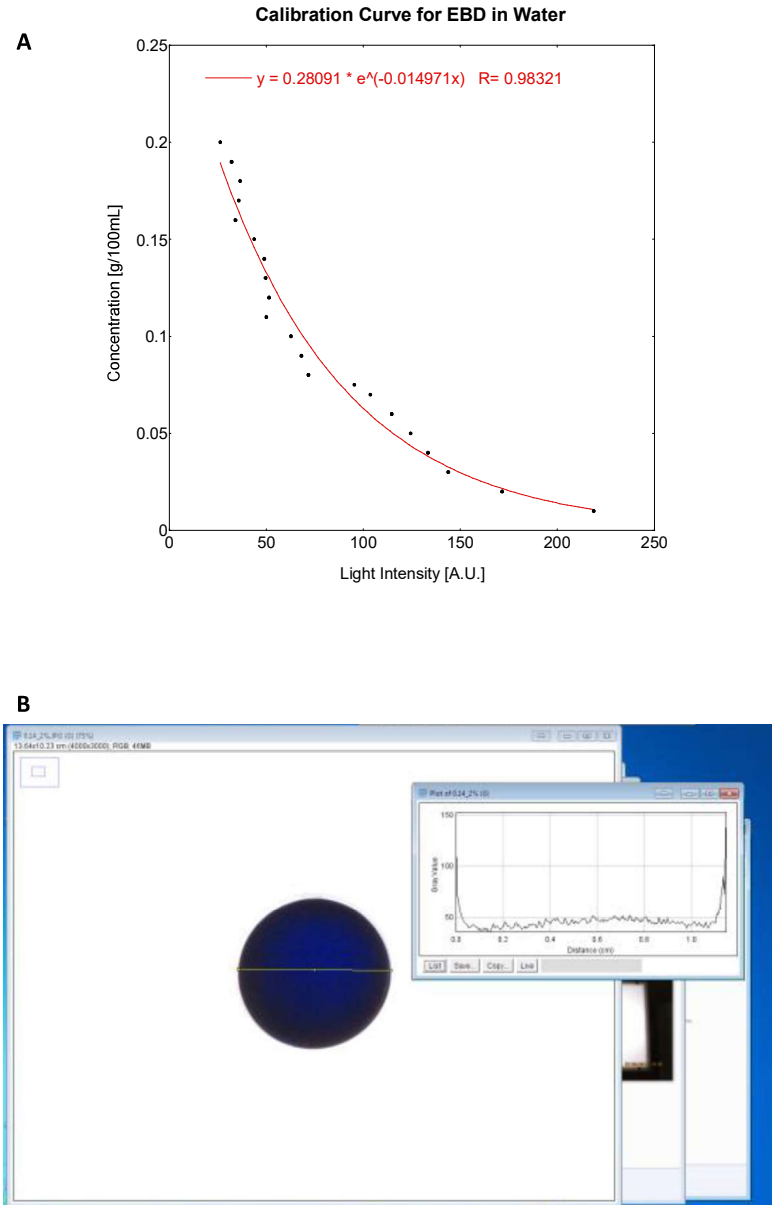

Figure 4.4. Standard curve and sample from curve procedure. **(A)** Exponential fit for standard curve data. Good linear fits could not be attained across all data. **(B)** Use of ImageJ to detect light intensity values of Evan's Blue dye standards for generation of data points on standard curve.

sample data taken. An exponential fit was used to better fit the data, as linear fits could not accurately capture the trend in the data. **Figure 4.4B** shows a sample concentration of EBD being measured in ImageJ. Higher concentrations of EBD allowed less light to pass through, leading to lower intensity values as concentration increased. Three samples of known concentration were used to test the validity of the standard curve, which correctly predicted each.

4.3.4 Thin Slice Concentration Profile

Figure 4.5 shows a thin slice of an infused gel encompassing the point of infusion for 0.3%/0.4% gel layers and its corresponding concentration profile. No noticeable difference in cloud shape can be seen between the two layers in **Figure 4.5A**. The presence of the interface can be seen in the concentration profile in **Figure 4.5B**, as around a position of 0.75 cm, the concentration of EBD drops rapidly, corresponding to the higher concentration of agarose.

4.3.5 Varied Flow Rates in Higher Concentration Difference Gels

Porcine animal models and human clinical trials are capable of handling higher flow rates with limited backflow. To investigate differences in concentration profiles with respect to flow rate, we created gel layers of 0.2% on 0.6% agarose, and injected EBD at both 1 μL/min and 3 μL/min. A total volume of 1 mL was infused for both infusions (with significantly different times for the total infusion). **Figure 4.6** shows

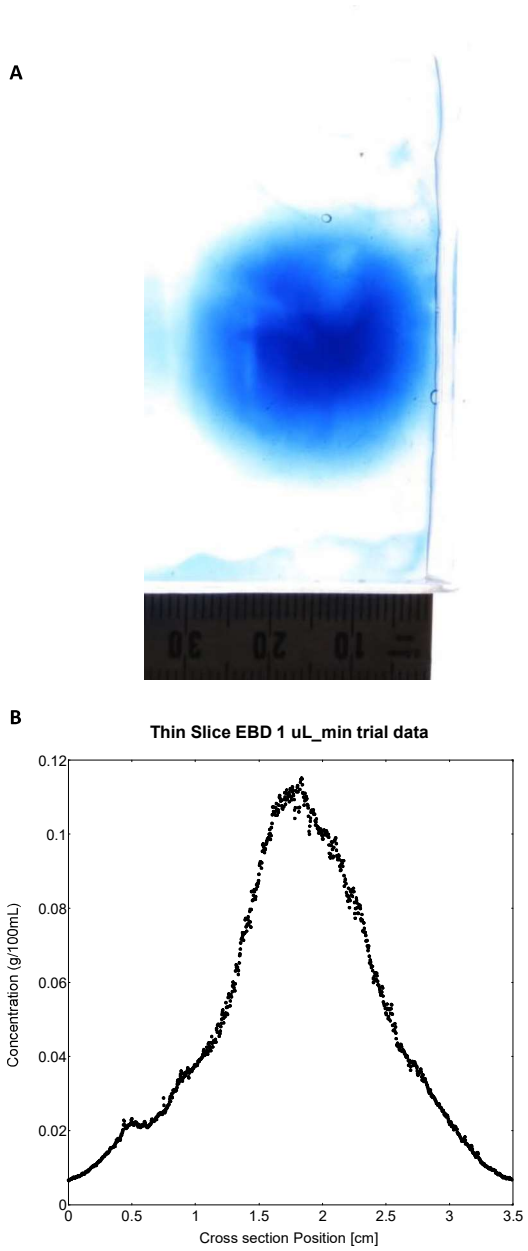

Figure 4.5. Sample experimental data for agarose experiments. With the exponential fit from the standard curve, we could estimate the concentration of an infusion cloud from a thin slice near the center cross section. **(A)** Thin cross section of a 1 μL/min infusion in 0.3%/0.4% agarose gels. **(B)** Concentration profile for same infusion. Steep drop on left half of curve indicative of interface.

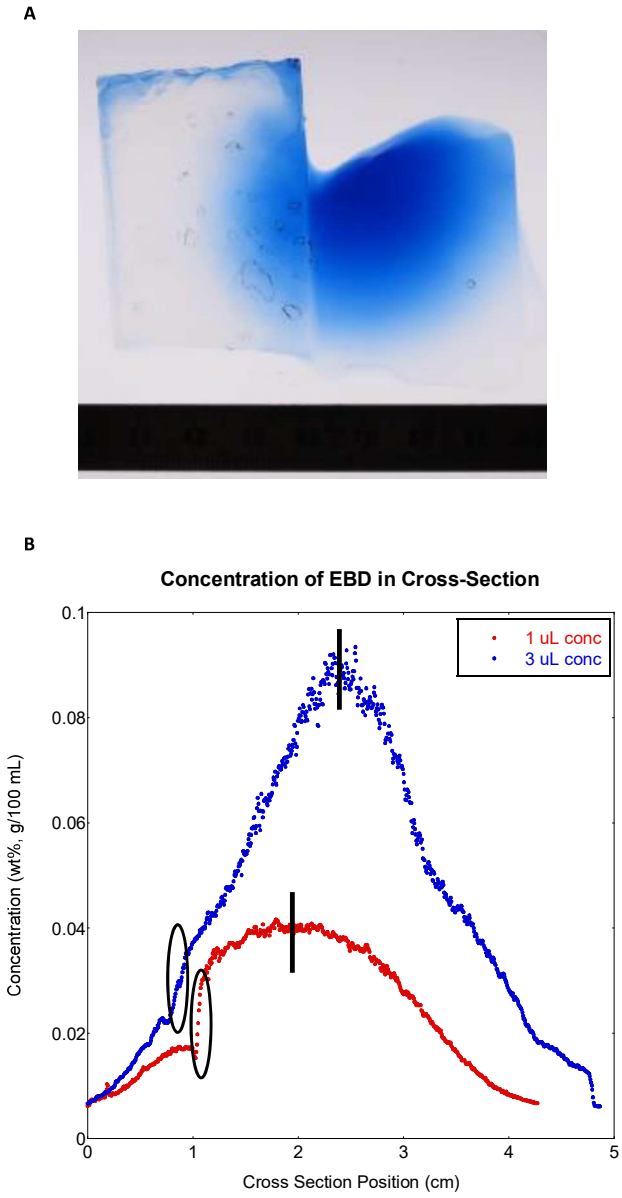

Figure 4.6. 0.2%/0.6% gel interface shows steep decline in concentration across the interface for multiple flow rates. **(A)** Sample thin slice from center of 3 µL/min infusion. **(B)** Concentration profiles for 1 µL/min and 3 µL/min infusions. Steep drop in concentration at interface is more prominent than in 0.3%/0.4% gel sample, shown before.

the thin slice from the center of the 3 μL/min infusion with its corresponding concentration profile. In **Figure 4.6A**, the slice is missing a piece of the layer, as the 0.2% gel commonly falls apart. The centerline is intact and allows for estimation of the concentration profile, which is shown in **Figure 4.6B**. The drop circled on the 3 μL/min blue curve signifies the interface, and is relatively broad when compared to the drop at the interface for the 1 μL/min red curve. The blue curve for the higher flow rate shows a higher concentration at all distances from the point of infusion (indicated by the line) than the lower flow rate. The lower flow rate, despite the lower peak concentration, resembles convective behavior, as the peak is broad for a large portion of the cross-section. The higher flow rate would in theory show a similar broad concentration profile while in a single layer. The times of infusion are significantly different, and more infusion time (and thus varied infusion volume) may be necessary in order to achieve a peak resembling convective flow from the cannula outlet. Compression of the local medium could be causing lower proliferation of the dye out into the gel, further reducing the concentration beyond the point of infusion.

4.4 Discussion

Agarose gels provide a means of simulating brain tissue *in vitro* [24,78,81]. Through the use of agarose gels, initial characterization of an infusion setup can be performed. We used layered agarose to simulate an interface between two mediums with different mechanical characteristics. In general, these infusions behaved more "ideally" than the infusions discussed in chapter 3, in that the infusate proliferates

isotropically into the agarose. The lack of blood vessels and other properties discussed in chapter 3 allows the infusion cloud morphology to become predictable. From these initial findings, we can influence translation to *in vivo* animal studies, and in theory, clinical trials.

Upon crossing the interface into the higher agarose concentration gel, the infusate experiences greater hindrance to movement, limiting its penetration further. The pressure gradient felt by the infusate near the interface is significantly less than near the needle outlet, but the immediate restraint shown between the horizontal expansion across the interface demonstrates this hindrance in **Figure 4.3**. In addition to loss in penetration depth, the concentration drops across the interface. **Figures 4.5B** and **4.6B** both show a distinct drop in concentration near 1 cm on the cross section position. While concentration profiles are not discussed in detail in chapter 3 for the infusions (due to fluctuation in power levels in the imaging of the stacks), the images near the needle tip, for the smaller sizes of the polystyrene beads, displayed similar behavior to the lower flow rate data shown in **Figure 4.6B**. The concentration stayed at near max concentration until toward the edge of the cloud, where it dropped off rapidly. The infusions in the rat brain were done at lower flow rates than those done in the agarose gel, which may be necessary in reducing compression of the gel (or tissue), which could further restrict movement, as the average pore size will likely drop if the local medium is compressed.

4.5 Conclusion

While agarose has many uses, and acts as a decent surrogate for brain tissue, it lacks the fine details and numerous additional complexities of real tissue. For the purpose of working with an "ideal" system for the first steps of characterizing an infusion system, agarose can be appropriate. We showed a method of layering agarose gels for the purpose of creating an interface between the gels. Infusion near this interface may give indications as to what happens to therapeutics near a tissue interface in the brain. We showed that when a tracer molecule encounters an interface with a higher concentration of agarose, the movement slows down drastically, and the accumulation of tracer molecules in the higher agarose medium drops significantly from what is found in the lower concentration of agarose. This could have important implications when infusions are done near the interface between different sections of the brain in the treatment of various CNS afflictions, and needs to be taken into account when trying to develop a more effective treatment.

CHAPTER 5

CONCLUSIONS AND FUTURE WORK

This dissertation aims to give insight into the underlying mechanisms behind therapeutic transport in the brain. This is done through the development of a fluorescence imaging method for sampling the infusate volume with high spatial and temporal resolution. While our experiments do not allow for control over the infusate distribution during a convection-enhanced delivery, they do allow for better prediction of where therapeutics of various sizes and types will go during the infusion. We show how infusion behavior can be greatly influenced by the presence of perivascular spaces surrounding local blood vessels, and discuss how the presence of the spaces might influence therapeutic distribution in clinical practice. This final chapter will discuss the context of this work, and provide future direction for these studies.

In chapter 2, the development of our imaging system is discussed in detail, and we detail the process of gathering data, processing said data, and extracting quantitative features. The imaging setup involved opening a craniotomy in the skull of an anesthetized rat, placing the rat on a motorized stage beneath the two-photon optics, and imaging various depths within the cortex of the rat while the stage oscillated toward and away from the objective. This allowed for collection of emitted fluorescence from the entire infusion cloud as it was being infused. To the best of our knowledge, no other studies have attempted to image the micron-scale movements of infusates in the rat cortex in this fashion. Two-photon fluorescence imaging techniques have been used for imaging in other related studies [33,43], but don't view

the entire infusion cloud as it enters the tissue. Magnetic resonance imaging has been used to view entire infused volumes [30,60], but it lacks the resolution that we can achieve. Our imaging system is limited to the cortex, as this type of imaging does not allow for imaging beyond ~500 μm into the brain. Imaging infusions into other parts of the brain could reveal other behavior, but the technology is currently limited. Higher photon imaging modalities will allow for deeper imaging into the brain, but it may not be possible to image beyond a few microns with this technique. As MRI technology improves, it may become easier to image infusions into various parts of the brain with resolution similar to what we were able to achieve in the cortex.

In chapter 3, we discuss the imaging of various infusates using the two-photon imaging system developed in chapter 2. Therapeutics have been in development for uses in CNS disease, but the actual treatment of patients has not improved. We believe that this is due, in part, to incomplete understanding of the factors influencing infusion cloud growth during convection-enhanced delivery. With the two-photon imaging method described in chapter 2, we infused fluorescently-tagged polystyrene beads and fluorescent liposomes of various sizes below, around, and exceeding the size of the space between cells in the brain.

By watching the growth of the infusion cloud, we were able to view where the infusate went in real time. For smaller particles, the movement was less hindered by the size of the pores, leading to larger infusion clouds in shorter time spans. Larger particles experienced great resistance to movement, limiting their penetration into the tissue, even at long infusion times. The liposomes, even at larger sizes, were able to behave as though they were smaller, penetrating further into the tissue than their

polystyrene bead counterparts. We catalogued all of the radial expansions and cloudfront velocities for each infusion, and fit this to power-law expressions from theory. Our results matched intuitively with what we predicted would happen, in that the flexibility of the liposomes allowed them to proliferate further into the tissue than their rigid polystyrene bead analogs. We compared these parenchymal transport rates to perivascular transport rates, which could be traced because we could see the progress of the infusate in perivascular spaces from our imaging. We found much higher movement speeds in the perivascular spaces than in the parenchyma, and the particles in the perivascular spaces moved within a 3-12 μm/s range for all particle sizes, which is consistent with values given in [85] for para-arterial drainage. Furthermore, there did not seem to be any effect of the pressure gradient from the needle outlet on the perivascular speed.

We calculated the volume of infusate distributed in the parenchyma and the perivascular spaces. We found that, as particle size increased for both particle types, the volume of particles in the perivascular spaces relative to volume of particles in the parenchyma increased greatly. The larger particle sizes maintained a higher value of this ratio into the infusion, meaning that for infusions involving larger particles, the perivascular routes are allowing significant egress for the particles, which needs to be accounted for when performing convection-enhanced delivery in the clinic. In addition, we successfully co-infused a solution containing a smaller molecular weight dextran and 200 nm polystyrene beads. As expected, the dextran moved much further during the infusions than the polystyrene beads.

These studies could be continued in a few directions. Experiments could be

done to infuse larger polystyrene beads or liposomes into the rat cortex using the same imaging setup, in an attempt to find an upper limit for what could be infused into the parenchyma. Other nanoparticles could also be used. Co-infusions could be done with solutions containing multiple types of particles to see if similar partitioning behaviour can be achieved to what we saw with the dextran and polystyrene bead solution. Repeat experiments could be run for the infusates used, but a dye to label local astrocytes could also be applied so that we could observe what was occurring with the astrocytic endfeet near the perivascular entrances. This would give insight into conformational changes in the endfeet setup near the PVS entrance, perhaps indicating if they are acting as a gate or changing in position to allow more or less fluid to enter over time.

Of particular interest to the author would be to use our system to do infusions with therapeutic like particles in the rat cortex with implanted tumor xenografts. The protocol for this system would take some time to develop, but something like what Baker et al. use in [86] would be a good starting point. The goal would be to see if the infusate acts different near or in the tumor xenograft, and if we could modulate the partitioning of the infusates to choose parenchyma or perivascular routes based on size, major breakthroughs in treating recurrent glioma could be achieved, at least in animal models.

In chapter 4, we discuss a set of studies done with agarose gels of various concentrations. By layering the gels, and infusing near the interface of the layers, we can simulate the movement of therapeutics near a biological interface *in vitro*. While the setup is rather rudimentary, the ideas behind it could lead to more complexity if

more studies were to be done. We captured infusion data for a few different gel layers and flow rates, and were able to back out the concentration profiles for the infusions. Our results indicated a drop in concentration across the gel interface, and the penetration into the higher concentration gel (lower porosity) was reduced for the dye used. If these experiments were to be continued, higher gradient in agarose concentration across the interface could be used to investigate larger hindrance on the infusate. More flow rates could be used, and repeat experiments could be used to gather statistical data for the preliminary data gathered here. Nanoparticles could be used, and co-infusions could be run, similar to those done in chapter 3, to see if a similar partitioning behavior can be achieved.

APPENDIX

CODE DEVELOPED FOR CALCULATING VARIOUS QUANTITATIVE PROPERTIES FROM IMAGE STACKS

```
%Written by: Justin Rosch

%%%%%%%%%%%%%%%%%%%%%%%%%%%%%%%%%%%%%%%%%%%%%%%%%%%%%%%%%%%%%%%%%%%%%%%%%%%%%%%

% %Notes from volume_calculator_v8
% %Version 1 converted from testing_imread code on 10/13/14
% %Last Updated 5/10/15
% %v4 has pressure gradient based on fake velocity
% %v5 has pressure gradient based on real time velocity
% %v8 has slice volumes

%%%%%%%%%%%%%%%%%%%%%%%%%%%%%%%%%%%%%%%%%%%%%%%%%%%%%%%%%%%%%%%%%%%%%%%%%%%%%%%

%Current Version == analysis_v1_0
%Converted from volume_calculator_v8
%Last Updated 5/31/15
%v1_0 has a few goals

    %first installment of surface area calculator
    %Need to threshold better--updated 4/29/15
    %Fix information loss through binary masking the data--need to convert
    %before volume summation--better attention to units
    %gets rid of pressure gradient terms in calculation
    %NEED TO WRITE DUPLICATE CODE FOR SWITCHED CHANNELS--this version is
    %for red channel 1

%%%%%%%%%%%%%%%%%%%%%%%%%%%%%%%%%%%%%%%%%%%%%%%%%%%%%%%%%%%%%%%%%%%%%%%%%%%%%%%


clear all
clc

%Open the monitor frames
%figure(1)
%figure(2)


time = 0.0001;
%Loop information ******USER CHANGE THESE******
flowrate = (0.2e-3)/60; %um^3/s
porosity = 0.2;
G = 1; %FIX THIS
kappa = 2e13; %um^4/(N*s)
mu = 9e-16;  %(N*s)/(um^2)
start_loop_number = 1;
max_loop_number = 12;
filename ='2_00';
filename_2 ='2_0';
pixels = 512;
pixel_conversion_factor = 0.892; %pixels/um for 2x zoom
threshold_multiplier = 0.05; %percentage of
depth=2;  %um
max_frames = 500;
%threshold_value = 400; relic implemented further down on 5/10/15
outlet_location = [300,285,74];  %(y,x,z) (down,right,into) (IN TERMS OF RED ONLY)
%inverted_outlet_location = [outlet_location(1),outlet_location(2),(max_frames-
outlet_location(3))];
edge_detector = 1;
```

```
ii=1;
jj=1;
kk=1;
ll=1;
mm=1;
nn=1;
oo=1;
pp=1;

%Preallocate Memory
%bothchannels = zeros(pixels,max_frames);
%F_saved = zeros(pixels,max_frames);
binary_output = zeros(pixels,pixels,max_frames);
particle_matrix = zeros(pixels,pixels,max_frames);
%Particles_saved = zeros(max_loop_number,max_frames);
particle_location = zeros(pixels,pixels,max_frames);
particle_distance = zeros(pixels,pixels,max_frames);
particle_velocity = zeros(pixels,pixels,max_frames);

%%%%%%%%%%%%%%%%%%%%%%%%%%%%%%%%%%%%%%%%%%%%%%%%%%%%%%%%%%%%%%%%%%%%%%%%%%%%%%%
loop_number=start_loop_number;

for loop_number = start_loop_number:max_loop_number


%%Read in the tif file to a 3d matrix
tic
loop_number
datestr(now)

string_loop=num2str(loop_number);
i=1;
if loop_number <=9
    file_to_use=strcat(filename,string_loop,'.tif');
else
    file_to_use=strcat(filename_2,string_loop,'.tif');
end

for i=1:max_frames

bothchannels(:,:,i) = imread(file_to_use,i);

%figure(1)
%imagesc(bothchannels(:,:,i));
%F_saved(loop_number,i) = getframe;



end

%%Get rid of background


size_image_stack = size(bothchannels);
num=size_image_stack(1)*size_image_stack(2);
image_vector=zeros(1,num);
stdev_multiplier = 0.1;

for mm = 1:max_frames
for jj=1:size_image_stack(1)
    for kk=1:size_image_stack(2)
        image_vector(1,(jj-1)*size_image_stack(2)+kk)=bothchannels(jj,kk,mm);
    end
end

image_vector = sort(image_vector);
length_of_image_vector = length(image_vector);
%top 10% average
top_10_percent_mean =
```

```
mean(image_vector(round(0.9*length_of_image_vector)):image_vector(length_of_image_vect
or));
%generate_threshold value as a percentage of top 10 percent
threshold_value = top_10_percent_mean*threshold_multiplier;

% average(mm) = mean(image_vector);
% stdev(mm) = std(image_vector);
  jj=1;
  kk=1;
end

for pp=1:max_frames;
    for oo=1:pixels;
        for nn=1:pixels;

        if bothchannels(nn,oo,pp) >= threshold_value
%stdev_multiplier*max(image_vector) %&& bothchannels(n,o,p) <=
mean(p)+stdev_multiplier*stdev(p)
           binary_output(nn,oo,pp) = 1;
        end
        end
    end
end



%%Spot the difference in the channels, assemble particle matrix, only
%%counts the pixels in the red channel by themselves, not those and the
%%ones from both channels

f=1; %row
g=1; %column
h=1; %page
h_new=(max_frames/2)-1;


for h=1:1:max_frames-1
    for g=1:pixels
        for f=1:pixels
            if binary_output(f,g,h)==1 && binary_output(f,g,h+1)==0;
                particle_matrix(f,g,h)=1;
%                 if h<=(max_frames/2)
%                 particle_distance(f,g,h)= sqrt((((f-
outlet_location(1))*(1/pixel_conversion_factor)).^2)+(((g-
outlet_location(2))*(1/pixel_conversion_factor)).^2)+((h*depth)-
outlet_location(3)).^2);
%                 particle_velocity(f,g,h)= particle_distance(f,g,h)./time;
%                 else
%                 h_new=(max_frames-h); %invert z direction
%                 particle_distance(f,g,h)= sqrt((((f-
outlet_location(1))*(1/pixel_conversion_factor)).^2)+(((g-
outlet_location(2))*(1/pixel_conversion_factor)).^2)+((h_new*depth)-
outlet_location(3)).^2);
%                 particle_velocity(f,g,h)= particle_distance(f,g,h)./time;
%                 end
            end
        end
    end



%figure(2)
%imagesc(particle_matrix(:,:,h));
%Particles_saved(loop_number,i) = getframe;
time = time + 0.317;
end
%%Calculate the Volume

m=1; %row
```

```
n=1; %column
o=1; %page

for o=1:max_frames-1
    total_area(o)=0;
    slice_volume(o)=0; %pix^2*um
    for n=1:pixels
        for m=1:pixels
            if particle_matrix(m,n,o)==1
                total_area(o) = total_area(o)+1;
            end
        end
    end
    slice_volume(o) = (depth*total_area(o))./(pixel_conversion_factor.^2); %total
surface area times depth of slice, now in um^3
    slice_volume_stored(loop_number,o) = slice_volume(o);
end




%%Store the volume values
total_volume_down(loop_number,1) = sum(slice_volume(1:max_frames/2));
total_volume_up(loop_number,1) = sum(slice_volume((max_frames/2):max_frames-1));


%Store Particle Locations/velocities in separate arrays
%assignin('base', ['particle_location' num2str(loop_number)], particle_matrix)
%assignin('base', ['particle_distance' num2str(loop_number)], particle_distance)
%assignin('base', ['particle_velocity' num2str(loop_number)], particle_velocity)
%Save the locations...
%save(strcat('particle_location',num2str(loop_number),'.mat'),['particle_location'
num2str(loop_number)])
%save(strcat('particle_distance',num2str(loop_number),'.mat'),['particle_distance'
num2str(loop_number)])
%save(strcat('particle_velocity',num2str(loop_number),'.mat'),['particle_velocity'
num2str(loop_number)])
%...and reduce them to single value
%assignin('base', ['particle_location' num2str(loop_number)], loop_number)
%assignin('base', ['particle_distance' num2str(loop_number)], loop_number)
%assignin('base', ['particle_velocity' num2str(loop_number)], loop_number)


%Calculate the surface area (without outermost pixels):

r=2; %row
s=2; %column
t=3; %page

for t=3:max_frames-2

    x_surface = zeros(pixels,pixels,max_frames);
    y_surface = zeros(pixels,pixels,max_frames);
    z_surface = zeros(pixels,pixels,max_frames);
    x_total(t) = 0;
    y_total(t) = 0;
    z_total(t) = 0;

    for s=2:pixels-1
        for r=2:pixels-1
            if particle_matrix(r,s,t)==1  && particle_matrix(r-1,s,t)==0 &&
particle_matrix(r+1,s,t)==0
                y_surface(r,s,t) = 2;
                y_total(t) = y_total(t)+2;
            elseif particle_matrix(r,s,t)==1  && particle_matrix(r-1,s,t)==0 &&
particle_matrix(r+1,s,t)==1
                y_surface(r,s,t) = 1;
                y_total(t) = y_total(t)+1;
            elseif particle_matrix(r,s,t)==1  && particle_matrix(r-1,s,t)==1 &&
```

```
particle_matrix(r+1,s,t)==0
                y_surface(r,s,t) = 1;
                y_total(t) = y_total(t)+1;
            end
            if particle_matrix(r,s,t)==1  && particle_matrix(r,s-1,t)==0 &&
particle_matrix(r,s+1,t)==0
                x_surface(r,s,t) = 2;
                x_total(t) = x_total(t)+2;
            elseif particle_matrix(r,s,t)==1  && particle_matrix(r,s-1,t)==0 &&
particle_matrix(r,s+1,t)==1
                x_surface(r,s,t) = 1;
                x_total(t) = x_total(t)+1;
            elseif particle_matrix(r,s,t)==1  && particle_matrix(r,s-1,t)==1 &&
particle_matrix(r,s+1,t)==0
                x_surface(r,s,t) = 1;
                x_total(t) = x_total(t)+1;
            end
            if particle_matrix(r,s,t)==1  && particle_matrix(r,s,t-2)==0 &&
particle_matrix(r,s,t+2)==0
                z_surface(r,s,t) = 2;
                z_total(t) = z_total(t)+2;
            elseif particle_matrix(r,s,t)==1  && particle_matrix(r,s,t-2)==0 &&
particle_matrix(r,s,t+2)==1
                z_surface(r,s,t) = 1;
                z_total(t) = z_total(t)+1;
            elseif particle_matrix(r,s,t)==1  && particle_matrix(r,s,t-2)==1 &&
particle_matrix(r,s,t+2)==0
                z_surface(r,s,t) = 1;
                z_total(t) = z_total(t)+1;
            end

        end
    end
       x_surface_area(t) = (depth*x_total(t))./(pixel_conversion_factor);
       y_surface_area(t) = (depth*y_total(t))./(pixel_conversion_factor);
       z_surface_area(t) = (z_total(t))./(pixel_conversion_factor.^2);
    slice_surface_area(t) = x_surface_area(t)+y_surface_area(t)+z_surface_area(t);
    slice_surface_area_stored(loop_number,t) = slice_surface_area(t);
end

%%Store the surface area values
total_surface_area_down(loop_number,1) = sum(slice_surface_area(1:max_frames/2));
total_surface_area_up(loop_number,1) =
sum(slice_surface_area((max_frames/2):max_frames-2));

%%%%%%%%%%%%%%%%%%%%%%%%%%%%%%%%%%%%%%%%%%%%%%%%%%%%%%%%%%%%%%%%%%%%%%%%%%%%%%%
%Ray tracing module v2
rr=1;
ss=1;
tt=1;
for tt=1:max_frames/2
    particle_matrix_new(:,:,tt) = particle_matrix(:,:,1+(2*tt-2));
end

matrix_dims = size(particle_matrix_new);

particle_matrix_down = particle_matrix_new(:,:,1:(matrix_dims(3)/2));
particle_matrix_up = particle_matrix(:,:,(matrix_dims(3)/2)+1:matrix_dims(3));

matrix_dims2 = size(particle_matrix_down);

%%%direction 1%%%%%
edge_detector=1;
ray_tracer=1;
direction=1;
if direction ==1;
    edge_detector=1;
    ray_tracer=1;
    while edge_detector==1
```

```
            if
particle_matrix_down(outlet_location(1),outlet_location(2)+ray_tracer,outlet_location(
3))==1;
                edge(direction,1+(6*loop_number)-6)=outlet_location(1);
                edge(direction,2+(6*loop_number)-6)=outlet_location(2)+ray_tracer;
                edge(direction,3+(6*loop_number)-6)=outlet_location(3)
                ray_tracer=ray_tracer+1;
                %picture limit detection
                if edge(direction,2+(6*loop_number)-6)== pixels
                    edge_detector=0;
                end
            else
                edge_detector=0;
            end
    end
    edge_detector=1;
    ray_tracer=1;
    while edge_detector==1
            if
particle_matrix_up(outlet_location(1),outlet_location(2)+ray_tracer,matrix_dims2(3)-
outlet_location(3)+1)==1;
                edge(direction,4+(6*loop_number)-6)=outlet_location(1);
                edge(direction,5+(6*loop_number)-6)=outlet_location(2)+ray_tracer;
                edge(direction,6+(6*loop_number)-6)=matrix_dims2(3)-
outlet_location(3)+1
                ray_tracer=ray_tracer+1;
                %picture limit detection
                if edge(direction,5+(6*loop_number)-6)== pixels
                    edge_detector=0;
                end
            else
                edge_detector=0;
            end
    end
end
%%%direction 2%%%%%
edge_detector=1;
ray_tracer=1;
direction=2;
if direction ==2;
    edge_detector=1;
    ray_tracer=1;
    while edge_detector==1
            if
particle_matrix_down(outlet_location(1)+ray_tracer,outlet_location(2)+ray_tracer,outle
t_location(3))==1;
                edge(direction,1+(6*loop_number)-6)=outlet_location(1)+ray_tracer;
                edge(direction,2+(6*loop_number)-6)=outlet_location(2)+ray_tracer;
                edge(direction,3+(6*loop_number)-6)=outlet_location(3)
                ray_tracer=ray_tracer+1;
                %picture limit detection
                if edge(direction,1+(6*loop_number)-6)== pixels ||
edge(direction,2+(6*loop_number)-6)==pixels
                    edge_detector=0;
                end
            else
                edge_detector=0;
            end
    end
    edge_detector=1;
    ray_tracer=1;
    while edge_detector==1
            if
particle_matrix_up(outlet_location(1)+ray_tracer,outlet_location(2)+ray_tracer,matrix_
dims2(3)-outlet_location(3)+1)==1;
                edge(direction,4+(6*loop_number)-6)=outlet_location(1)+ray_tracer;
                edge(direction,5+(6*loop_number)-6)=outlet_location(2)+ray_tracer;
                edge(direction,6+(6*loop_number)-6)=matrix_dims2(3)-
outlet_location(3)+1
```

```
                ray_tracer=ray_tracer+1;
                %picture limit detection
                if edge(direction,4+(6*loop_number)-6)== pixels ||
edge(direction,5+(6*loop_number)-6)==pixels
                    edge_detector=0;
                end
            else
                edge_detector=0;
            end
    end
end
%%%direction 3%%%%%
edge_detector=1;
ray_tracer=1;
direction=3;
if direction ==3;
    edge_detector=1;
    ray_tracer=1;
    while edge_detector==1
            if
particle_matrix_down(outlet_location(1)+ray_tracer,outlet_location(2),outlet_location(
3))==1;
                edge(direction,1+(6*loop_number)-6)=outlet_location(1)+ray_tracer;
                edge(direction,2+(6*loop_number)-6)=outlet_location(2);
                edge(direction,3+(6*loop_number)-6)=outlet_location(3)
                ray_tracer=ray_tracer+1;
                %picture limit detection
                if edge(direction,1+(6*loop_number)-6)== pixels
                    edge_detector=0;
                end
            else
                edge_detector=0;
            end
    end
    edge_detector=1;
    ray_tracer=1;
    while edge_detector==1
            if
particle_matrix_up(outlet_location(1)+ray_tracer,outlet_location(2),matrix_dims2(3)-
outlet_location(3)+1)==1;
                edge(direction,4+(6*loop_number)-6)=outlet_location(1)+ray_tracer;
                edge(direction,5+(6*loop_number)-6)=outlet_location(2);
                edge(direction,6+(6*loop_number)-6)=matrix_dims2(3)-
outlet_location(3)+1
                ray_tracer=ray_tracer+1;
                %picture limit detection
                if edge(direction,4+(6*loop_number)-6)==pixels
                    edge_detector=0;
                end
            else
                edge_detector=0;
            end
    end
end

%%%direction 4%%%%%
edge_detector=1;
ray_tracer=1;
direction=4;
if direction ==4;
    edge_detector=1;
    ray_tracer=1;
    while edge_detector==1
            if particle_matrix_down(outlet_location(1)+ray_tracer,outlet_location(2)-
ray_tracer,outlet_location(3))==1;
                edge(direction,1+(6*loop_number)-6)=outlet_location(1)+ray_tracer;
                edge(direction,2+(6*loop_number)-6)=outlet_location(2)-ray_tracer;
                edge(direction,3+(6*loop_number)-6)=outlet_location(3)
                ray_tracer=ray_tracer+1;
```

```
                %picture limit detection
                if edge(direction,1+(6*loop_number)-6)== pixels ||
edge(direction,2+(6*loop_number)-6)==1
                    edge_detector=0;
                end
            else
                edge_detector=0;
            end
    end
    edge_detector=1;
    ray_tracer=1;
    while edge_detector==1
            if particle_matrix_up(outlet_location(1)+ray_tracer,outlet_location(2)-
ray_tracer,matrix_dims2(3)-outlet_location(3)+1)==1;
                edge(direction,4+(6*loop_number)-6)=outlet_location(1)+ray_tracer;
                edge(direction,5+(6*loop_number)-6)=outlet_location(2)-ray_tracer;
                edge(direction,6+(6*loop_number)-6)=matrix_dims2(3)-
outlet_location(3)+1
                ray_tracer=ray_tracer+1;
                %picture limit detection
                if edge(direction,4+(6*loop_number)-6)== pixels ||
edge(direction,5+(6*loop_number)-6)==1
                    edge_detector=0;
                end
            else
                edge_detector=0;
            end
    end
end
%%%direction 5%%%%%
edge_detector=1;
ray_tracer=1;
direction=5;
if direction ==5;
    edge_detector=1;
    ray_tracer=1;
    while edge_detector==1
            if particle_matrix_down(outlet_location(1),outlet_location(2)-
ray_tracer,outlet_location(3))==1;
                edge(direction,1+(6*loop_number)-6)=outlet_location(1);
                edge(direction,2+(6*loop_number)-6)=outlet_location(2)-ray_tracer;
                edge(direction,3+(6*loop_number)-6)=outlet_location(3)
                ray_tracer=ray_tracer+1;
                %picture limit detection
                if edge(direction,2+(6*loop_number)-6)== 1
                    edge_detector=0;
                end
            else
                edge_detector=0;
            end
    end
    edge_detector=1;
    ray_tracer=1;
    while edge_detector==1
            if particle_matrix_up(outlet_location(1),outlet_location(2)-
ray_tracer,matrix_dims2(3)-outlet_location(3)+1)==1;
                edge(direction,4+(6*loop_number)-6)=outlet_location(1);
                edge(direction,5+(6*loop_number)-6)=outlet_location(2)-ray_tracer;
                edge(direction,6+(6*loop_number)-6)=matrix_dims2(3)-
outlet_location(3)+1
                ray_tracer=ray_tracer+1;
                %picture limit detection
                if edge(direction,5+(6*loop_number)-6)== 1
                    edge_detector=0;
                end
            else
                edge_detector=0;
            end
    end
```

```
end
%%%direction 6%%%%%
edge_detector=1;
ray_tracer=1;
direction=6;
if direction ==6;
    edge_detector=1;
    ray_tracer=1;
    while edge_detector==1
            if particle_matrix_down(outlet_location(1)-ray_tracer,outlet_location(2)-
ray_tracer,outlet_location(3))==1;
                edge(direction,1+(6*loop_number)-6)=outlet_location(1)-ray_tracer;
                edge(direction,2+(6*loop_number)-6)=outlet_location(2)-ray_tracer;
                edge(direction,3+(6*loop_number)-6)=outlet_location(3)
                ray_tracer=ray_tracer+1;
                %picture limit detection
                if edge(direction,1+(6*loop_number)-6)== 1 ||
edge(direction,2+(6*loop_number)-6)==1
                    edge_detector=0;
                end
            else
                edge_detector=0;
            end
    end
    edge_detector=1;
    ray_tracer=1;
    while edge_detector==1
            if particle_matrix_up(outlet_location(1)-ray_tracer,outlet_location(2)-
ray_tracer,matrix_dims2(3)-outlet_location(3)+1)==1;
                edge(direction,4+(6*loop_number)-6)=outlet_location(1)-ray_tracer;
                edge(direction,5+(6*loop_number)-6)=outlet_location(2)-ray_tracer;
                edge(direction,6+(6*loop_number)-6)=matrix_dims2(3)-
outlet_location(3)+1
                ray_tracer=ray_tracer+1;
                %picture limit detection
                if edge(direction,4+(6*loop_number)-6)== 1 ||
edge(direction,5+(6*loop_number)-6)==1
                    edge_detector=0;
                end
            else
                edge_detector=0;
            end
    end
end
%%%direction 7%%%%%
edge_detector=1;
ray_tracer=1;
direction=7;
if direction ==7;
    edge_detector=1;
    ray_tracer=1;
    while edge_detector==1
            if particle_matrix_down(outlet_location(1)-
ray_tracer,outlet_location(2),outlet_location(3))==1;
                edge(direction,1+(6*loop_number)-6)=outlet_location(1)-ray_tracer;
                edge(direction,2+(6*loop_number)-6)=outlet_location(2);
                edge(direction,3+(6*loop_number)-6)=outlet_location(3)
                ray_tracer=ray_tracer+1;
                %picture limit detection
                if edge(direction,1+(6*loop_number)-6)== 1
                    edge_detector=0;
                end
            else
                edge_detector=0;
            end
    end
    edge_detector=1;
    ray_tracer=1;
    while edge_detector==1
```

```
            if particle_matrix_up(outlet_location(1)-
ray_tracer,outlet_location(2),matrix_dims2(3)-outlet_location(3)+1)==1;
                edge(direction,4+(6*loop_number)-6)=outlet_location(1)-ray_tracer;
                edge(direction,5+(6*loop_number)-6)=outlet_location(2);
                edge(direction,6+(6*loop_number)-6)=matrix_dims2(3)-
outlet_location(3)+1
                ray_tracer=ray_tracer+1;
                %picture limit detection
                if edge(direction,4+(6*loop_number)-6)==1
                    edge_detector=0;
                end
            else
                edge_detector=0;
            end
    end
end
%%%direction 8%%%%%
edge_detector=1;
ray_tracer=1;
direction=8;
if direction ==8;
    edge_detector=1;
    ray_tracer=1;
    while edge_detector==1
            if particle_matrix_down(outlet_location(1)-
ray_tracer,outlet_location(2)+ray_tracer,outlet_location(3))==1;
                edge(direction,1+(6*loop_number)-6)=outlet_location(1)-ray_tracer;
                edge(direction,2+(6*loop_number)-6)=outlet_location(2)+ray_tracer;
                edge(direction,3+(6*loop_number)-6)=outlet_location(3)
                ray_tracer=ray_tracer+1;
                %picture limit detection
                if edge(direction,1+(6*loop_number)-6)== 1 ||
edge(direction,2+(6*loop_number)-6)==pixels
                    edge_detector=0;
                end
            else
                edge_detector=0;
            end
    end
    edge_detector=1;
    ray_tracer=1;
    while edge_detector==1
            if particle_matrix_up(outlet_location(1)-
ray_tracer,outlet_location(2)+ray_tracer,matrix_dims2(3)-outlet_location(3)+1)==1;
                edge(direction,4+(6*loop_number)-6)=outlet_location(1)-ray_tracer;
                edge(direction,5+(6*loop_number)-6)=outlet_location(2)+ray_tracer;
                edge(direction,6+(6*loop_number)-6)=matrix_dims2(3)-
outlet_location(3)+1
                ray_tracer=ray_tracer+1;
                %picture limit detection
                if edge(direction,4+(6*loop_number)-6)== 1 ||
edge(direction,5+(6*loop_number)-6)==pixels
                    edge_detector=0;
                end
            else
                edge_detector=0;
            end
    end
end

%%%%%%%%%%END OF PLANAR

%%%%%%%%%BEG OF BOT
%%%direction 9%%%%%
edge_detector=1;
ray_tracer=1;
direction=9;
if direction ==9;
    edge_detector=1;
```

```
    ray_tracer=1;
    while edge_detector==1
            if
particle_matrix_down(outlet_location(1),outlet_location(2)+ray_tracer,outlet_location(
3)+ray_tracer)==1;
                edge(direction,1+(6*loop_number)-6)=outlet_location(1);
                edge(direction,2+(6*loop_number)-6)=outlet_location(2)+ray_tracer;
                edge(direction,3+(6*loop_number)-6)=outlet_location(3)+ray_tracer
                ray_tracer=ray_tracer+1;
                %picture limit detection
                if edge(direction,2+(6*loop_number)-6)== pixels ||
edge(direction,3+(6*loop_number)-6)==matrix_dims2(3)
                    edge_detector=0;
                end
            else
                edge_detector=0;
            end
    end
    edge_detector=1;
    ray_tracer=1;
    while edge_detector==1
            if
particle_matrix_up(outlet_location(1),outlet_location(2)+ray_tracer,matrix_dims2(3)-
outlet_location(3)+1-ray_tracer)==1;
                edge(direction,4+(6*loop_number)-6)=outlet_location(1);
                edge(direction,5+(6*loop_number)-6)=outlet_location(2)+ray_tracer;
                edge(direction,6+(6*loop_number)-6)=matrix_dims2(3)-
outlet_location(3)+1-ray_tracer
                ray_tracer=ray_tracer+1;
                %picture limit detection
                if edge(direction,5+(6*loop_number)-6)== pixels ||
edge(direction,6+(6*loop_number)-6)==1
                    edge_detector=0;
                end
            else
                edge_detector=0;
            end
    end
end
%%%direction 10%%%%%
edge_detector=1;
ray_tracer=1;
direction=10;
if direction ==10;
    edge_detector=1;
    ray_tracer=1;
    while edge_detector==1
            if
particle_matrix_down(outlet_location(1)+ray_tracer,outlet_location(2)+ray_tracer,outle
t_location(3)+ray_tracer)==1;
                edge(direction,1+(6*loop_number)-6)=outlet_location(1)+ray_tracer;
                edge(direction,2+(6*loop_number)-6)=outlet_location(2)+ray_tracer;
                edge(direction,3+(6*loop_number)-6)=outlet_location(3)+ray_tracer
                ray_tracer=ray_tracer+1;
                %picture limit detection
                if edge(direction,1+(6*loop_number)-6)== pixels ||
edge(direction,2+(6*loop_number)-6)==pixels || edge(direction,3+(6*loop_number)-
6)==matrix_dims2(3)
                    edge_detector=0;
                end
            else
                edge_detector=0;
            end
    end
    edge_detector=1;
    ray_tracer=1;
    while edge_detector==1
            if
particle_matrix_up(outlet_location(1)+ray_tracer,outlet_location(2)+ray_tracer,matrix_
```

```
dims2(3)-outlet_location(3)+1-ray_tracer)==1;
                edge(direction,4+(6*loop_number)-6)=outlet_location(1)+ray_tracer;
                edge(direction,5+(6*loop_number)-6)=outlet_location(2)+ray_tracer;
                edge(direction,6+(6*loop_number)-6)=matrix_dims2(3)-
outlet_location(3)+1-ray_tracer
                ray_tracer=ray_tracer+1;
                %picture limit detection
                if edge(direction,4+(6*loop_number)-6)== pixels ||
edge(direction,5+(6*loop_number)-6)==pixels || edge(direction,6+(6*loop_number)-6)==1
                    edge_detector=0;
                end
            else
                edge_detector=0;
            end
    end
end
%%%direction 11%%%%%
edge_detector=1;
ray_tracer=1;
direction=11;
if direction ==11;
    edge_detector=1;
    ray_tracer=1;
    while edge_detector==1
            if
particle_matrix_down(outlet_location(1)+ray_tracer,outlet_location(2),outlet_location(
3)+ray_tracer)==1;
                edge(direction,1+(6*loop_number)-6)=outlet_location(1)+ray_tracer;
                edge(direction,2+(6*loop_number)-6)=outlet_location(2);
                edge(direction,3+(6*loop_number)-6)=outlet_location(3)+ray_tracer
                ray_tracer=ray_tracer+1;
                %picture limit detection
                if edge(direction,1+(6*loop_number)-6)== pixels ||
edge(direction,3+(6*loop_number)-6)==matrix_dims2(3)
                    edge_detector=0;
                end
            else
                edge_detector=0;
            end
    end
    edge_detector=1;
    ray_tracer=1;
    while edge_detector==1
            if
particle_matrix_up(outlet_location(1)+ray_tracer,outlet_location(2),matrix_dims2(3)-
outlet_location(3)+1-ray_tracer)==1;
                edge(direction,4+(6*loop_number)-6)=outlet_location(1)+ray_tracer;
                edge(direction,5+(6*loop_number)-6)=outlet_location(2);
                edge(direction,6+(6*loop_number)-6)=matrix_dims2(3)-
outlet_location(3)+1-ray_tracer
                ray_tracer=ray_tracer+1;
                %picture limit detection
                if edge(direction,4+(6*loop_number)-6)==pixels ||
edge(direction,6+(6*loop_number)-6)==1
                    edge_detector=0;
                end
            else
                edge_detector=0;
            end
    end
end

%%%direction 12%%%%%
edge_detector=1;
ray_tracer=1;
direction=12;
if direction ==12;
    edge_detector=1;
    ray_tracer=1;
```

```
    while edge_detector==1
            if particle_matrix_down(outlet_location(1)+ray_tracer,outlet_location(2)-
ray_tracer,outlet_location(3)+ray_tracer)==1;
                edge(direction,1+(6*loop_number)-6)=outlet_location(1)+ray_tracer;
                edge(direction,2+(6*loop_number)-6)=outlet_location(2)-ray_tracer;
                edge(direction,3+(6*loop_number)-6)=outlet_location(3)+ray_tracer
                ray_tracer=ray_tracer+1;
                %picture limit detection
                if edge(direction,1+(6*loop_number)-6)== pixels ||
edge(direction,2+(6*loop_number)-6)==1 || edge(direction,3+(6*loop_number)-
6)==matrix_dims2(3)
                    edge_detector=0;
                end
            else
                edge_detector=0;
            end
    end
    edge_detector=1;
    ray_tracer=1;
    while edge_detector==1
            if particle_matrix_up(outlet_location(1)+ray_tracer,outlet_location(2)-
ray_tracer,matrix_dims2(3)-outlet_location(3)+1-ray_tracer)==1;
                edge(direction,4+(6*loop_number)-6)=outlet_location(1)+ray_tracer;
                edge(direction,5+(6*loop_number)-6)=outlet_location(2)-ray_tracer;
                edge(direction,6+(6*loop_number)-6)=matrix_dims2(3)-
outlet_location(3)+1-ray_tracer
                ray_tracer=ray_tracer+1;
                %picture limit detection
                if edge(direction,4+(6*loop_number)-6)== pixels ||
edge(direction,5+(6*loop_number)-6)==1 || edge(direction,6+(6*loop_number)-6)==1
                    edge_detector=0;
                end
            else
                edge_detector=0;
            end
    end
end
%%%direction 13%%%%%
edge_detector=1;
ray_tracer=1;
direction=13;
if direction ==13;
    edge_detector=1;
    ray_tracer=1;
    while edge_detector==1
            if particle_matrix_down(outlet_location(1),outlet_location(2)-
ray_tracer,outlet_location(3)+ray_tracer)==1;
                edge(direction,1+(6*loop_number)-6)=outlet_location(1);
                edge(direction,2+(6*loop_number)-6)=outlet_location(2)-ray_tracer;
                edge(direction,3+(6*loop_number)-6)=outlet_location(3)+ray_tracer
                ray_tracer=ray_tracer+1;
                %picture limit detection
                if edge(direction,2+(6*loop_number)-6)== 1 ||
edge(direction,3+(6*loop_number)-6)==matrix_dims2(3)
                    edge_detector=0;
                end
            else
                edge_detector=0;
            end
    end
    edge_detector=1;
    ray_tracer=1;
    while edge_detector==1
            if particle_matrix_up(outlet_location(1),outlet_location(2)-
ray_tracer,matrix_dims2(3)-outlet_location(3)+1-ray_tracer)==1;
                edge(direction,4+(6*loop_number)-6)=outlet_location(1);
                edge(direction,5+(6*loop_number)-6)=outlet_location(2)-ray_tracer;
                edge(direction,6+(6*loop_number)-6)=matrix_dims2(3)-
outlet_location(3)+1-ray_tracer
```

```
                ray_tracer=ray_tracer+1;
                %picture limit detection
                if edge(direction,5+(6*loop_number)-6)== 1 ||
edge(direction,6+(6*loop_number)-6)==1
                    edge_detector=0;
                end
            else
                edge_detector=0;
            end
    end
end
%%%direction 14%%%%%
edge_detector=1;
ray_tracer=1;
direction=14;
if direction ==14;
    edge_detector=1;
    ray_tracer=1;
    while edge_detector==1
            if particle_matrix_down(outlet_location(1)-ray_tracer,outlet_location(2)-
ray_tracer,outlet_location(3)+ray_tracer)==1;
                edge(direction,1+(6*loop_number)-6)=outlet_location(1)-ray_tracer;
                edge(direction,2+(6*loop_number)-6)=outlet_location(2)-ray_tracer;
                edge(direction,3+(6*loop_number)-6)=outlet_location(3)+ray_tracer
                ray_tracer=ray_tracer+1;
                %picture limit detection
                if edge(direction,1+(6*loop_number)-6)== 1 ||
edge(direction,2+(6*loop_number)-6)==1 || edge(direction,3+(6*loop_number)-
6)==matrix_dims2(3)
                    edge_detector=0;
                end
            else
                edge_detector=0;
            end
    end
    edge_detector=1;
    ray_tracer=1;
    while edge_detector==1
            if particle_matrix_up(outlet_location(1)-ray_tracer,outlet_location(2)-
ray_tracer,matrix_dims2(3)-outlet_location(3)+1-ray_tracer)==1;
                edge(direction,4+(6*loop_number)-6)=outlet_location(1)-ray_tracer;
                edge(direction,5+(6*loop_number)-6)=outlet_location(2)-ray_tracer;
                edge(direction,6+(6*loop_number)-6)=matrix_dims2(3)-
outlet_location(3)+1-ray_tracer
                ray_tracer=ray_tracer+1;
                %picture limit detection
                if edge(direction,4+(6*loop_number)-6)== 1 ||
edge(direction,5+(6*loop_number)-6)==1 || edge(direction,6+(6*loop_number)-6)==1
                    edge_detector=0;
                end
            else
                edge_detector=0;
            end
    end
end
%%%direction 15%%%%%
edge_detector=1;
ray_tracer=1;
direction=15;
if direction ==15;
    edge_detector=1;
    ray_tracer=1;
    while edge_detector==1
            if particle_matrix_down(outlet_location(1)-
ray_tracer,outlet_location(2),outlet_location(3)+ray_tracer)==1;
                edge(direction,1+(6*loop_number)-6)=outlet_location(1)-ray_tracer;
                edge(direction,2+(6*loop_number)-6)=outlet_location(2);
                edge(direction,3+(6*loop_number)-6)=outlet_location(3)+ray_tracer
                ray_tracer=ray_tracer+1;
```

```
                %picture limit detection
                if edge(direction,1+(6*loop_number)-6)== 1 ||
edge(direction,3+(6*loop_number)-6)==matrix_dims2(3)
                    edge_detector=0;
                end
            else
                edge_detector=0;
            end
    end
    edge_detector=1;
    ray_tracer=1;
    while edge_detector==1
            if particle_matrix_up(outlet_location(1)-
ray_tracer,outlet_location(2),matrix_dims2(3)-outlet_location(3)+1-ray_tracer)==1;
                edge(direction,4+(6*loop_number)-6)=outlet_location(1)-ray_tracer;
                edge(direction,5+(6*loop_number)-6)=outlet_location(2);
                edge(direction,6+(6*loop_number)-6)=matrix_dims2(3)-
outlet_location(3)+1-ray_tracer
                ray_tracer=ray_tracer+1;
                %picture limit detection
                if edge(direction,4+(6*loop_number)-6)==1 ||
edge(direction,6+(6*loop_number)-6)==1
                    edge_detector=0;
                end
            else
                edge_detector=0;
            end
    end
end
%%%direction 16%%%%%
edge_detector=1;
ray_tracer=1;
direction=16;
if direction ==16;
    edge_detector=1;
    ray_tracer=1;
    while edge_detector==1
            if particle_matrix_down(outlet_location(1)-
ray_tracer,outlet_location(2)+ray_tracer,outlet_location(3)+ray_tracer)==1;
                edge(direction,1+(6*loop_number)-6)=outlet_location(1)-ray_tracer;
                edge(direction,2+(6*loop_number)-6)=outlet_location(2)+ray_tracer;
                edge(direction,3+(6*loop_number)-6)=outlet_location(3)+ray_tracer
                ray_tracer=ray_tracer+1;
                %picture limit detection
                if edge(direction,1+(6*loop_number)-6)== 1 ||
edge(direction,2+(6*loop_number)-6)==pixels || edge(direction,3+(6*loop_number)-
6)==matrix_dims2(3)
                    edge_detector=0;
                end
            else
                edge_detector=0;
            end
    end
    edge_detector=1;
    ray_tracer=1;
    while edge_detector==1
            if particle_matrix_up(outlet_location(1)-
ray_tracer,outlet_location(2)+ray_tracer,matrix_dims2(3)-outlet_location(3)+1-
ray_tracer)==1;
                edge(direction,4+(6*loop_number)-6)=outlet_location(1)-ray_tracer;
                edge(direction,5+(6*loop_number)-6)=outlet_location(2)+ray_tracer;
                edge(direction,6+(6*loop_number)-6)=matrix_dims2(3)-
outlet_location(3)+1-ray_tracer
                ray_tracer=ray_tracer+1;
                %picture limit detection
                if edge(direction,4+(6*loop_number)-6)== 1 ||
edge(direction,5+(6*loop_number)-6)==pixels || edge(direction,6+(6*loop_number)-6)==1
                    edge_detector=0;
                end
```

```
            else
                edge_detector=0;
            end
    end
end
%%%direction 17%%%%%
edge_detector=1;
ray_tracer=1;
direction=17;
if direction ==17;
    edge_detector=1;
    ray_tracer=1;
    while edge_detector==1
            if
particle_matrix_down(outlet_location(1),outlet_location(2),outlet_location(3)+ray_trac
er)==1;
                edge(direction,1+(6*loop_number)-6)=outlet_location(1);
                edge(direction,2+(6*loop_number)-6)=outlet_location(2);
                edge(direction,3+(6*loop_number)-6)=outlet_location(3)+ray_tracer
                ray_tracer=ray_tracer+1;
                %picture limit detection
                if edge(direction,3+(6*loop_number)-6)==matrix_dims2(3)
                    edge_detector=0;
                end
            else
                edge_detector=0;
            end
    end
    edge_detector=1;
    ray_tracer=1;
    while edge_detector==1
            if
particle_matrix_up(outlet_location(1),outlet_location(2),matrix_dims2(3)-
outlet_location(3)+1-ray_tracer)==1;
                edge(direction,4+(6*loop_number)-6)=outlet_location(1);
                edge(direction,5+(6*loop_number)-6)=outlet_location(2);
                edge(direction,6+(6*loop_number)-6)=matrix_dims2(3)-
outlet_location(3)+1-ray_tracer
                ray_tracer=ray_tracer+1;
                %picture limit detection
                if edge(direction,6+(6*loop_number)-6)==1
                    edge_detector=0;
                end
            else
                edge_detector=0;
            end
    end
end

%%%%%%%%%END OF BOT

%%%%%%%%BEG OF TOP
%%%direction 18%%%%%
edge_detector=1;
ray_tracer=1;
direction=18;
if direction ==18;
    edge_detector=1;
    ray_tracer=1;
    while edge_detector==1
            if
particle_matrix_down(outlet_location(1),outlet_location(2)+ray_tracer,outlet_location(
3)-ray_tracer)==1;
                edge(direction,1+(6*loop_number)-6)=outlet_location(1);
                edge(direction,2+(6*loop_number)-6)=outlet_location(2)+ray_tracer;
                edge(direction,3+(6*loop_number)-6)=outlet_location(3)-ray_tracer
                ray_tracer=ray_tracer+1;
                %picture limit detection
                if edge(direction,2+(6*loop_number)-6)== pixels ||
```

```
edge(direction,3+(6*loop_number)-6)==1
                    edge_detector=0;
                end
            else
                edge_detector=0;
            end
    end
    edge_detector=1;
    ray_tracer=1;
    while edge_detector==1
            if
particle_matrix_up(outlet_location(1),outlet_location(2)+ray_tracer,matrix_dims2(3)-
outlet_location(3)+1+ray_tracer)==1;
                edge(direction,4+(6*loop_number)-6)=outlet_location(1);
                edge(direction,5+(6*loop_number)-6)=outlet_location(2)+ray_tracer;
                edge(direction,6+(6*loop_number)-6)=matrix_dims2(3)-
outlet_location(3)+1+ray_tracer
                ray_tracer=ray_tracer+1;
                %picture limit detection
                if edge(direction,5+(6*loop_number)-6)== pixels ||
edge(direction,6+(6*loop_number)-6)==matrix_dims2(3)
                    edge_detector=0;
                end
            else
                edge_detector=0;
            end
    end
end
%%%direction 19%%%%%
edge_detector=1;
ray_tracer=1;
direction=19;
if direction ==19;
    edge_detector=1;
    ray_tracer=1;
    while edge_detector==1
            if
particle_matrix_down(outlet_location(1)+ray_tracer,outlet_location(2)+ray_tracer,outle
t_location(3)-ray_tracer)==1;
                edge(direction,1+(6*loop_number)-6)=outlet_location(1)+ray_tracer;
                edge(direction,2+(6*loop_number)-6)=outlet_location(2)+ray_tracer;
                edge(direction,3+(6*loop_number)-6)=outlet_location(3)-ray_tracer
                ray_tracer=ray_tracer+1;
                %picture limit detection
                if edge(direction,1+(6*loop_number)-6)== pixels ||
edge(direction,2+(6*loop_number)-6)==pixels || edge(direction,3+(6*loop_number)-6)==1
                    edge_detector=0;
                end
            else
                edge_detector=0;
            end
    end
    edge_detector=1;
    ray_tracer=1;
    while edge_detector==1
            if
particle_matrix_up(outlet_location(1)+ray_tracer,outlet_location(2)+ray_tracer,matrix_
dims2(3)-outlet_location(3)+1+ray_tracer)==1;
                edge(direction,4+(6*loop_number)-6)=outlet_location(1)+ray_tracer;
                edge(direction,5+(6*loop_number)-6)=outlet_location(2)+ray_tracer;
                edge(direction,6+(6*loop_number)-6)=matrix_dims2(3)-
outlet_location(3)+1+ray_tracer
                ray_tracer=ray_tracer+1;
                %picture limit detection
                if edge(direction,4+(6*loop_number)-6)== pixels ||
edge(direction,5+(6*loop_number)-6)==pixels || edge(direction,6+(6*loop_number)-
6)==matrix_dims2(3)
                    edge_detector=0;
                end
```

```
            else
                edge_detector=0;
            end
    end
end
%%%direction 20%%%%%
edge_detector=1;
ray_tracer=1;
direction=20;
if direction ==20;
    edge_detector=1;
    ray_tracer=1;
    while edge_detector==1
            if
particle_matrix_down(outlet_location(1)+ray_tracer,outlet_location(2),outlet_location(
3)-ray_tracer)==1;
                edge(direction,1+(6*loop_number)-6)=outlet_location(1)+ray_tracer;
                edge(direction,2+(6*loop_number)-6)=outlet_location(2);
                edge(direction,3+(6*loop_number)-6)=outlet_location(3)-ray_tracer
                ray_tracer=ray_tracer+1;
                %picture limit detection
                if edge(direction,1+(6*loop_number)-6)== pixels ||
edge(direction,3+(6*loop_number)-6)==1
                    edge_detector=0;
                end
            else
                edge_detector=0;
            end
    end
    edge_detector=1;
    ray_tracer=1;
    while edge_detector==1
            if
particle_matrix_up(outlet_location(1)+ray_tracer,outlet_location(2),matrix_dims2(3)-
outlet_location(3)+1+ray_tracer)==1;
                edge(direction,4+(6*loop_number)-6)=outlet_location(1)+ray_tracer;
                edge(direction,5+(6*loop_number)-6)=outlet_location(2);
                edge(direction,6+(6*loop_number)-6)=matrix_dims2(3)-
outlet_location(3)+1+ray_tracer
                ray_tracer=ray_tracer+1;
                %picture limit detection
                if edge(direction,4+(6*loop_number)-6)==pixels ||
edge(direction,6+(6*loop_number)-6)==matrix_dims2(3)
                    edge_detector=0;
                end
            else
                edge_detector=0;
            end
    end
end

%%%direction 21%%%%%
edge_detector=1;
ray_tracer=1;
direction=21;
if direction ==21;
    edge_detector=1;
    ray_tracer=1;
    while edge_detector==1
            if particle_matrix_down(outlet_location(1)+ray_tracer,outlet_location(2)-
ray_tracer,outlet_location(3)-ray_tracer)==1;
                edge(direction,1+(6*loop_number)-6)=outlet_location(1)+ray_tracer;
                edge(direction,2+(6*loop_number)-6)=outlet_location(2)-ray_tracer;
                edge(direction,3+(6*loop_number)-6)=outlet_location(3)-ray_tracer
                ray_tracer=ray_tracer+1;
                %picture limit detection
                if edge(direction,1+(6*loop_number)-6)== pixels ||
edge(direction,2+(6*loop_number)-6)==1 || edge(direction,3+(6*loop_number)-6)==1
                    edge_detector=0;
```

```
                end
            else
                edge_detector=0;
            end
    end
    edge_detector=1;
    ray_tracer=1;
    while edge_detector==1
            if particle_matrix_up(outlet_location(1)+ray_tracer,outlet_location(2)-
ray_tracer,matrix_dims2(3)-outlet_location(3)+1+ray_tracer)==1;
                edge(direction,4+(6*loop_number)-6)=outlet_location(1)+ray_tracer;
                edge(direction,5+(6*loop_number)-6)=outlet_location(2)-ray_tracer;
                edge(direction,6+(6*loop_number)-6)=matrix_dims2(3)-
outlet_location(3)+1+ray_tracer
                ray_tracer=ray_tracer+1;
                %picture limit detection
                if edge(direction,4+(6*loop_number)-6)== pixels ||
edge(direction,5+(6*loop_number)-6)==1 || edge(direction,6+(6*loop_number)-
6)==matrix_dims2(3)
                    edge_detector=0;
                end
            else
                edge_detector=0;
            end
    end
end
%%%direction 22%%%%%
edge_detector=1;
ray_tracer=1;
direction=22;
if direction ==22;
    edge_detector=1;
    ray_tracer=1;
    while edge_detector==1
            if particle_matrix_down(outlet_location(1),outlet_location(2)-
ray_tracer,outlet_location(3)-ray_tracer)==1;
                edge(direction,1+(6*loop_number)-6)=outlet_location(1);
                edge(direction,2+(6*loop_number)-6)=outlet_location(2)-ray_tracer;
                edge(direction,3+(6*loop_number)-6)=outlet_location(3)-ray_tracer
                ray_tracer=ray_tracer+1;
                %picture limit detection
                if edge(direction,2+(6*loop_number)-6)== 1 ||
edge(direction,3+(6*loop_number)-6)==1
                    edge_detector=0;
                end
            else
                edge_detector=0;
            end
    end
    edge_detector=1;
    ray_tracer=1;
    while edge_detector==1
            if particle_matrix_up(outlet_location(1),outlet_location(2)-
ray_tracer,matrix_dims2(3)-outlet_location(3)+1+ray_tracer)==1;
                edge(direction,4+(6*loop_number)-6)=outlet_location(1);
                edge(direction,5+(6*loop_number)-6)=outlet_location(2)-ray_tracer;
                edge(direction,6+(6*loop_number)-6)=matrix_dims2(3)-
outlet_location(3)+1+ray_tracer
                ray_tracer=ray_tracer+1;
                %picture limit detection
                if edge(direction,5+(6*loop_number)-6)== 1 ||
edge(direction,6+(6*loop_number)-6)==matrix_dims2(3)
                    edge_detector=0;
                end
            else
                edge_detector=0;
            end
    end
end
```

```
%%%direction 23%%%%%
edge_detector=1;
ray_tracer=1;
direction=23;
if direction ==23;
    edge_detector=1;
    ray_tracer=1;
    while edge_detector==1
            if particle_matrix_down(outlet_location(1)-ray_tracer,outlet_location(2)-
ray_tracer,outlet_location(3)-ray_tracer)==1;
                edge(direction,1+(6*loop_number)-6)=outlet_location(1)-ray_tracer;
                edge(direction,2+(6*loop_number)-6)=outlet_location(2)-ray_tracer;
                edge(direction,3+(6*loop_number)-6)=outlet_location(3)-ray_tracer
                ray_tracer=ray_tracer+1;
                %picture limit detection
                if edge(direction,1+(6*loop_number)-6)== 1 ||
edge(direction,2+(6*loop_number)-6)==1 || edge(direction,3+(6*loop_number)-6)==1
                    edge_detector=0;
                end
            else
                edge_detector=0;
            end
    end
    edge_detector=1;
    ray_tracer=1;
    while edge_detector==1
            if particle_matrix_up(outlet_location(1)-ray_tracer,outlet_location(2)-
ray_tracer,matrix_dims2(3)-outlet_location(3)+1+ray_tracer)==1;
                edge(direction,4+(6*loop_number)-6)=outlet_location(1)-ray_tracer;
                edge(direction,5+(6*loop_number)-6)=outlet_location(2)-ray_tracer;
                edge(direction,6+(6*loop_number)-6)=matrix_dims2(3)-
outlet_location(3)+1+ray_tracer
                ray_tracer=ray_tracer+1;
                %picture limit detection
                if edge(direction,4+(6*loop_number)-6)== 1 ||
edge(direction,5+(6*loop_number)-6)==1 || edge(direction,6+(6*loop_number)-
6)==matrix_dims2(3)
                    edge_detector=0;
                end
            else
                edge_detector=0;
            end
    end
end
%%%direction 24%%%%%
edge_detector=1;
ray_tracer=1;
direction=24;
if direction ==24;
    edge_detector=1;
    ray_tracer=1;
    while edge_detector==1
            if particle_matrix_down(outlet_location(1)-
ray_tracer,outlet_location(2),outlet_location(3)-ray_tracer)==1;
                edge(direction,1+(6*loop_number)-6)=outlet_location(1)-ray_tracer;
                edge(direction,2+(6*loop_number)-6)=outlet_location(2);
                edge(direction,3+(6*loop_number)-6)=outlet_location(3)-ray_tracer
                ray_tracer=ray_tracer+1;
                %picture limit detection
                if edge(direction,1+(6*loop_number)-6)== 1 ||
edge(direction,3+(6*loop_number)-6)==1
                    edge_detector=0;
                end
            else
                edge_detector=0;
            end
    end
    edge_detector=1;
    ray_tracer=1;
```

```
    while edge_detector==1
            if particle_matrix_up(outlet_location(1)-
ray_tracer,outlet_location(2),matrix_dims2(3)-outlet_location(3)+1+ray_tracer)==1;
                edge(direction,4+(6*loop_number)-6)=outlet_location(1)-ray_tracer;
                edge(direction,5+(6*loop_number)-6)=outlet_location(2);
                edge(direction,6+(6*loop_number)-6)=matrix_dims2(3)-
outlet_location(3)+1+ray_tracer
                ray_tracer=ray_tracer+1;
                %picture limit detection
                if edge(direction,4+(6*loop_number)-6)==1 ||
edge(direction,6+(6*loop_number)-6)==matrix_dims2(3)
                    edge_detector=0;
                end
            else
                edge_detector=0;
            end
    end
end
%%%direction 25%%%%%
edge_detector=1;
ray_tracer=1;
direction=25;
if direction ==25;
    edge_detector=1;
    ray_tracer=1;
    while edge_detector==1
            if particle_matrix_down(outlet_location(1)-
ray_tracer,outlet_location(2)+ray_tracer,outlet_location(3)-ray_tracer)==1;
                edge(direction,1+(6*loop_number)-6)=outlet_location(1)-ray_tracer;
                edge(direction,2+(6*loop_number)-6)=outlet_location(2)+ray_tracer;
                edge(direction,3+(6*loop_number)-6)=outlet_location(3)-ray_tracer
                ray_tracer=ray_tracer+1;
                %picture limit detection
                if edge(direction,1+(6*loop_number)-6)== 1 ||
edge(direction,2+(6*loop_number)-6)==pixels || edge(direction,3+(6*loop_number)-6)==1
                    edge_detector=0;
                end
            else
                edge_detector=0;
            end
    end
    edge_detector=1;
    ray_tracer=1;
    while edge_detector==1
            if particle_matrix_up(outlet_location(1)-
ray_tracer,outlet_location(2)+ray_tracer,matrix_dims2(3)-
outlet_location(3)+1+ray_tracer)==1;
                edge(direction,4+(6*loop_number)-6)=outlet_location(1)-ray_tracer;
                edge(direction,5+(6*loop_number)-6)=outlet_location(2)+ray_tracer;
                edge(direction,6+(6*loop_number)-6)=matrix_dims2(3)-
outlet_location(3)+1+ray_tracer
                ray_tracer=ray_tracer+1;
                %picture limit detection
                if edge(direction,4+(6*loop_number)-6)== 1 ||
edge(direction,5+(6*loop_number)-6)==pixels || edge(direction,6+(6*loop_number)-
6)==matrix_dims2(3)
                    edge_detector=0;
                end
            else
                edge_detector=0;
            end
    end
end
%%%direction 26%%%%%
edge_detector=1;
ray_tracer=1;
direction=26;
if direction ==26;
    edge_detector=1;
```

```
    ray_tracer=1;
    while edge_detector==1
            if
particle_matrix_down(outlet_location(1),outlet_location(2),outlet_location(3)-
ray_tracer)==1;
                edge(direction,1+(6*loop_number)-6)=outlet_location(1);
                edge(direction,2+(6*loop_number)-6)=outlet_location(2);
                edge(direction,3+(6*loop_number)-6)=outlet_location(3)-ray_tracer
                ray_tracer=ray_tracer+1;
                %picture limit detection
                if edge(direction,3+(6*loop_number)-6)==1
                    edge_detector=0;
                end
            else
                edge_detector=0;
            end
    end
    edge_detector=1;
    ray_tracer=1;
    while edge_detector==1
            if
particle_matrix_up(outlet_location(1),outlet_location(2),matrix_dims2(3)-
outlet_location(3)+1+ray_tracer)==1;
                edge(direction,4+(6*loop_number)-6)=outlet_location(1);
                edge(direction,5+(6*loop_number)-6)=outlet_location(2);
                edge(direction,6+(6*loop_number)-6)=matrix_dims2(3)-
outlet_location(3)+1+ray_tracer
                ray_tracer=ray_tracer+1;
                %picture limit detection
                if edge(direction,6+(6*loop_number)-6)==matrix_dims2(3)
                    edge_detector=0;
                end
            else
                edge_detector=0;
            end
    end
end



%%%%%%%%%%%%%%%%%%%%%%%%%%%%%%%%%%%%%%%%%%%%%%%%%%%%%%%%%%%%%%%%%%%%%%%%%%%%%%%
toc
time = time + 2.635;
end


%%%%%%%%%%%%%%%%%%%%%%%%%%%%%%%%%%%%%%%%%%%%%%%%%%%%%%%%%%%%%%%%%%%%%%%%%%%%%%%


%%%%%%%%%%%%%%%%%%%%%%%%%%%%%%%%%%%%%%%%%%%%%%%%%%%%%%%%%%%%%%%%%%%%%%%%%%%%%%%

%Appendix

%%Plot the Volume of distribution
% figure(3)
% plot(0.5:max_loop_number-
0.5,total_volume_down,'bx',1:max_loop_number,total_volume_up,'rx')

%%Save Variable Information
save('variables.mat')


%%%%%%%For showing heatmap
% for z=1:2:499
%     figure(1)
%     hold on
%     imagesc(particle_distance10(:,:,z))
%     colorbar
%     hold off
```

```
% end
```

REFERENCES

[1] J. Xu, S.L. Murphy, K.D. Kochanek, B.A. Bastian, National Vital Statistics Reports Deaths : Final Data for 2009, Natl. Cent. Heal. Stat. 60 (2012) 1–117. http://www.cdc.gov/nchs/data/nvsr/nvsr58/nvsr58_19.pdf.

[2] American Cancer Society, Cancer Facts & Figures 2015, Cancer Facts Fig. 2015. (2015) 1–9. doi:10.1097/01.NNR.0000289503.22414.79.

[3] W.M. Pardridge, Drug and gene delivery to the brain: The vascular route, Neuron. 36 (2002) 555–558. doi:10.1016/S0896-6273(02)01054-1.

[4] J. Bicker, G. Alves, A. Fortuna, A. Falcão, Blood-brain barrier models and their relevance for a successful development of CNS drug delivery systems: A review, Eur. J. Pharm. Biopharm. 87 (2014) 409–432. doi:10.1016/j.ejpb.2014.03.012.

[5] C.T. Lu, Y.Z. Zhao, H.L. Wong, J. Cai, L. Peng, X.Q. Tian, Current approaches to enhance CNS delivery of drugs across the brain barriers, Int. J. Nanomedicine. 9 (2014) 2241–2257. doi:10.2147/IJN.S61288.

[6] L. Crawford, J. Rosch, D. Putnam, Concepts, technologies, and practices for drug delivery past the blood-brain barrier to the central nervous system, J. Control. Release. (2015). doi:10.1016/j.jconrel.2015.12.041.

[7] M.S. Lesniak, R. Langer, H. Brem, Drug delivery to tumors of the central nervous system., Curr. Neurol. Neurosci. Rep. 1 (2001) 210–6. doi:10.1007/s11910-001-0020-z.

[8] A. Mangraviti, B. Tyler, H. Brem, Interstitial chemotherapy for malignant glioma: Future prospects in the era of multimodal therapy, Surg. Neurol. …. 2 (2011) 1–22. doi:10.4103/2152.

[9] X. Yang, R. Saito, T. Nakamura, R. Zhang, Y. Sonoda, T. Kumabe, J. Forsayeth, K. Bankiewicz, T. Tominaga, Peri-tumoral leakage during intra-tumoral convection-enhanced delivery has implications for efficacy of peri-tumoral infusion before removal of tumor., Drug Deliv. 7544 (2014) 1–6. doi:10.3109/10717544.2014.914987.

[10] Westphal M, Hilt DC, Bortey E, Delavault P, Olivares R, Warnke PC, A phase 3 trial of local che- motherapy with biodegradable carmustine (BCNU) wafers (Gliadel wafers) in patients with primary malignant glioma, Neuro Oncol. (2003).

[11] M. Westphal, Z. Ram, V. Riddle, D. Hilt, E. Bortey, Gliadel(R) wafer in initial surgery for malignant glioma: Long-term follow-up of a multicenter controlled trial, Acta Neurochir. (Wien). 148 (2006) 269–275. doi:10.1007/s00701-005-0707-z.

[12] R.H. Bobo, D.W. Laske, a Akbasak, P.F. Morrison, R.L. Dedrick, E.H. Oldfield, Convection-enhanced delivery of macromolecules in the brain., Proc. Natl. Acad. Sci. U. S. A. 91 (1994) 2076–80. http://www.pubmedcentral.nih.gov/articlerender.fcgi?artid=43312&tool=pmcentrez&rendertype=abstract.

[13] J.F. Hamilton, P.F. Morrison, M.Y. Chen, J. Harvey-White, R.S. Pernaute, H. Phillips, E. Oldfield, K.S. Bankiewicz, Heparin coinfusion during convection-enhanced delivery (CED) increases the distribution of the glial-derived neurotrophic factor (GDNF) ligand family in rat striatum and enhances the pharmacological activity of neurturin., Exp. Neurol. 168 (2001) 155–61. doi:10.1006/exnr.2000.7571.

[14] S. Vinchon-Petit, D. Jarnet, A. Paillard, J.-P. Benoit, E. Garcion, P. Menei, In vivo evaluation of intracellular drug-nanocarriers infused into intracranial tumours by convection-enhanced delivery: distribution and radiosensitisation efficacy., J. Neurooncol. (2010). doi:10.1007/s11060-009-0012-4.

[15] D.K. Stiles, Z. Zhang, P. Ge, B. Nelson, R. Grondin, Y. Ai, P. Hardy, P.T. Nelson, A.P. Guzaev, M.T. Butt, K. Charisse, V. Kosovrasti, L. Tchangov, M. Meys, M. Maier, L. Nechev, M. Manoharan, W.F. Kaemmerer, D. Gwost, G.R. Stewart, D.M. Gash, D.W.Y. Sah, Widespread suppression of huntingtin with convection-enhanced delivery of siRNA., Exp. Neurol. 233 (2012) 463–71. doi:10.1016/j.expneurol.2011.11.020.

[16] M.F. Lam, M.G. Thomas, C.R.P. Lind, Neurosurgical convection-enhanced

delivery of treatments for Parkinson's disease., J. Clin. Neurosci. 18 (2011) 1163–7. doi:10.1016/j.jocn.2011.01.012.

[17] R. Hiramatsu, S. Kawabata, H. Tanaka, Y. Sakurai, M. Suzuki, K. Ono, S.-I. Miyatake, T. Kuroiwa, E. Hao, M.G.H. Vicente, Tetrakis(p -Carboranylthio-Tetrafluorophenyl)Chlorin (TPFC): Application for Photodynamic Therapy and Boron Neutron Capture Therapy, J. Pharm. Sci. 104 (2015) 962–970. doi:10.1002/jps.24317.

[18] M. Yokosawa, Y. Sonoda, S. Sugiyama, R. Saito, Y. Yamashita, M. Nishihara, T. Satoh, T. Kumabe, M. Yokoyama, T. Tominaga, Convection-enhanced delivery of a synthetic retinoid Am80, loaded into polymeric micelles, prolongs the survival of rats bearing intracranial glioblastoma xenografts., Tohoku J. Exp. Med. 221 (2010) 257–264. doi:10.1620/tjem.221.257.

[19] E. Allard, D. Jarnet, A. Vessières, S. Vinchon-Petit, G. Jaouen, J.P. Benoit, C. Passirani, Local delivery of ferrociphenol lipid nanocapsules followed by external radiotherapy as a synergistic treatment against intracranial 9L glioma xenograft, Pharm. Res. 27 (2010) 56–64. doi:10.1007/s11095-009-0006-0.

[20] D. Yin, Y. Zhai, H.E. Gruber, C.E. Ibanez, J.M. Robbins, A.P. Kells, N. Kasahara, J. Forsayeth, D.J. Jolly, K.S. Bankiewicz, Convection-enhanced delivery improves distribution and efficacy of tumor-selective retroviral replicating vectors in a rodent brain tumor model., Cancer Gene Ther. 20 (2013) 336–41. doi:10.1038/cgt.2013.25.

[21] A. a Linninger, M.R. Somayaji, M. Mekarski, L. Zhang, Prediction of convection-enhanced drug delivery to the human brain., J. Theor. Biol. 250 (2008) 125–38. doi:10.1016/j.jtbi.2007.09.009.

[22] E. Lueshen, M. LaRiviere, B. Yamini, A. Linninger, Computer simulations and in vivo convection-enhanced delivery of fluorescent nanoparticles demonstrate variable distribution geometry, Comput. Chem. Eng. (2014). doi:10.1016/j.compchemeng.2014.09.008.

[23] R. Raghavan, M. Brady, Predictive models for pressure-driven fluid infusions into brain parenchyma., Phys. Med. Biol. 56 (2011) 6179–204.

doi:10.1088/0031-9155/56/19/003.

[24] P.A. Hardy, D. Keeley, G. Schorn, E. Forman, Y. Ai, R. Venugopalan, Z. Zhang, L.H. Bradley, Convection enhanced delivery of different molecular weight tracers of gadolinium-tagged polylysine, J. Neurosci. Methods. 219 (2013) 169–175. doi:10.1016/j.jneumeth.2013.07.013.

[25] T. Gill, N.U. Barua, M. Woolley, a S. Bienemann, D.E. Johnson, S O'Sullivan, G. Murray, C. Fennelly, O. Lewis, C. Irving, M.J. Wyatt, P. Moore, S.S. Gill, In vitro and in vivo testing of a novel recessed-step catheter for reflux-free convection-enhanced drug delivery to the brain., J. Neurosci. Methods. 219 (2013) 1–9. doi:10.1016/j.jneumeth.2013.06.008.

[26] W. Gu, H. Yao, A. Vega, D. Flagler, Diffusivity of ions in agarose gels and intervertebral disc: effect of porosity, Ann. Biomed. Eng. 32 (2004) 1710–1717. http://link.springer.com/article/10.1007/s10439-004-7823-4 (accessed June 13, 2013).

[27] J.A. MacKay, D.F. Deen, F.C. Szoka, Distribution in brain of liposomes after convection enhanced delivery; Modulation by particle charge, particle diameter, and presence of steric coating, Brain Res. 1035 (2005) 139–153. doi:10.1016/j.brainres.2004.12.007.

[28] G.W. Astary, S. Kantorovich, P.R. Carney, T.H. Mareci, M. Sarntinoranont, Regional convection-enhanced delivery of gadolinium-labeled albumin in the rat hippocampus in vivo, J. Neurosci. Methods. 187 (2010) 129–137. doi:10.1016/j.jneumeth.2010.01.002.

[29] A. Mangraviti, S.Y. Tzeng, K.L. Kozielski, Y. Wang, Y. Jin, D. Gullotti, M. Pedone, N. Buaron, A. Liu, D.R. Wilson, S.K. Hansen, F.J. Rodriguez, G.-D. Gao, F. DiMeco, H. Brem, A. Olivi, B. Tyler, J.J. Green, Â.S.Y. Tzeng, Â.K.L. Kozielski, Â.Y. Wang, Â.Y. Jin, D. Gullotti, M. Pedone, N. Buaron, A. Liu, D.R. Wilson, S.K. Hansen, F.J. Rodriguez, X.G. Gao, F. DiMeco, O.H. Brem, A. Olivi, B. Tyler, J.J. Green, Polymeric Nanoparticles for Nonviral Gene Therapy Extend Brain Tumor Survival in Vivo., ACS Nano. 9 (2015) 1236–1249. doi:10.1021/nn504905q.

[30] R. Saito, M.T. Krauze, J.R. Bringas, C. Noble, T.R. McKnight, P. Jackson, M.F. Wendland, C. Mamot, D.C. Drummond, D.B. Kirpotin, K. Hong, M.S. Berger, J.W. Park, K.S. Bankiewicz, Gadolinium-loaded liposomes allow for real-time magnetic resonance imaging of convection-enhanced delivery in the primate brain, Exp. Neurol. 196 (2005) 381–389. doi:10.1016/j.expneurol.2005.08.016.

[31] P.J. Haar, W.C. Broaddus, Z.-J. Chen, P.P. Fatouros, G.T. Gillies, F.D. Corwin, Quantification of convection-enhanced delivery to the ischemic brain., Physiol. Meas. 31 (2010) 1075–1089. doi:10.1088/0967-3334/31/9/001.

[32] R.O. Weller, M. Subash, S.D. Preston, I. Mazanti, R.O. Carare, Perivascular drainage of amyloid-beta peptides from the brain and its failure in cerebral amyloid angiopathy and Alzheimer's disease., Brain Pathol. 18 (2008) 253–66. doi:10.1111/j.1750-3639.2008.00133.x.

[33] C.P. Foley, N. Nishimura, K.B. Neeves, C.B. Schaffer, W.L. Olbricht, Real-time imaging of perivascular transport of nanoparticles during convection-enhanced delivery in the rat cortex., Ann. Biomed. Eng. 40 (2012) 292–303. doi:10.1007/s10439-011-0440-0.

[34] M.T. Krauze, R. Saito, C. Noble, J. Bringas, J. Forsayeth, T.R. McKnight, J. Park, K.S. Bankiewicz, Effects of the perivascular space on convection-enhanced delivery of liposomes in primate putamen, Exp. Neurol. 196 (2005) 104–111. doi:10.1016/j.expneurol.2005.07.009.

[35] N.G. Horton, K. Wang, C.C. Wang, C. Xu, In vivo three-photon imaging of subcortical structures of an intact mouse brain using quantum dots, Nat. Photonics. 7 (2013) 205–209. doi:10.1109/CLEOE-IQEC.2013.6801501.

[36] M. Oheim, D.J. Michael, M. Geisbauer, D. Madsen, R.H. Chow, Principles of two-photon excitation fluorescence microscopy and other nonlinear imaging approaches., Adv. Drug Deliv. Rev. 58 (2006) 788–808. doi:10.1016/j.addr.2006.07.005.

[37] J.H. Kim, G.W. Astary, T.L. Nobrega, S. Kantorovich, P.R. Carney, T.H. Mareci, M. Sarntinoranont, Dynamic contrast-enhanced MRI of Gd-albumin

delivery to the rat hippocampus in vivo by convection-enhanced delivery, J. Neurosci. Methods. 209 (2012) 62–73. doi:10.1016/j.jneumeth.2012.05.024.

[38] R.M. Richardson, A.P. Kells, K.H. Rosenbluth, E.A. Salegio, M.S. Fiandaca, P.S. Larson, P. a Starr, A.J. Martin, R.R. Lonser, H.J. Federoff, J.R. Forsayeth, K.S. Bankiewicz, Interventional MRI-guided putaminal delivery of AAV2-GDNF for a planned clinical trial in Parkinson's disease., Mol. Ther. 19 (2011) 1048–1057. doi:10.1038/mt.2011.11.

[39] R.G. Thorne, C. Nicholson, In vivo diffusion analysis with quantum dots and dextrans predicts the width of brain extracellular space., Proc. Natl. Acad. Sci. U. S. A. 103 (2006) 5567–5572. doi:10.1073/pnas.0509425103.

[40] E. Nance, C. Zhang, T.Y. Shih, Q. Xu, B.S. Schuster, J. Hanes, Brain-penetrating nanoparticles improve paclitaxel efficacy in malignant glioma following local administration, ACS Nano. 8 (2014) 10655–10664. doi:10.1021/nn504210g.

[41] E.A. Nance, G.F. Woodworth, K.A. Sailor, T.-Y. Shih, Q. Xu, G. Swaminathan, D. Xiang, C. Eberhart, J. Hanes, A Dense Poly(Ethylene Glycol) Coating Improves Penetration of Large Polymeric Nanoparticles Within Brain Tissue, Sci. Transl. Med. 4 (2012) 149ra119-149ra119. doi:10.1126/scitranslmed.3003594.

[42] D.S. Hersh, B.A. Nguyen, J.G. Dancy, A.R. Adapa, J.A. Winkles, G.F. Woodworth, A.J. Kim, V. Frenkel, Pulsed ultrasound expands the extracellular and perivascular spaces of the brain, Brain Res. 1646 (2016) 543–550. doi:10.1016/j.brainres.2016.06.040.

[43] J.J. Iliff, M. Wang, Y. Liao, B. a. Plogg, W. Peng, G. a. Gundersen, H. Benveniste, G.E. Vates, R. Deane, S. a. Goldman, E. a. Nagelhus, M. Nedergaard, A Paravascular Pathway Facilitates CSF Flow Through the Brain Parenchyma and the Clearance of Interstitial Solutes, Including Amyloid, Sci. Transl. Med. 4 (2012) 147ra111-147ra111. doi:10.1126/scitranslmed.3003748.

[44] A.P. Pathak, D. Artemov, B.D. Ward, D.G. Jackson, M. Neeman, Z.M. Bhujwalla, Characterizing extravascular fluid transport of macromolecules in

the tumor interstitium by magnetic resonance imaging., Cancer Res. 65 (2005) 1425–32. doi:10.1158/0008-5472.CAN-04-3682.

[45] H.F. Cserr, L.H. Ostrach, Bulk flow of interstitial fluid after intracranial injection of Blue Dextran 2000, Exp. Neurol. 45 (1974) 50–60. doi:10.1016/0014-4886(74)90099-5.

[46] M.L. Rennels, T.F. Gregory, O.R. Blaumanis, K. Fujimoto, P.A. Grady, Evidence for a "Paravascular" fluid circulation in the mammalian central nervous system, provided by the rapid distribution of tracer protein throughout the brain from the subarachnoid space, Brain Res. 326 (1985) 47–63. doi:10.1016/0006-8993(85)91383-6.

[47] P. Wang, W.L. Olbricht, Fluid mechanics in the perivascular space., J. Theor. Biol. 274 (2011) 52–7. doi:10.1016/j.jtbi.2011.01.014.

[48] P. Hadaczek, Y. Yamashita, H. Mirek, L. Tamas, M.C. Bohn, C. Noble, J.W. Park, K. Bankiewicz, The "Perivascular Pump" Driven by Arterial Pulsation Is a Powerful Mechanism for the Distribution of Therapeutic Molecules within the Brain, Mol. Ther. 14 (2006) 69–78. doi:10.1016/j.ymthe.2006.02.018.

[49] V. Kiviniemi, X. Wang, V. Korhonen, T. Keinänen, T. Tuovinen, J. Autio, P. LeVan, S. Keilholz, Y.-F. Zang, J. Hennig, M. Nedergaard, Ultra-fast magnetic resonance encephalography of physiological brain activity - Glymphatic pulsation mechanisms?, J. Cereb. Blood Flow Metab. (2015) 0271678X15622047. doi:10.1177/0271678X15622047.

[50] L. Xie, H. Kang, Q. Xu, M.J. Chen, Y. Liao, M. Thiyagarajan, J. O'Donnell, D.J. Christensen, C. Nicholson, J.J. Iliff, T. Takano, R. Deane, M. Nedergaard, Sleep drives metabolite clearance from the adult brain., Science. 342 (2013) 373–7. doi:10.1126/science.1241224.

[51] J.J. Iliff, M.J. Chen, B.A. Plog, D.M. Zeppenfeld, M. Soltero, L. Yang, I. Singh, R. Deane, M. Nedergaard, Impairment of Glymphatic Pathway Function Promotes Tau Pathology after Traumatic Brain Injury, J. Neurosci. (2014). doi:10.1523/JNEUROSCI.3020-14.2014.

[52] B.T. Kress, J.J. Iliff, M. Xia, M. Wang, H. Wei, D. Zeppenfeld, L. Xie, H.

Kang, Q. Xu, J. Liew, B.A. Plog, F. Ding, R. Deane, M. Nedergaard, Impairment of paravascular clearance pathways in the aging brain., Ann. Neurol. (2014). doi:10.1002/ana.24271.

[53] A.F.H. McCaslin, B.R. Chen, A.J. Radosevich, B. Cauli, E.M.C. Hillman, In vivo 3D morphology of astrocyte-vasculature interactions in the somatosensory cortex: implications for neurovascular coupling., J. Cereb. Blood Flow Metab. 31 (2011) 795–806. doi:10.1038/jcbfm.2010.204.

[54] M. Desjardins, R. Berti, J. Lefebvre, S. Dubeau, F. Lesage, Aging-related differences in cerebral capillary blood flow in anesthetized rats., Neurobiol. Aging. 35 (2014) 1947–55. doi:10.1016/j.neurobiolaging.2014.01.136.

[55] K.B. Neeves, A.J. Sawyer, C.P. Foley, W.M. Saltzman, W.L. Olbricht, Dilation and degradation of the brain extracellular matrix enhances penetration of infused polymer nanoparticles., Brain Res. 1180 (2007) 121–32. doi:10.1016/j.brainres.2007.08.050.

[56] C. Nicholson, Diffusion and related transport mechanisms in brain tissue, Reports Prog. Phys. 64 (2001) 815–884. doi:10.1088/0034-4885/64/7/202.

[57] D. Yin, J. Forsayeth, K.S. Bankiewicz, Optimized cannula design and placement for convection-enhanced delivery in rat striatum., J. Neurosci. Methods. 187 (2010) 46–51. doi:10.1016/j.jneumeth.2009.12.008.

[58] F. Wang, Y. Shi, L. Lu, L. Liu, Y. Cai, H. Zheng, X. Liu, F. Yan, C. Zou, C. Sun, J. Shi, S. Lu, Y. Chen, Targeted Delivery of GDNF through the Blood-Brain Barrier by MRI-Guided Focused Ultrasound, PLoS One. 7 (2012) 1–8. doi:10.1371/journal.pone.0052925.

[59] M.T. Krauze, J. Forsayeth, J.W. Park, K.S. Bankiewicz, Real-time imaging and quantification of brain delivery of liposomes., Pharm. Res. 23 (2006) 2493–504. doi:10.1007/s11095-006-9103-5.

[60] M.T. Krauze, J. Forsayeth, D. Yin, K.S. Bankiewicz, Convection-enhanced delivery of liposomes to primate brain., Methods Enzymol. 465 (2009) 349–362. doi:10.1016/S0076-6879(09)65018-7.

[61] J.H. Sampson, G. Archer, C. Pedain, E. Wembacher-Schröder, M. Westphal, S.

Kunwar, M. a Vogelbaum, A. Coan, J.E. Herndon, R. Raghavan, M.L. Brady, D. a Reardon, A.H. Friedman, H.S. Friedman, M.I. Rodríguez-Ponce, S.M. Chang, S. Mittermeyer, D. Croteau, R.K. Puri, Poor drug distribution as a possible explanation for the results of the PRECISE trial., J. Neurosurg. 113 (2010) 301–9. doi:10.3171/2009.11.JNS091052.

[62] E. Nance, K. Timbie, G.W. Miller, J. Song, C. Louttit, A.L. Klibanov, T.Y. Shih, G. Swaminathan, R.J. Tamargo, G.F. Woodworth, J. Hanes, R.J. Price, Non-invasive delivery of stealth, brain-penetrating nanoparticles across the blood - Brain barrier using MRI-guided focused ultrasound, J. Control. Release. 189 (2014) 123–132. doi:10.1016/j.jconrel.2014.06.031.

[63] T.M. Allen, P.R. Cullis, Drug delivery systems: entering the mainstream., Science. 303 (2004) 1818–22. doi:10.1126/science.1095833.

[64] Y. Çirpanli, E. Allard, C. Passirani, E. Bilensoy, L. Lemaire, S. Çaliş, J.P. Benoit, Antitumoral activity of camptothecin-loaded nanoparticles in 9L rat glioma model, Int. J. Pharm. 403 (2011) 201–206. doi:10.1016/j.ijpharm.2010.10.015.

[65] J. Zhou, T.R. Patel, R.W. Sirianni, G. Strohbehn, M.-Q. Zheng, N. Duong, T. Schafbauer, A.J. Huttner, Y. Huang, R.E. Carson, Y. Zhang, D.J. Sullivan, J.M. Piepmeier, W.M. Saltzman, Highly penetrative, drug-loaded nanocarriers improve treatment of glioblastoma., Proc. Natl. Acad. Sci. U. S. A. 110 (2013) 11751–6. doi:10.1073/pnas.1304504110.

[66] T. Nakamura, R. Saito, S.I. Sugiyama, Y. Sonoda, T. Kumabe, T. Tominaga, Local convection-enhanced delivery of chemotherapeutic agent transiently opens blood-brain barrier and improves efficacy of systemic chemotherapy in intracranial xenograft tumor model, Cancer Lett. 310 (2011) 77–83. doi:10.1016/j.canlet.2011.06.018.

[67] T. Huo, R.F. Barth, W. Yang, R.J. Nakkula, R. Koynova, B. Tenchov, A.R. Chaudhury, L. Agius, T. Boulikas, H. Elleaume, R.J. Lee, Preparation, Biodistribution and Neurotoxicity of Liposomal Cisplatin following Convection Enhanced Delivery in Normal and F98 Glioma Bearing Rats, PLoS One. 7

(2012). doi:10.1371/journal.pone.0048752.

[68] G.D. Kenny, A.S. Bienemann, A.D. Tagalakis, J.A. Pugh, K. Welser, F. Campbell, A.B. Tabor, H.C. Hailes, S.S. Gill, M.F. Lythgoe, C.W. McLeod, E.A. White, S.L. Hart, Multifunctional receptor-targeted nanocomplexes for the delivery of therapeutic nucleic acids to the Brain, Biomaterials. 34 (2013) 9190–9200. doi:10.1016/j.biomaterials.2013.07.081.

[69] E.A. Salegio, H. Streeter, N. Dube, P. Hadaczek, L. Samaranch, A.P. Kells, W. San Sebastian, Y. Zhai, J. Bringas, T. Xu, J. Forsayeth, K.S. Bankiewicz, Distribution of nanoparticles throughout the cerebral cortex of rodents and non-human primates: Implications for gene and drug therapy., Front. Neuroanat. 8 (2014) 9. doi:10.3389/fnana.2014.00009.

[70] Z.R. Stephen, F.M. Kievit, O. Veiseh, P.A. Chiarelli, C. Fang, K. Wang, S.J. Hatzinger, R.G. Ellenbogen, J.R. Silber, M. Zhang, S.E.T. Al, Redox-Responsive Magnetic Nanoparticle for Targeted Convection-Enhanced Delivery of O 6 - Benzylguanine to Brain Tumors, ACS Nano. (2014) 10383–10395.

[71] A. Arshad, B. Yang, A.S. Bienemann, N.U. Barua, M.J. Wyatt, M. Woolley, D.E. Johnson, K.J. Edler, S.S. Gill, Convection-Enhanced Delivery of Carboplatin PLGA Nanoparticles for the Treatment of Glioblastoma, PLoS One. 10 (2015) e0132266. doi:10.1371/journal.pone.0132266.

[72] G.M. Bernal, M.J. LaRiviere, N. Mansour, P. Pytel, K.E. Cahill, D.J. Voce, S. Kang, R. Spretz, U. Welp, S.E. Noriega, L. Nuñez, G. Larsen, R.R. Weichselbaum, B. Yamini, Convection-enhanced delivery and in vivo imaging of polymeric nanoparticles for the treatment of malignant glioma., Nanomedicine. (2014). doi:10.1016/j.nano.2013.07.003.

[73] J.R. Weiser, W.M. Saltzman, Controlled release for local delivery of drugs: barriers and models., J. Control. Release. 190 (2014) 664–73. doi:10.1016/j.jconrel.2014.04.048.

[74] L. Tao, C. Nicholson, Diffusion of albumins in rat cortical slices and relevance to volume transmission, Neuroscience. 75 (1996) 839–847. doi:10.1016/0306-

4522(96)00303-X.

[75] M. Sarntinoranont, R.K. Banerjee, R.R. Lonser, P.F. Morrison, A computational model of direct interstitial infusion of macromolecules into the spinal cord, Ann. Biomed. Eng. 31 (2003) 448–461. doi:10.1114/1.1558032.

[76] A. a Linninger, M.R. Somayaji, T. Erickson, X. Guo, R.D. Penn, Computational methods for predicting drug transport in anisotropic and heterogeneous brain tissue., J. Biomech. 41 (2008) 2176–87. doi:10.1016/j.jbiomech.2008.04.025.

[77] J.P.M. Motion, G.H. Huynh, F.C. Szoka, R. a. Siegel, Convection and retro-convection enhanced delivery: some theoretical considerations related to drug targeting., Pharm. Res. 28 (2011) 472–479. doi:10.1007/s11095-010-0296-2.

[78] Z.-J. Chen, W.C. Broaddus, R.R. Viswanathan, R. Raghavan, G.T. Gillies, Intraparenchymal drug delivery via positive-pressure infusion: experimental and modeling studies of poroelasticity in brain phantom gels., IEEE Trans. Biomed. Eng. 49 (2002) 85–96. doi:10.1109/10.979348.

[79] S. Kunwar, S. Chang, M. Westphal, M. Vogelbaum, J. Sampson, G. Barnett, M. Shaffrey, Z. Ram, J. Piepmeier, M. Prados, D. Croteau, C. Pedain, P. Leland, S.R. Husain, B.H. Joshi, R.K. Puri, Phase III randomized trial of CED of IL13-PE38QQR vs Gliadel wafers for recurrent glioblastoma, Neuro. Oncol. 12 (2010) 871–881. doi:10.1093/neuonc/nop054.

[80] J.M. Bezemer, D.W. Grijpma, P.J. Dijkstra, C.A. Van Blitterswijk, J. Feijen, A controlled release system for proteins based on poly (ether ester) block-copolymers : polymer network characterization, J. Control. Release. 62 (1999) 393–405.

[81] Z.-J. Chen, G.T. Gillies, W.C. Broaddus, S.S. Prabhu, H. Fillmore, R.M. Mitchell, F.D. Corwin, P.P. Fatouros, H.F. Young, N. Section, H.H. Mcguire, V. Affairs, A realistic brain tissue phantom for intraparenchymal infusion studies., J. Neurosurg. 101 (2004) 314–322. doi:10.3171/jns.2004.101.2.0314.

[82] L.C. Vazquez, E. Hagel, B.J. Willenberg, W. Dai, F. Casanova, C.D. Batich, M. Sarntinoranont, Polymer-coated cannulas for the reduction of backflow during

intraparenchymal infusions, J. Mater. Sci. Mater. Med. 23 (2012) 2037–2046. doi:10.1007/s10856-012-4652-0.

[83] F. Casanova, P.R. Carney, M. Sarntinoranont, Influence of needle insertion speed on backflow for convection-enhanced delivery., J. Biomech. Eng. 134 (2012) 41006. doi:10.1115/1.4006404.

[84] M.M. Chui, R.J. Phillips, M.J. McCarthy, Measurement of the Porous Microstructure of Hydrogels by Nuclear Magnetic Resonance, J. Colloid Interface Sci. 174 (1995) 336–344. doi:10.1006/jcis.1995.1399.

[85] A.K. Diem, M. Tan, N.W. Bressloff, C. Hawkes, A.W.J. Morris, R.O. Weller, R.O. Carare, A Simulation Model of Periarterial Clearance of Amyloid-β from the Brain, Front. Aging Neurosci. 8 (2016) 1–11. doi:10.3389/fnagi.2016.00018.

[86] G.J. Baker, V.N. Yadav, S. Motsch, C. Koschmann, A.-A. Calinescu, Y. Mineharu, S.I. Camelo-Piragua, D. Orringer, S. Bannykh, W.S. Nichols, A.C. deCarvalho, T. Mikkelsen, M.G. Castro, P.R. Lowenstein, Mechanisms of Glioma Formation: Iterative Perivascular Glioma Growth and Invasion Leads to Tumor Progression, VEGF-Independent Vascularization, and Resistance to Antiangiogenic Therapy, Neoplasia. 16 (2014) 543–561. doi:10.1016/j.neo.2014.06.003.